The Astrophysical Journal, 790:10 (30pp), 2014 July 20 doi:10.1088/0004-637X/790/1/10

H I-TO-H_2 TRANSITIONS AND H I COLUMN DENSITIES IN GALAXY STAR-FORMING REGIONS

Amiel Sternberg[1], Franck Le Petit[2], Evelyne Roueff[2], and Jacques Le Bourlot[2,3]
[1] Raymond and Beverly Sackler School of Physics & Astronomy, Tel Aviv University, Ramat Aviv 69978, Israel
[2] LERMA, Observatoire de Paris, CNRS, 5 place Jules Janssen, F-92190 Meudon, France
[3] Université Paris Diderot, 5 rue Thomas-Mann, F-75205 Paris cedex 13, France
Received 2013 November 13; accepted 2014 April 16; published 2014 June 27

ABSTRACT

We present new analytic theory and radiative transfer computations for the atomic-to-molecular (H I-to-H_2) transitions and the buildup of atomic hydrogen (H I) gas columns in optically thick interstellar clouds irradiated by far-UV (FUV) photodissociating radiation fields. We derive analytic expressions for the total H I column densities for (one-dimensional (1D)) planar slabs, for beamed or isotropic radiation fields, from the weak- to strong-field limits, for gradual or sharp atomic-to-molecular transitions, and for arbitrary metallicity. Our expressions may be used to evaluate the H I column densities as functions of the radiation field intensity and the H_2-dust-limited dissociation flux, the hydrogen gas density, and the metallicity-dependent H_2 formation rate coefficient and FUV dust grain absorption cross section. We make the distinction between "H I-dust" and "H_2-dust" opacity, and we present computations for the "universal H_2-dust-limited effective dissociation bandwidth." We validate our analytic formulae with *Meudon PDR code* computations for the H I-to-H_2 density profiles and total H I column densities. We show that our general 1D formulae predict H I columns and H_2 mass fractions that are essentially identical to those found in more complicated (and approximate) spherical (shell–core) models. We apply our theory to compute H_2 mass fractions and star-formation thresholds for individual clouds in self-regulated galaxy disks, for a wide range of metallicities. Our formulae for the H I columns and H_2 mass fractions may be incorporated into hydrodynamics simulations for galaxy evolution.

Key words: galaxies: ISM – ISM: clouds – ISM: general – ISM: structure – stars: formation

Online-only material: color figures

1. INTRODUCTION

The atomic-to-molecular hydrogen (H I-to-H_2) transition is of central importance for the evolution of the interstellar medium (ISM) and for star formation in galaxies, from local environments in the Milky Way to distant cold gas reservoirs in high-redshift systems. Stars form in molecular gas, plausibly because H_2 formation enhances low-temperature cooling and cloud fragmentation or perhaps simply because the molecular formation rates are elevated in the denser and more shielded components of the gravitationally collapsing regions. The atomic-to-molecular conversion is also the critical initiating step for the growth of chemical complexity in the ISM from large to small scales, e.g., from diffuse clouds to dense star-forming cores to protoplanetary disks. Globally, the transition to H_2 appears to be associated with star-formation thresholds in galaxy-wide Kennicutt–Schmidt relations and with the observed critical gas mass surface densities above which star formation becomes probable.

In this paper, we revisit the theory of the H I-to-H_2 transition and the buildup of atomic hydrogen gas layers in fully optically thick interstellar clouds irradiated by far-UV (FUV) radiation fields. Atomic (H I) gas produced by rapid stellar FUV "Lyman–Werner" (LW) photodissociation undergoes conversion to H_2 as the destructive radiation is absorbed. In steady state, a mass of H I is maintained in the outer FUV-irradiated photon-dominated regions (PDRs) of the dense molecular clouds. Much of the (cold) H I gas in galaxies may reside in such cloud boundary layers and envelopes, interspersed with the recently formed FUV-emitting OB-type stars.

The study of interstellar H I-to-H_2 conversion has had a long and venerable history. Early theoretical discussions (e.g., Spitzer 1948; Gould & Salpeter 1963; Field et al. 1966; Stecher & Williams 1967; de Jong 1972; followed by Aaronson et al. 1974; Glassgold & Langer 1974; Jura 1974; Black & Dalgarno 1977; Federman et al. 1979; van Dishoeck & Black 1986) focused on the competing processes of (grain surface) molecule formation, photodissociation, and shielding in predominantly atomic gas—the classical warm and cold neutral medium (WNM and CNM) and diffuse gas—showing that significant concentrations of H_2 could be expected in the Galactic ISM, especially in dark, dusty clouds with high visual extinctions (Mészáros 1968; Hollenbach et al. 1971; Solomon & Werner 1971; de Jong 1972). This was confirmed observationally with the first direct (FUV LW absorption line) detections of interstellar molecular hydrogen in diffuse clouds and the correlation of the H_2 with $E(B-V)$ color excess and dust extinction (Carruthers 1970; Spitzer et al. 1973; Savage et al. 1977) and with the discovery of fully molecular clouds via proxy millimeter-wave carbon monoxide (CO) emissions (Wilson et al. 1970; Rank et al. 1971).

Absorption line spectroscopy (Lyα for H I; LW band for H_2) has been carried out for H I-to-H_2 conversion along many Milky Way sight lines, through low-extinction diffuse-to-translucent gas in the disk, and into the infrared cirrus and high-velocity gas in vertical directions (Savage et al. 1977; Bohlin et al. 1978; Richter et al. 2001; Liszt & Lucas 2002; Rachford et al. 2002, 2009; Gillmon & Shull 2006; Gillmon et al. 2006; Wakker 2006; Liszt 2007; France et al. 2013; Fukui et al. 2014; Röhser et al. 2014). These studies probe systems in which the H_2 mass fractions range over many orders of magnitude, from $\lesssim 10^{-5}$ up to $\sim$50% in highly reddened systems. Absorption line observations of damped and sub-damped Lyα absorbers at high redshifts also directly reveal the partial conversion of H I to H_2 in optically thin media (Levshakov & Varshalovich 1985; Foltz et al. 1988; Ge & Bechtold 1997; Cui et al. 2005; Ledoux et al.

2006; Noterdaeme et al. 2010; Crighton et al. 2013; Albornoz Vásquez et al. 2014). In the early universe, the formation of the first stars (Population III) was enabled by the partial conversion to H_2 via negative ion chemistry. The resulting H_2 rotational line gas cooling rates were likely regulated by LW photodissociation "feedback" from the first stars and FUV sources (Palla et al. 1983; Lepp & Shull 1984; Haiman et al. 1996, 1997; Abel et al. 1997; Ciardi et al. 2000; Glover & Brand 2003; Yoshida et al. 2003; Wise & Abel 2007; Dijkstra et al. 2008; Ahn et al. 2009; Bromm et al. 2009; Miyake et al. 2010; Wolcott-Green et al. 2011; Fialkov et al. 2012; Holzbauer & Furlanetto 2012; Safranek-Shrader et al. 2012; Visbal et al. 2014).

In optically thick regions, 21 cm observations of very cold ($\lesssim$20 K) narrow-line self-absorbed H I (the Galactic "HINSA"; Li & Goldsmith 2003) in combination with CO, OH, and dust mapping for locating the H_2 clouds reveal the presence of trace atomic hydrogen inside dark, dusty, and predominantly molecular clouds (Bok et al. 1955; Heiles 1969; Knapp 1974; Burton et al. 1978; McCutcheon et al. 1978; Liszt & Burton 1979; Mebold et al. 1982; van der Werf et al. 1988; Li & Goldsmith 2003; Goldsmith & Li 2005; Krčo & Goldsmith 2010). Such clouds are fully shielded against externally incident photodissociating FUV radiation, and the conversion to H_2 is essentially complete. The residual atomic gas in the cloud cores is likely the product of impact ionization by penetrating low-energy cosmic rays (Spitzer & Tomasko 1968; Webber 1998; Dalgarno 2006). Somewhat warmer H I ($\sim$100 K, so still "cold") is also observed in dissociation zones surrounding Galactic H II regions associated with individual OB-type stars or clusters and/or as H I PDRs in molecular cloud envelopes exposed to ambient interstellar radiation (e.g., Sancisi et al. 1974; Myers et al. 1978; Read 1981; Roger & Pedlar 1981; Wannier et al. 1983; Elmegreen & Elmegreen 1987; van der Werf & Goss 1989; Wannier et al. 1991; Andersson et al. 1992; Gir et al. 1994; Reach et al. 1994; Williams & Maddalena 1996; Gomez et al. 1998; Habart et al. 2003; Matthews et al. 2003; Roger et al. 2004; Lee et al. 2007; Lee et al. 2012; van der Werf et al. 2013). In nearby galaxies, H I has been mapped in spiral arms showing that the atomic gas likely traces outer photodissociated layers in the star-forming giant molecular clouds (Allen et al. 1986, 1997; Shaya & Federman 1987; Rand et al. 1992; Madden et al. 1993; Smith et al. 2000; Heyer et al. 2004; Heiner et al. 2009, 2011; Knapen et al. 2006; Schuster et al. 2007).

By the 1980s, a conceptual switch had occurred with the recognition that much of the hydrogen in galaxies is fully shielded H_2 and that in dense gas in star-forming regions the H I is often a surface photodissociation "product," rather than being the dominant component within which some shielded H_2 may be present, as in the diffuse medium. Over the decades, many model computations for the H I-to-H_2 transition in optically thick media have been presented, with varying degrees of sophistication in treating the critical roles of FUV dust absorption and scattering and H_2 absorption line self-shielding. These include one-dimensional (1D) plane-parallel (slab) models assuming steady state conditions with simplified ("isolated line") treatments of H_2 self-shielding (Federman et al. 1979; de Jong et al. 1980; Tielens & Hollenbach 1985; Viala 1986; Black & van Dishoeck 1987; Sternberg 1988; Sternberg & Dalgarno 1989; Burton et al. 1990; Spaans et al. 1994; Sternberg & Neufeld 1999; Kaufman et al. 1999), models incorporating "exact" radiative transfer for the combined effects of multiple H_2 absorption line overlap and dust absorption and scattering (van Dishoeck & Black 1988, 1990; Viala et al. 1988; Abgrall et al. 1992; Draine & Bertoldi 1996; Browning et al. 2003; Shaw et al. 2005; Goicoechea & Le Bourlot 2007; Le Petit et al. 2006), spherically symmetric models (Andersson & Wannier 1993; Diaz-Miller et al. 1998; Neufeld & Spaans 1996; Stoerzer et al. 1996; Spaans & Neufeld 1997; Spaans & van Dishoeck 1997; Krumholz et al. 2008, 2009; McKee & Krumholz 2010; Wolfire et al. 2010), and also time-dependent models for the H_2 formation and destruction (London 1978; Roger & Dewdney 1992; Goldshmidt & Sternberg 1995; Hollenbach & Natta 1995; Lee et al. 1996; Goldsmith et al. 2007). More recently, sophisticated multidimensional (2D and 3D) radiative transfer codes have been developed for the atomic-to-molecular conversion, also incorporating hydrodynamics (Robertson & Kravtsov 2008; Gnedin et al. 2009; Glover et al. 2010; Bisbas et al. 2012; Christensen et al. 2012; Mac Low & Glover 2012; Davé et al. 2013; Offner et al. 2013; Thompson et al. 2014), although the H_2 photodissociation rates and the implied H I/H_2 density ratios are generally still estimated using 1D shielding prescriptions for the individual hydrodynamic particles or cells.

In recent years interstellar H I-to-H_2 conversion has become an important issue in the study of galaxy evolution on large scales, across entire galaxy disks, at both low and high redshifts, and for varying metallicities (e.g., Wong & Blitz 2002; Böker et al. 2003; Blitz & Rosolowsky 2004, 2006; Bigiel et al. 2008; Leroy et al. 2008; Tacconi et al. 2010; Bolatto et al. 2011; Schruba et al. 2011; Welty et al. 2012; Genzel et al. 2012, 2013; Tacconi et al. 2013). Galaxy mapping surveys suggest that on global scales the star-formation efficiencies are determined, at least in part, by molecular gas fractions that may be sensitive to the varying midplane gas pressures and/or metallicities (e.g., Hirashita & Ferrara 2005; Fumagalli et al. 2010; Fu et al. 2010; Lagos et al. 2011; Feldmann et al. 2012; Kuhlen et al. 2013; Popping et al. 2014). Remarkably, the observations of disk galaxies on large scales (e.g., Leroy et al. 2008), and individual Galactic molecular clouds on small scales (e.g., Lee et al. 2012, 2014), indicate that for solar metallicity the H I-to-H_2 conversion occurs for characteristic gas surface densities of $\sim 10\, M_\odot\ \mathrm{pc}^{-2}$ (for "ambient" FUV radiation fields). This surface density corresponds to an FUV dust optical depth $\sim$1 for typical grain properties and dust-to-gas mass ratios, suggesting that dust absorption and hence metallicity is playing an essential role in setting the critical gas surface densities.

An analytic theory for the H I-to-H_2 transition was presented by Sternberg (1988, hereafter S88),who derived a scaling law for the growth of the H I column density and the associated FUV-excited infrared H_2 vibrational emission intensities produced in optically thick irradiated cloud surfaces, for application to Galactic emission line sources (see also Jura 1974; Hill & Hollenbach 1978; Elmegreen 1993). S88 included a general-purpose analytic formula for the total H I column density as a function of the FUV radiation intensity, the cloud gas density, and the metallicity-dependent H_2 formation rate coefficient and FUV dust attenuation cross section. S88 also identified the fundamental dimensionless parameter that controls the H I-to-H_2 transitions and the buildup of the atomic hydrogen columns.

More recently, and motivated by the possible metallicity dependence of molecular mass fractions in galaxy disks, Krumholz et al. (2008, 2009) and McKee & Krumholz (2010; hereafter KMT/MK10) presented new models for the H I-to-H_2 transition and for the associated metallicity-dependent H_2 mass fractions and star-formation surface density thresholds. A novel feature of the KMT/MK10 study is their analytic focus on (idealized) spherical clouds embedded in ambient isotropic fields, as

opposed to the (also idealized) planar geometry and beamed fields adopted in much of the earlier PDR literature, including S88.

Our main goal and motivation in this paper is to reintroduce and extend the S88 theory for applications to global galaxy evolution studies. In Section 2 we elaborate on S88 and present a detailed overview and discussion of the basic theoretical ingredients and parameters controlling the H I-to-H_2 transition in FUV-irradiated clouds. We rederive the fundamental S88 equation for the total H I column density produced for beamed radiation into a (1D) optically thick slab. We then extend the theory and consider irradiation by isotropic fields. This will enable our direct comparison with the more complicated (and more approximate) formalism for spheres. In Section 3 we present detailed numerical (*Meudon PDR code*) radiative transfer computations for the H I-to-H_2 transitions and integrated H I columns for a wide range of interstellar conditions. The ratio of the free-space FUV field intensity (or dissociation rate) to the gas density (or H_2 formation rate) is an essential parameter, as is the metallicity and dust-to-gas mass ratio. We present numerical computations for a verification of our analytic formulae for beamed and isotropic irradiation from the weak- to strong-field limits (gradual to sharp H I-to-H_2 transitions) and for low- to high-metallicity gas. In Section 4 we compare our planar formulae with the KMT/MK10 theory for spheres. This includes a discussion of the dimensionless parameters and a comparison of the expressions for the total H I columns, H_2 mass fractions, and star-formation thresholds, as functions of the metallicity. An important application and comparison is for "self-regulated gas" in which the FUV intensity–to–gas density ratio is set by the condition of two-phased equilibrium for H I. We demonstrate that our simpler, more general, and fully analytic 1D formulae predict H I columns and H_2 mass fractions that are essentially identical to results for spheres in the more restricted regime in which the spherical models are applicable (intense fields, sharp transitions, low metallicity).

This is a lengthy paper, and we develop the theory and present our step-by-step comparisons in a pedagogical style. In Section 5 we summarize and recap our basic analytic results for the H I column densities and molecular mass fractions in FUV-irradiated clouds, including for self-regulated star-forming galaxies. A glossary of symbols is in the Appendix.

2. ANALYTIC OVERVIEW

In this section we present an analytic discussion and overview of the basic processes and quantities that control the H I-to-H_2 transitions and total H I columns in interstellar clouds exposed to photodissociating FUV radiation fields. Our overview anticipates and also provides analytic representations for the detailed numerical results that we present in Section 3. We focus on idealized static 1D semi-infinite uniform density isothermal and optically thick plane-parallel clouds that are irradiated by steady fluxes of FUV LW-band photons. We rederive the S88 formula for the steady state H I column densities produced in slabs irradiated by normally incident unidirectional beamed fields as appropriate for interstellar clouds exposed to localized FUV sources. We then show that this formula can be generalized to clouds embedded in isotropic radiation fields. Isotropic irradiation may be more representative of global ambient conditions in galaxies.

We begin with our normalizations for the beamed and isotropic ultraviolet radiation fields and for the associated H_2 photodissociation rates (Section 2.1). We then define the dissociation bandwidth and its derivative—the H_2 self-shielding function (Section 2.2.1). We then describe our treatment of dust grains (Section 2.2.2). The grains provide FUV continuum opacity and are also the H_2 formation sites. The metallicity of the gas then enters as an important parameter because it controls the dust-to-gas mass ratio and therefore also the associated H_2 formation efficiency and the FUV dust optical depth per gas column density. We make the simplifying assumption that the dust-to-gas mass ratio scales linearly with the metallicity. If star formation requires the conversion from H I to H_2, the metallicity will be an essential parameter in controlling the star-formation thresholds.

We put the physical ingredients together and write down the depth-dependent steady state H I/H_2 formation–destruction equation for semi-infinite slabs exposed to beamed fields (Section 2.2.3). Crucially, the differential equation is separable, and this enables our definition of the "universal H_2-dust-limited LW dissociation bandwidth" (Section 2.2.4) and the "effective dissociation flux" (Section 2.2.5). The H_2-dust-limited dissociation bandwidth is a fundamental quantity in the theory, and we present analytic expressions and numerical computations for it in this paper.

We then integrate the H I/H_2 formation–destruction equation to derive our analytic formula for the H I column density for clouds irradiated by beamed fields (Section 2.2.6). Our formula gives the H I column density as a function of the physical variables, including gas density, FUV intensity, effective dissociation flux, H_2 formation rate coefficient, FUV dust absorption cross section, and metallicity.

As we discuss in Section 2.2.6, the H I-to-H_2 transition profiles and the total atomic column densities are controlled by a single dimensionless parameter, "αG," first introduced by S88. In a nutshell, αG determines the LW-band optical depth in the cloud due to the *dust associated with the H I gas* (which we refer to in this paper as "H I-dust"), whether or not the H I is mixed with the H_2. The total H I-dust optical depth is a critical quantity in the theory; for beamed fields our formula for it (as derived in Section 2.2.6) is

$$\tau_{1,\mathrm{tot}} = \ln\left[\frac{\alpha G}{2} + 1\right]. \quad (1)$$

As we show in Section 2.2.7, αG can be expressed in terms of the physical variables in several ways. Most simply, α (also dimensionless) is the ratio of the free-space photodissociation rate to the H_2 formation rate, and G is a cloud-averaged H_2 self-shielding factor. The product αG is then similar to the ionization parameter "U" for H II Strömgren regions, where U is proportional to the ratio of the photoionization rate to the H I formation rate via electron–proton recombination. However, αG is also a measure of the dust absorption efficiency of the H_2-dissociating photons. For the H I/H_2 density ratio in an optically thin "free-space" radiation field, αG is the ratio of the H I-dust to H_2-line absorption rates of LW-band photons that are effectively available for H_2 dissociation. For sufficiently large metallicities, this *excludes* LW photons "between the lines" that are inevitably absorbed by dust associated with just the H_2 ("H_2-dust") in a predominantly molecular and dusty cloud. As we will discuss, the mean shielding factor G depends on the competition between H_2-line absorption and H_2-dust absorption. Because of this competition, a metallicity dependence is introduced into G and therefore also into our fundamental parameter αG.

An important physical distinction occurs between the limits of small and large αG (Section 2.2.8). Small αG is the

"weak-field limit" for which H I-dust opacity is negligible and does not contribute to the absorption of the radiation, although a substantial (observable) atomic column can nevertheless exist in this limit. Large αG is the "strong-field limit" for which the atomic column becomes so large that H I-dust dominates the attenuation of the radiation fields, reducing the fraction of the incident radiation that is absorbed by the H_2.

In general, αG is the dimensionless "free parameter" in the problem, with a value that is determined by local conditions (density, radiation intensity, metallicity, etc.). However, as invoked by KMT/MK10, on global scales in star-forming galaxy disks the gas density and radiation intensity may be correlated or self-regulated to conditions enabling a two-phase equilibrium between cold and warm H I (CNM/WNM multiphase). As we describe in Section 2.2.9, this then drives αG to a narrow range, of order unity, intermediate between the weak- and strong-field limits, and only weakly dependent on the metallicity.

Finally, in Section 2.3 we extend our analysis to slabs exposed to isotropic radiation fields. An angular integration over all photodissociating ray directions is then also required in the computation of the H I column densities. Our resulting analytic expressions for the atomic columns and associated H I-dust opacities are similar to those for beamed fields, with similar behavior in the weak- and strong-field limits. Our analytic results for slabs irradiated by isotropic fields enable a direct comparison to the KMT/MK10 results for spheres, as we discuss in depth in Section 4. In Section 3 we verify our analytic results with detailed numerical model computations.

2.1. Radiation Fields and H_2 Photodissociation Rate

We will consider static, optically thick plane-parallel clouds (slabs) exposed to either isotropic or corresponding beamed LW-band radiation fields. We define the spectral range of the LW band as 912–1108 Å (11.3–13.6 eV) as appropriate for line absorptions occurring out of low-lying rotational levels in the ground vibrational state.

Let $F_\nu \equiv 4\pi I_\nu$, where I_ν is the specific photon intensity (cm^{-2} s^{-1} Hz^{-1} sr^{-1}) of an isotropic optically thin "free-space" LW radiation field. If an optically thick gas slab (or semi-infinite slab) is inserted, the flux density of the isotropic field at a cloud surface is equal to $\pi I_\nu = F_\nu/4$. The corresponding unidirectional beamed field is defined such the LW photons are normally incident on the cloud surface with flux density $2\pi I_\nu = F_\nu/2$. The surface flux of the isotropic field is half that of the corresponding beamed field, but the energy densities are equal. The energy densities at the cloud surfaces are half that in the (full 4π) free-space radiation field.

In this paper we adopt the standard Draine (1978, 2011) expression

$$\mathcal{I}_\nu^{\rm ISM} = \frac{1}{4\pi}\left\{\frac{1.068\times10^{-3}}{\lambda} - \frac{1.719\times10^{0}}{\lambda^2} + \frac{6.853\times10^{2}}{\lambda^3}\right\} \text{ photons s}^{-1}\text{ cm}^{-2}\text{ Hz}^{-1}\text{ sr}^{-1} \quad (2)$$

for the specific intensity of the isotropic free-space FUV (5–13.6 eV FUV) radiation field in the Galactic ISM. In Equation (2), λ is the photon wavelength in Angstroms. For this spectrum, the specific intensity varies by a factor of eight across the LW band. At 1000 Å, $\mathcal{I}_\nu^{\rm ISM} = 2.73\times10^{-9}$ photons s^{-1} cm^{-2} Hz^{-1} sr^{-1}, and the energy density $4\pi h\nu^2\mathcal{I}_\nu/c = 6.8\times10^{-14}$ erg cm^{-3} (where ν is the photon frequency in Hz). The total photon density in the 912–1108 Å LW band is 6.9×10^{-4} cm^{-3}.

To consider radiation fields with greater or lesser intensities, we multiply by an overall field-strength scaling factor $I_{\rm UV}$, such that $I_{\rm UV} = 1$ corresponds to the unit free-space Draine field given by Equation (2). In this paper we do not consider radiation fields with alternate spectral shapes. For completeness we recall that the Draine energy density is 1.7 times larger than the Habing (1968) estimate for the LW energy density at 1000 Å.[4]

For the free-space fields, we define the LW-band photon flux integral

$$F_0 \equiv \int_{\nu_1}^{\nu_2} F_\nu d\nu, \quad (3)$$

where ν_1 to ν_2 is the frequency range of the LW band and $F_\nu \equiv 4\pi\mathcal{I}_\nu^{\rm ISM} I_{\rm UV}$. For the Draine spectrum, $F_\nu = 3.4\times10^{-8} I_{\rm UV}$ photons s^{-1} cm^{-2} Hz^{-1} at 1000 Å, and

$$F_0 = 2.07\times10^{7}\, I_{\rm UV} \text{ photons cm}^{-2}\text{ s}^{-1}. \quad (4)$$

At the cloud surfaces, the 1000 Å flux densities are then $F_\nu/4 = 8.6\times10^{-9} I_{\rm UV}$ and $F_\nu/2 = 1.7\times10^{-8} I_{\rm UV}$ photons s^{-1} cm^{-2} Hz^{-1} for the isotropic and corresponding beamed fields. The total LW-band surface fluxes are $F_0/4 = 5.18\times10^{6} I_{\rm UV}$ and $F_0/2 = 1.03\times10^{7} I_{\rm UV}$ photons cm^{-2} s^{-1}. For a given $I_{\rm UV}$, the energy densities of the isotropic and corresponding beamed fields are equal at the cloud surfaces.

The photodissociation of H_2 occurs via line absorption of LW photons in allowed transitions from the ground electronic $X^1\Sigma_g^+$ state to the excited $B^1\Sigma_u$ or $C^1\Pi_u$ states. These are followed by rapid decays to either bound ro-vibrational levels or to the continuum of the ground X state. Decays to the continuum lead to dissociation (P. M. Solomon, private communication in Field et al. 1966; Stecher & Williams 1967; Stephens & Dalgarno 1972; Abgrall et al. 1992). The B–X and C–X bound–bound transitions are mainly to excited vibrational levels followed by a near-infrared quadrupole radiative cascade (Gould & Harwit 1963; Black & Dalgarno 1976; Shull 1978; Black & van Dishoeck 1987; S88; Sternberg & Dalgarno 1989; Draine & Bertoldi 1996; Neufeld & Spaans 1996). Thus, all of the LW-band photons absorbed by the H_2 are removed, but only a fraction of these absorptions ($\sim$10%) lead to photodissociation.

The H_2 photodissociation rate in the ISM is a fundamental quantity, and we recompute it in Section 3 by assuming the Draine spectrum for a range of assumed gas temperatures, densities, and field intensities. We find that for dissociation out of the 912–1108 Å LW band, the optically thin (full 4π) free-space photodissociation rate is

$$D_0 = 5.8\times10^{-11}\, I_{\rm UV} \text{ s}^{-1}. \quad (5)$$

[4] We note that in the classical "PDR literature," the FUV field strength is designated variously as G_0, $I_{\rm UV}$, or χ (e.g., Hollenbach et al. 1971; van Dishoeck & Black 1986; Sternberg & Dalgarno 1989; Draine & Bertoldi 1996). In this paper we adopt $I_{\rm UV}$ for the field strength to avoid confusion with the "αG factor" defined in Section 2.2.5 or with the KMT/MK10 "χ," which as we discuss in Section 4 is equivalent to our αG in the low-metallicity limit. The adopted normalizations can be confusing. For example, in the classic Tielens & Hollenbach (1985) paper, $G_0 = 1$ refers to an FUV field for which the energy density at the surface of an optically thick cloud is equal to the energy density in the free-space (all 4π) Habing (1968) field. That is, $G_0 = 0.5$ for an optically thick slab embedded in a unit (isotropic) Habing field. With our definitions, $I_{\rm UV} = 1$ (not 0.5) for a cloud inserted into a unit isotropic Draine field with $I_\nu = I_\nu^{\rm ISM}$ or for a cloud illuminated by a corresponding beamed field with surface flux density $F_\nu = 2\pi I_\nu^{\rm ISM}$. For $I_{\rm UV} = 1$, the H_2 photodissociation rates at the cloud surfaces are equal to half the full 4π "free-space" rate in a unit Draine field (see also Equation (5)).

At a cloud surface the dissociation rate, $D(0) \equiv D_0/2$, is half the free-space rate and

$$D(0) = 2.9 \times 10^{-11} I_{\rm UV}\ {\rm s}^{-1}. \quad (6)$$

Because the dissociation rate is proportional to the radiation energy density, the dissociation rates for isotropic and corresponding beamed fields are identical at a cloud surface.

The photodissociation rate diminishes with cloud depth due to the combination of H_2-line and dust absorptions. The attenuation of the LW radiation field is crucial in determining the depth dependence of the atomic and molecular densities, the shapes of the H I-to-H_2 transition profiles, and the resulting atomic hydrogen column densities. The depth-dependent attenuation depends on the assumed field geometry, and we analyze the behavior for both beamed and isotropic fields, starting with beamed fields which are simpler.

2.2. Beamed Fields

We consider the H I-to-H_2 transition and total column density of atomic hydrogen on one side of an optically thick plane-parallel slab of gas (or semi-infinite slab) that is exposed to a steady flux of LW-band photons normally incident on the cloud surface as unidirectional beamed radiation.

2.2.1. Dissociation Bandwidth and Self-shielding Function

Let N_2 be the H_2 column density (cm^{-2}) at some depth normal to the cloud surface. Then, neglecting dust absorption of the LW photons, and for beamed radiation, the photodissociation rate (s^{-1}) for a single LW absorption line ℓ may be written as

$$D_\ell(N_2) = \frac{1}{2}\int_0^\infty F_\nu\ \sigma_{\nu,d}\ e^{-\sigma_\nu N_2}\ d\nu = \frac{1}{2} F_\nu\ \frac{dW_{\ell,d}}{dN_2}, \quad (7)$$

where

$$W_{\ell,d}(N_2) \equiv \int_0^\infty [1 - \frac{\sigma_{\nu,d}}{\sigma_\nu} e^{-\sigma_\nu N_2}]\ d\nu. \quad (8)$$

In these expressions, $F_\nu/2 = 2\pi \mathcal{I}_\nu^{\rm ISM} I_{\rm UV}$ is the incident beamed flux density (photons cm^{-2} s^{-1} Hz^{-1}) at the cloud surface, $\sigma_{\nu,d}$ is the cross section (cm^2) for absorptions that lead to molecular dissociation,[5] and σ_ν is the cross section for all photon absorptions (not just those that are followed by dissociation). The dissociation probabilities, $f_{\rm diss} \equiv \sigma_{\nu,d}/\sigma_\nu$, range from $\sim$0 to more than 0.5 for individual LW transitions depending on the rotational quantum number in the excited B or C states. The mean (typical) dissociation probability averaged over all lines is $\langle f_{\rm diss}\rangle = 0.12$. For a single absorption line,

$$\sigma_d \equiv \int \sigma_{\nu,d}\ d\nu = \ f_{\rm diss}\ \frac{\pi e^2}{m_e c}\ f_{\rm osc}\ \simeq\ 2.7 \times 10^{-5}\ {\rm cm}^2\ {\rm Hz} \quad (9)$$

for a typical LW-band oscillator strength of $f_{\rm osc} \approx 0.01$ and dissociation probability of $f_{\rm diss} \approx 0.1$ (and where e and m_e are the electron charge and mass, and c is the speed of light).

In Equation (7), we pull F_ν out of the integral because we assume that the flux density varies very slowly over the narrow line profile (as represented by σ_ν). In Equation (8), $W_{\ell,d}(N_2)$ is defined as the "equivalent bandwidth" (Hz) of radiation absorbed in H_2 dissociations via absorption line ℓ, up to *molecular* column N_2. The dissociation rate $D_\ell(N_2)$ decreases with the molecular column N_2 as the absorption line become optically thick, and the ratio

$$f_{\ell,{\rm shield}}(N_2)\ \equiv\ \frac{D_\ell(N_2)}{D_\ell(0)} = \frac{1}{\sigma_d}\ \frac{dW_{\ell,d}}{dN_2} \quad (10)$$

is the individual H_2-line "self-shielding" function. It quantifies the reduction of the line dissociation rate, where $D_\ell(0)$ is the line dissociation rate at the cloud surface. By definition, the self-shielding function is proportional to the derivative of the dissociation bandwidth $W_{\ell,d}$ (Federman et al. 1979; van Dishoeck & Black 1986; S88; Draine & Bertoldi 1996).

For the full multiline LW-band system, the dissociation rate (again neglecting dust absorption) may be written compactly as

$$D(N_2) = \frac{1}{2}\bar{F}_\nu\ \frac{dW_d}{dN_2}, \quad (11)$$

where $W_d(N_2)$ is the equivalent dissociation bandwidth *summed* over all of the (possibly overlapping) absorption lines, and $\bar{F}_\nu$ is a mean flux density. A plot of W_d versus N_2 is the effective "curve of growth" for the dissociating LW radiation bandwidth in a dust-free cloud. We present computations for $W_d(N_2)$ in Section 3 (the blue curve in Figure 3).

The mean flux density in Equation (11) is given by

$$\bar{F}_\nu\ \equiv\ 4\pi \frac{\sum I_{\nu_{ij}} x_i \sigma_d^{ij}}{\sum x_i \sigma_d^{ij}}. \quad (12)$$

Here x_i are the fractional populations of H_2 molecules in ro-vibrational levels i of the ground electronic X state, $I_{\nu_{ij}}$ is the (full 4π) free-space specific intensity at frequencies ν_{ij} of LW-band transitions between level i and levels j in the excited B or C states, and σ_d^{ij} are the absorption line dissociation cross sections (cm^2 Hz). The mean flux density $\bar{F}_\nu$ is weighted by the relative strengths of the dissociation transitions. For the Draine spectrum, $\bar{F}_\nu = 2.46 \times 10^{-8} I_{\rm UV}$ photons cm^{-2} s^{-1} Hz^{-1}.

The denominator in expression (12) is the total (frequency integrated) H_2 dissociation cross section (cm^2 Hz) summed over all absorption lines,

$$\sigma_d^{\rm tot} \equiv \sum x_i \sigma_d^{ij}. \quad (13)$$

Most of the H_2-line absorptions occur out of the lowest few rotational levels, and the total effective dissociation cross section is insensitive to the fractional populations x_i. We find that

$$\sigma_d^{\rm tot} = 2.36 \times 10^{-3}\ \ {\rm cm}^2\ {\rm Hz}. \quad (14)$$

The ratio $\sigma_d^{\rm tot}/\sigma_d\ \simeq\ 80$ is then the approximate number of strong LW absorption lines involved in the multiline H_2 photodissociation process (see also Figure 2 in Section 3).

With these definitions, the free-space photodissociation rate may be expressed as

$$D_0 = \bar{F}_\nu\ \sigma_d^{\rm tot}. \quad (15)$$

At a cloud surface the photodissociation rate is $D(0) \equiv D_0/2 = (1/2)\bar{F}_\nu\ \sigma_d^{\rm tot}$. The ratio

$$f_{\rm shield}(N_2)\ \equiv\ \frac{D(N_2)}{D(0)} = \frac{1}{\sigma_d^{\rm tot}}\ \frac{dW_d}{dN_2} \quad (16)$$

[5] In our notation, the subscript "d" refers to H_2 photodissociation. Thus, $\sigma_{\nu,d}$ is the cross section for line absorption followed by dissociation. The subscript "g" refers to dust grains. Thus, σ_g is the FUV dust grain absorption cross section (Section 2.2.2).

is then the complete multiline H_2 "self-shielding" function. It quantifies the reduction of the total dissociation rate due opacity in all of the absorption lines.

For a single line the self-shielding function varies as $N_2^{-1/2}$ for large N_2 because absorptions can always occur far out on the Lorentzian damping wings.[6] Therefore, for a single absorption line, $W_{\ell,d}$ as given by Equation (8) diverges as $N_2^{1/2}$. For strong lines (with $f_{\rm osc} \sim 0.01$), this "square root" part of the curve of growth begins when $N_2 \gtrsim 10^{17}$ cm^{-2}. For the realistic multiline system, the absorption lines will overlap for sufficiently large ($\gtrsim 5 \times 10^{20}$ cm^{-2}) molecular columns, and W_d does not diverge as does $W_{\ell,d}$. For the multiline system, the total dissociation bandwidth

$$W_{d,\rm tot} \equiv \int_0^\infty \frac{dW_d}{dN_2}\, dN_2 \tag{17}$$

is limited to a finite maximal value (even in the absence of dust). We find that for the Draine spectrum $W_{d,\rm tot} = 9.1 \times 10^{13}$ Hz (as computed in Section 3.1.2). In Section 3.1.3 we present our computations for the multiline self-shielding function (Figure 5). At the cloud surface, $f_{\rm shield} = 1$. As the Doppler cores become optically thick at $N_2 \gtrsim 10^{14}$ cm^{-2}, $f_{\rm shield}$ becomes small and the molecules are then said to self-shield against the dissociating radiation. The decline is more gradual at intermediate columns, 10^{17} to 10^{22} cm^{-2}, for which most of the absorption is out of the line wings. Finally, as line overlap occurs and the dissociating radiation is fully absorbed, $f_{\rm shield}$ becomes vanishingly small.

In the limit of complete line overlap, every photon in the (912–1108 Å) LW band is absorbed in H_2-lines. The product $(1/2)\bar{F}_\nu W_{d,\rm tot}$ is then the LW "dissociation flux" (photons cm^{-2} s^{-1}) at the cloud surface. In the absence of dust absorption, this flux is equal to the H_2 dissociation rate per unit area. For complete absorption of the LW-band radiation, the mean dissociation probability is

$$\bar{f}_{\rm diss} = \frac{\bar{F}_\nu W_{d,\rm tot}}{F_0}, \tag{18}$$

where $F_0/2$ is the total incident LW-band flux. For the radiative transfer computations we present in Section 3, we find that $\bar{f}_{\rm diss} = 0.12$ and is essentially equal to the simple average over the individual line dissociation probabilities for the matrix of *X–B* and *X–C* transitions. Our result for $\bar{f}_{\rm diss}$ is consistent with many previous calculations (e.g., Black & van Dishoeck 1987; Draine & Bertoldi 1996; Browning et al. 2003).

2.2.2. Dust and Metallicity

In addition to the H_2-line absorptions, the LW-band photons are also absorbed by dust grains, further reducing the photodissociation rate. We assume that the dust is mixed uniformly with the gas with a dust-to-gas mass ratio that depends linearly on the metallicity of the cloud. For the grain–photon interaction, we assume pure absorption and no scattering (or equivalently only forward scattering). With the inclusion of dust, the local dissociation rate, D, at any cloud depth is then

$$D = \frac{1}{2} D_0\, f_{\rm shield}(N_2)\, e^{-\tau_g}, \tag{19}$$

where D_0 is the free-space dissociation rate (Equation (5)). In this expression, $\tau_g \equiv \sigma_g N$ is the dust continuum optical depth, where $N \equiv N_1 + 2N_2$ is the column density of hydrogen nuclei, in molecules *plus* atoms. Here σ_g is the dust grain LW-photon absorption cross section (cm^2) per hydrogen nucleon. With the inclusion of dust attenuation, the dissociation rate given by Equation (19) depends on both N_2 *and* the column density of atomic hydrogen N_1.

For simplicity we also assume that σ_g is independent of photon frequency over the narrow LW band. For a standard interstellar extinction curve, with a total-to-selective extinction ratio of $R_V \equiv A_V/E(B-V) = 3.1$, a 1000 Å grain albedo ≈ 0.3, and a scattering asymmetry factor $\langle \cos\theta \rangle \approx 0.6$, the effective absorption cross section per hydrogen nucleus $\sigma_g = 1.9 \times 10^{-21}$ cm^2 (Draine 2003); $R_V = 3.1$ is for diffuse gas (with densities $n \sim 10^2$ cm^{-3}). For $R_V = 3.1$, $A_V/N = 5.35 \times 10^{-22}$ mag cm^2. In dense regions ($n \gtrsim 10^3$ cm^{-3}), R_V can be larger (up to ~5.8) but with an extinction curve that is less steep toward the ultraviolet, with $\sigma_g \approx 8 \times 10^{-22}$ cm^{-2} (Cardelli et al. 1989; Fitzpatrick 1999; Draine & Bertoldi 1996; Draine 2011). With the assumption that the dust-to-gas mass ratio is linearly proportional to the metallicity Z' of the gas, we therefore set

$$\sigma_g = 1.9 \times 10^{-21} \phi_g\, Z'\ {\rm cm}^2 \tag{20}$$

where $Z' = 1$ corresponds to the solar photospheric abundances of the heavy elements ("solar metallicity") and where ϕ_g of order unity depends on the grain composition and size distribution.

Dust grains are also essential for H_2 formation (Hollenbach et al. 1971; Jura 1974; Barlow & Silk 1976; Leitch-Devlin & Williams 1985; Pirronello et al. 1997; Takahashi et al. 1999; Cazaux & Tielens 2002; Habart et al. 2004). We assume that per hydrogen nucleon the rate coefficient for H_2 formation on grains is given by

$$R = 3 \times 10^{-17} \left(\frac{T}{100\ {\rm K}}\right)^{1/2} Z'\ {\rm cm}^3\ {\rm s}^{-1}, \tag{21}$$

where T is the gas temperature in °K. Our standard value is then $R = 3 \times 10^{-17}$ cm^3 s^{-1} for $T = 100$ K and $Z' = 1$.

2.2.3. H I/H$_2$ Formation–Destruction Equation

For a steady state in which molecular photodissociation is balanced everywhere by grain surface H_2 formation, the H I/H_2 formation–destruction equation may be written as

$$Rn\, n_1 = \frac{1}{2}\bar{F}_\nu \frac{dW_d}{dN_2}\, e^{-\tau_g}\, n_2 = \frac{1}{2} D_0\, f_{\rm shield}(N_2)\, e^{-\tau_g}\, n_2. \tag{22}$$

In this equation, n_1 and n_2 are the local volume densities (cm^{-3}) of the H I atoms and H_2 molecules, and

$$n \equiv n_1 + 2n_2 \tag{23}$$

is the total volume density of hydrogen nuclei. The right-hand side of Equation (22) is the H_2 photodissociation rate per unit volume (s^{-1} cm^{-3}) at some cloud depth where the rate is reduced by the combined effects of self-shielding and dust attenuation. The left-hand side is the rate per unit volume of H_2 formation on dust grains. We ignore all other formation or destruction processes (such as formation in the gas phase or destruction by X-ray or cosmic-ray ionization).

Given the free parameters n, D_0 (or equivalently $I_{\rm UV}$), R, and σ_g (or given Z', which determines R and σ_g), Equation (22)

[6] This can be seen directly from Equation (7). For damped lines, σ_ν and $\sigma_{\nu,d}$ are proportional to ν^{-2}, and the integral over frequency is then proportional to $N_2^{-1/2}$.

together with particle conservation Equation (23) can be solved for the local atomic and molecular densities n_1 and n_2 and for the integrated atomic and molecular columns N_1 and N_2. If it is assumed that the incident LW radiation is fully absorbed, then (as we show below) Equation (22) gives our fundamental formula for the total atomic column that is maintained in the cloud.

The density ratio $n_1/n_2 = dN_1/dN_2$, and Equation (22) may be written as the separable differential equation (S88; see also Jura 1974; Hill & Hollenbach 1978):

$$Rn\, e^{\sigma_g N_1}\, dN_1 = \frac{1}{2}\bar{F}_\nu \frac{dW_d}{dN_2}\, e^{-2\sigma_g N_2}\, dN_2. \quad (24)$$

In writing the formation–destruction equation this way, a key insight is that the dust opacities associated with the atomic and molecular columns can be considered *separately*. We will refer to "H_2-dust" or "H I-dust" as the dust opacities associated with either just the H_2 or the H I gas, respectively, *whether or not the H I gas is mixed with the H_2*.

Integrating this expression and assuming that R and n are constants (i.e., do not vary with cloud depth) gives

$$Rn \int_0^{N_1} e^{\sigma_g N_1'}\, dN_1' = \frac{1}{2}\bar{F}_\nu \int_0^{N_2} \frac{dW_d}{dN_2'}\, e^{-2\sigma_g N_2'}\, dN_2', \quad (25)$$

which is a functional relationship, $N_1(N_2)$, between the atomic and molecular column densities. We note that the independent variable parameterizing the cloud depth is here chosen to be N_2 rather than the total gas column density N. Choosing N_2 as the independent variable is essential for our analysis, even though it is N that is proportional to the visual extinction A_V, or to the length scale $z \equiv N/n$.

2.2.4. H_2-dust-limited Dissociation Bandwidth

Most importantly, for a given value of σ_g, the integral on the right-hand side of Equation (25),

$$W_g(N_2) \equiv \int_0^{N_2} \frac{dW_d}{dN_2'}\, e^{-2\sigma_g N_2'}\, dN_2', \quad (26)$$

is a function of the molecular column N_2 only. This is because the exponential cutoff factor in the integrand is due to H_2-dust opacity only—it excludes H I-dust—and because W_d itself depends only on N_2. Furthermore, $W_g(N_2)$ is only very weakly dependent on n, R, or D_0 and is essentially independent of these parameters (see Section 3). So, for a given σ_g, the effective equivalent width $W_g(N_2)$ is a quantity that can be calculated *in advance* as a "universal dust-limited curve of growth" for the H_2-line absorption of LW radiation, independent of the other parameters, n, R, and D_0, that together with σ_g determine the depth-dependent H I/H_2 density ratios and the H I-to-H_2 transition profiles.

Thus, $W_g(N_2)$ (as opposed to $W_d[N_2]$) is the effective bandwidth of dissociating LW radiation in a *dusty* H_2 cloud, where now this bandwidth is limited by *H_2-dust* absorption of LW photons that would otherwise be available for H_2 photodissociation in a dust-free cloud. H_2-dust opacity is important if it becomes large before the H_2 absorption lines can fully overlap. For sufficiently small σ_g, the lines do overlap completely, and then $W_g(N_2) = W_d(N_2)$. For sufficiently large σ_g, the H_2-dust provides a cutoff, and then $W_g(N_2) < W_d(N_2)$ at large N_2.

It is a remarkable physical coincidence that the H_2 column density at which the H_2-lines begin to overlap—a column that depends on the internal molecular oscillator strengths and energy level spacings—is comparable to the H_2 column at which the H_2-dust opacity $2N_2\sigma_g \gtrsim 1$ for standard interstellar dust absorption cross sections. Thus, both regimes of "small σ_g" and "large σ_g" for the dissociation bandwidth $W_g(N_2)$ are relevant for the range of interstellar dust properties and metallicities in galaxies. In Section 3.1.2, we present computations of $W_g(N_2)$ for a wide range of σ_g encompassing these regimes.

As $N_2 \to \infty$, the equivalent width $W_g(N_2)$ converges to a finite limit

$$W_{g,\rm tot}(\sigma_g) \equiv \int_0^\infty \frac{dW_d}{dN_2}\, e^{-2\sigma_g N_2}\, dN_2, \quad (27)$$

either because the exponential H_2-dust attenuation factor cuts off the integrand (for large σ_g) or because dW_d/dN_2 itself vanishes as the lines overlap (for small σ_g). Thus, $W_{g,\rm tot}(\sigma_g)$ is the *total H_2-dust-limited effective dissociation bandwidth*. For large σ_g, $W_{g,\rm tot} < W_{d,\rm tot}$, and for small σ_g, $W_{g,\rm tot} = W_{d,\rm tot}$. For large σ_g, the absorption lines remain separated but are nevertheless highly damped for most of the integration range up to the H_2-dust cutoff.

For a single absorption line, $dW_d/dN_2 \propto N_2^{-1/2}$ in the damped regime, and it follows from Equation (27) that $W_{g,\rm tot}(\sigma_g)$ scales as $\sigma_g^{-1/2}$. Our numerical computations (Section 3.1.2) show that for large σ_g this scaling behavior is maintained in the full multiline problem to a good approximation. In Section 3, we find that the simple formula

$$W_{g,\rm tot}(\sigma_g) \simeq \frac{9.9\times10^{13}}{1+(\sigma_g/\,7.2\times10^{-22}\ {\rm cm}^2)^{1/2}}\ {\rm Hz} \quad (28)$$

is an excellent fit to our numerical radiative transfer results. The normalized H_2-dust-limited dissociation bandwidth

$$w \equiv \frac{W_{g,\rm tot}}{W_{d,\rm tot}} \simeq \frac{1}{1+(\sigma_g/\,7.2\times10^{-22}\ {\rm cm}^2)^{1/2}} = \frac{1}{1+(2.64\phi_g Z')^{1/2}}, \quad (29)$$

where in the last equality we have assumed $\sigma_g = 1.9\times10^{-21}\phi_g Z'$ (Equation (20)). In these expressions, $W_{g,\rm tot} \to W_{d,\rm tot}$ and $w \to 1$ for small σ_g (low metallicity) and decrease as $\sigma_g^{-1/2}$ for large σ_g (high metallicity). The normalized bandwidth w decreases from 0.9 to 0.2 for σ_g ranging from 1×10^{-23} cm^{-2} (small) to $\sim6\times10^{-21}$ cm^{-2} (large) or for Z' ranging from $\sim$0.01 to 3 (assuming $\sigma_g \propto Z'$), which is the relevant range for galaxies.

2.2.5. Effective Dissociation Flux and Dissociation Probability

Given Equation (18), we may now write

$$\bar{F}_\nu W_{g,\rm tot} = w\,\bar{f}_{\rm diss} F_0, \quad (30)$$

and define the effective dissociation probability

$$\bar{p}_{\rm diss} \equiv \frac{\bar{F}_\nu W_{g,\rm tot}}{F_0} \equiv w\,\bar{f}_{\rm diss}. \quad (31)$$

The product $(1/2)\bar{F}_\nu W_{g,\rm tot}$ is the "effective dissociation flux" for dusty clouds in which H_2-dust may absorb some of the incident LW radiation. The effective dissociation flux depends

on the competition between H_2-line absorption and H_2-dust absorption as given by the dependence of $W_{g,\rm tot}$ on σ_g. The effective dissociation flux is the H_2 photodissociation rate per unit surface area for a dusty and optically thick molecular slab in which H I-dust opacity is negligible.

When H_2-dust is negligible, $w = 1$ and $\bar{p}_{\rm diss} = \bar{f}_{\rm diss}$. When H_2-dust opacity is significant, $w < 1$ and $\bar{p}_{\rm diss} < \bar{f}_{\rm diss}$. The effective dissociation probability $\bar{p}_{\rm diss}$ is the fraction of the total 912–1108 Å LW-band flux that is absorbed in H_2 photodissociation events in a dusty, optically thick, predominantly molecular slab (with vanishing H I-dust opacity). For low Z', $\bar{p}_{\rm diss} = 0.12$ is a constant. For high Z', $\bar{p}_{\rm diss}$ decreases as $Z'^{-1/2}$.

2.2.6. Formula for the H I Column Density

Returning now to Equation (25), it follows that

$$Rn \int_0^{N_1} e^{\sigma_g N_1'} dN_1' = \frac{1}{\sigma_g} Rn[e^{\sigma_g N_1} - 1] = \frac{1}{2} \bar{F}_\nu W_g(N_2) \quad (32)$$

or

$$N_1(N_2) = \frac{1}{\sigma_g} \ln\left[\frac{1}{2}\frac{\sigma_g \bar{F}_\nu W_g(N_2)}{Rn} + 1\right]. \quad (33)$$

Following S88, we now define the dimensionless parameter

$$\alpha \equiv \frac{D_0}{Rn} = \frac{\sigma_d^{\rm tot} \bar{F}_\nu}{Rn}, \quad (34)$$

where D_0 is the *free-space* dissociation rate,[7] and we define the dimensionless "G integral"

$$G(N_2) \equiv \sigma_g \int_0^{N_2} f_{\rm shield}(N_2')\, e^{-2\sigma_g N_2'}\, dN_2' = \frac{\sigma_g}{\sigma_d^{\rm tot}} W_g(N_2). \quad (35)$$

We can then write

$$N_1(N_2) = \frac{1}{\sigma_g} \ln\left[\frac{\alpha G(N_2)}{2} + 1\right], \quad (36)$$

where

$$\alpha G(N_2) = \frac{\sigma_g \bar{F}_\nu W_g(N_2)}{Rn}. \quad (37)$$

Given the "universal" dust-limited curve of growth $W_g(N_2)$, which can be computed "in advance" for any σ_g, the atomic column is then given by Equation (36) (or Equation (33)) for any surface dissociation rate D_0 (or $I_{\rm UV}$), rate coefficient R, and density n.

We refer to Equation (36) as the "semi-analytic integral H I-to-H_2 profile." It shows that the H I column at any depth depends on only two quantities—σ_g and $\alpha G(N_2)$. In dimensionless form

$$\tau_1(\tau_2) = \ln\left[\frac{\alpha G(\tau_2)}{2} + 1\right], \quad (38)$$

where $\tau_2 \equiv 2\sigma_g N_2$ is the dust optical depth associated with the molecular column, and $\tau_1(\tau_2) \equiv \sigma_g N_1$ is the H I-dust optical depth at τ_2.

As $N_2 \to \infty$, $W_g(N_2) \to W_{g,\rm tot}$. The *total* atomic column density is therefore finite and is given by

$$N_{1,\rm tot} = \frac{1}{\sigma_g} \ln\left[\frac{1}{2}\frac{\sigma_g \bar{F}_\nu W_{g,\rm tot}}{Rn} + 1\right] = \frac{1}{\sigma_g} \ln\left[\frac{1}{2}\bar{f}_{\rm diss}\frac{\sigma_g w F_0}{Rn} + 1\right] \quad (39)$$

or

$$N_{1,\rm tot} = \frac{1}{\sigma_g} \ln\left[\frac{\alpha G}{2} + 1\right]. \quad (40)$$

Here the dimensionless parameter

$$G(\sigma_g) \equiv \frac{\sigma_g}{\sigma_d^{\rm tot}} W_{g,\rm tot}(\sigma_g) \quad (41)$$

is the limit of $G(N_2)$ as $N_2 \to \infty$, so that

$$\alpha G = \frac{D_0 G}{Rn} = \frac{\sigma_g \bar{F}_\nu W_{g,\rm tot}}{Rn} = \bar{f}_{\rm diss}\frac{\sigma_g w F_0}{Rn}. \quad (42)$$

We discuss these and additional expressions for αG in Section 2.2.6 below.

Equation (40) for the total H I column on one side of an optically thick cloud was first derived by S88 (see Equation (9) of that paper), and it is the fundamental relation in our analysis.[8] The basic assumption is that all of the dissociating LW-band radiation is absorbed, as in a classical "ionization-bounded" H II region or layer (Strömgren 1939). However, because of the three-way competition between H I-dust, H_2-dust, and H_2-lines, the behavior for H I is more complicated than for H II. For a steady (dust-free) photoionized planar Strömgren layer, the H II column equals the ratio of the Lyman continuum flux to the recombination rate, independent of the photoionization cross section. Similarly, in our Equation (39) or Equation (40), the H_2-line absorption cross section does not appear explicitly (although it is implicit in our definition of the effective dissociation flux). The H I column depends on the ratio of the effective dissociation flux to the H_2 formation rate, but this ratio is multiplied by the dust absorption cross section and appears inside a logarithm. We discuss this behavior, and the connection to Strömgren relations, in our description of the weak- and strong-field limits in Section 2.2.8.

In dimensionless form, the total H I-dust optical depth associated with the total *atomic* column is

$$\tau_{1,\rm tot} = \ln\left[\frac{\alpha G}{2} + 1\right]. \quad (43)$$

The total H I-dust optical depth depends on the single dimensionless parameter αG constructed from the cloud variables D_0 (or F_0 or $I_{\rm UV}$), n, R, and σ_g (or Z', which determines R and σ_g).

The total gas column $N \equiv N_1(N_2) + 2N_2$. It therefore follows from Equation (36) that the atomic column as a function of the total (atomic plus molecular) column, $N_1(N)$, also depends on just σ_g and αG. Similarly, for $\tau_g \equiv \sigma_g N$, the H I-dust optical depth $\tau_1(\tau_g)$ depends on the single dimensionless parameter αG. Then, since $n_1/n_2 \equiv dN_1/dN_2$ it follows that the *shapes* of the H I-to-H_2 transition profiles are *invariant* for identical αG. That is, the density fractions n_1/n and $2n_2/n$ expressed as functions

[7] In S88, α was defined with the surface dissociation rate $D(0) = D_0/2$ in the numerator. In this paper we adjust the definition and instead use D_0 for a clear comparison of planar and spherical geometries as presented in Section 4. With this adjustment, factors of 1/2 appear in our formulae.

[8] The main goal and result of S88 was an analytic formula for the intensity of UV excited (fluorescent) IR H_2 emission lines from PDRs. Because the FUV-pumped H_2 vibrational excitation rate is proportional to the dissociation rate, the IR intensity is proportional to the H I column density, as expressed in Equation (10) of that paper.

of the dust optical depth τ_g (or visual extinction A_V) depend on just the single dimensionless parameter αG.

In Section 3.1.4 we present detailed numerical computations for the H I-to-H_2 transition profiles. We show that the transitions are "gradual" when $\alpha G \ll 1$ and are "sharp" when $\alpha G \gg 1$. An essential feature of our derivation and analytic expression for the total H I column is that no assumptions need to be made on the shape of the H I-to-H_2 transition profile. Our Equation (39) or Equation (40) are universally valid for all profile shapes, gradual or sharp.

2.2.7. αG

It is useful to consider the physical meaning of the dimensionless parameters α and G and their product αG.

First, α is the ratio of the unattenuated free-space H_2 photodissociation rate to the H_2 formation rate and can be expressed as

$$\alpha = 1.93 \times 10^4 \left(\frac{D_0}{5.8 \times 10^{-11}\ \mathrm{s^{-1}}}\right)\left(\frac{3 \times 10^{-17}\ \mathrm{cm^3\ s^{-1}}}{R}\right) \times \left(\frac{100\ \mathrm{cm^{-3}}}{n}\right). \quad (44)$$

Thus, α is just the free-space atomic-to-molecular density ratio n_1/n_2, and $\alpha/2$ is the density ratio at the surface of an optically thick slab. For a characteristic interstellar cloud gas density $n \sim 10^2\ \mathrm{cm^{-3}}$, and with $D_0 = 5.8 \times 10^{-11} I_{\rm UV}\ \mathrm{s^{-1}}$, the atomic-to-molecular density ratio is $n_1/n_2 \gg 1$ at the cloud edge in the absence of shielding, unless $I_{\rm UV}$ is unrealistically small. Conversion to the molecular phase in the ISM generally requires significant attenuation of the ambient and destructive radiation fields.

Now consider the parameter G. Defining the H_2-dust opacity $\tau_2 \equiv 2\sigma_g N_2$ (see Equation (35)),

$$G = \frac{1}{2}\int_0^\infty f_{\rm shield}(\tau_2) e^{-\tau_2}\, d\tau_2 \equiv \frac{1}{2}\langle f_{\rm shield}\rangle \approx \frac{1}{2}\int_0^1 f_{\rm shield}(\tau_2)\, d\tau_2. \quad (45)$$

Thus, G is the *average* H_2 self-shielding factor. The average is over an H_2 column for which the H_2-dust opacity $\tau_2 \approx 1$. Thus, $(1/2)D_0 G$ is the characteristic photodissociation rate for self-shielded H_2 in a fully molecular cloud, prior to the onset of any H_2-dust attenuation. Because $f_{\rm shield}$ is already $\ll 1$ for $\tau_2 \ll 1$, the H_2 molecules are very self-shielded for an H_2-dust opacity $\tau_2 \sim 1$, and G is generally very small.

The product $\alpha G/2 = (1/2)D_0 G/Rn$ is then the atomic-to-molecular density ratio n_1/n_2 for the average *shielded* H_2 dissociation rate. This is our first interpretation for αG (and as adopted in S88). If $n_1 > 2n_2$ for the shielded dissociation rate, then H I-dust must also contribute to the attenuation of the LW radiation since then $\tau_1 > \tau_2$ within the H_2-dust attenuation column. If $n_1 \ll 2n_2$, then H I-dust attenuation is negligible.

Alternatively, $G \equiv \sigma_g W_{g,\rm tot}/\sigma_d^{\rm tot}$ (Equation (41)) is the ratio of the UV continuum dust absorption cross section ($\mathrm{cm^2}$) to the total H_2-line dissociation cross section ($\mathrm{cm^2\ Hz}$) averaged over the effective dissociation bandwidth (Hz). Again, G is generally very small because H_2-line absorption is so much more efficient than dust absorption. Given $\sigma_g = 1.9 \times 10^{-21} \phi_g Z'\ \mathrm{cm^2}$ (Equation (20)) and our expression (28) for $W_{g,\rm tot}$, and with $\sigma_d^{\rm tot} = 2.36 \times 10^{-3}\ \mathrm{cm^2\ Hz}$, we have

$$G \simeq \frac{7.97 \times 10^{-5} Z' \phi_g}{1 + (2.64 Z' \phi_g)^{1/2}}. \quad (46)$$

For example, for standard values $Z' = 1$ and $\phi_g = 1$, Equation (46) gives $G = 3.0 \times 10^{-5}$ and the shielded H_2 dissociation rate $(1/2)D_0 G = 8.7 \times 10^{-16} I_{\rm UV}\ \mathrm{s^{-1}}$. For low metallicity, small σ_g, it follows that $G \propto Z'$ (or $G \propto \sigma_g$). For high metallicity, large σ_g, $G \propto Z'^{1/2}$ (or $G \propto \sigma_g^{1/2}$).

Since α is the free-space atomic-to-molecular density ratio, we have

$$\alpha G = \left.\frac{\sigma_g W_{g,\rm tot}}{\sigma_d^{\rm tot}}\frac{n_1}{n_2}\right|_{\rm freespace} = \left.\frac{\sigma_g \bar{F}_\nu W_{g,\rm tot} n_1}{D_0 n_2}\right|_{\rm freespace} = \left.\frac{\bar{f}_{\rm diss} w F_0 \sigma_g n_1}{D_0 n_2}\right|_{\rm freespace}, \quad (47)$$

where in the second and third equalities we have used the relations $D_0 \equiv \sigma_d^{\rm tot}\bar{F}_\nu$ and $\bar{F}_\nu W_{g,\rm tot} \equiv \bar{f}_{\rm diss} w F_0$. This gives our second interpretation for αG. It is the free-space ratio of the H I-dust to H_2-line absorption rates of LW photons in the H_2-dust-limited dissociation band.

Third, since $D_0 G = \bar{f}_{\rm diss}\sigma_g w F_0$ (and $\bar{p}_{\rm diss} \equiv w\bar{f}_{\rm diss}$), we have

$$\alpha G = \bar{f}_{\rm diss}\frac{\sigma_g w F_0}{Rn} = \bar{p}_{\rm diss}\frac{\sigma_g F_0}{Rn}. \quad (48)$$

Thus, αG is the free-space ratio of the dust absorption rate of the effective dissociation flux—*per hydrogen atom*—to the molecular formation rate per atom.

When $\alpha G \ll 1$, H I-dust plays no role anywhere in the cloud, since it is negligible even for the free-space field where the atomic density is largest. However, when $\alpha G \gg 1$, H I-dust becomes important and absorbs an increasing fraction of the LW photons that are otherwise available for H_2 photodissociation.

Thus, with Equations (44) and (46),

$$\alpha G = 1.54 \left(\frac{D_0}{5.8 \times 10^{-11}\ \mathrm{s^{-1}}}\right)\left(\frac{3 \times 10^{-17}\ \mathrm{cm^3\ s^{-1}}}{R}\right) \times \left(\frac{100\ \mathrm{cm^{-3}}}{n}\right)\frac{\phi_g Z'}{1 + (2.64\phi_g Z')^{1/2}}, \quad (49)$$

or with Equation (48),

$$\alpha G = 1.54 \left(\frac{\sigma_g}{1.9 \times 10^{-21}\ \mathrm{cm^2}}\right)\left(\frac{F_0}{2.07 \times 10^7\ \mathrm{cm^{-2}\ s^{-1}}}\right) \times \left(\frac{3 \times 10^{-17}\ \mathrm{cm^3\ s^{-1}}}{R}\right)\left(\frac{100\ \mathrm{cm^{-3}}}{n}\right) \times \frac{1}{1 + (2.64\phi_g Z')^{1/2}}. \quad (50)$$

With Equation (4) or Equation (5) for F_0 or D_0, and Equations (20) and (21) for σ_g and R, we then have

$$\alpha G = 1.54 \frac{I_{\rm UV}}{(n/100\,\mathrm{cm^{-3}})}\frac{\phi_g}{1 + (2.64\phi_g Z')^{1/2}}. \quad (51)$$

For σ_g and R varying the same way with Z' there is a cancellation, but a metallicity dependence still remains via the dissociation bandwidth w (Equation (29)) and its dependence on the competition between H_2-dust absorption and H_2-line absorption. For low Z' (complete line overlap limit, $w = 1$), αG is independent of the metallicity, but for high Z', $w \sim \sigma_g^{-1/2}$ and $\alpha G \sim Z'^{-1/2}$.

2.2.8. Weak- and Strong-field Limits

Expression (51) also shows that the regimes of large and small αG are both relevant for the widely varying conditions in localized environments of the ISM in galaxies. For example, $I_{\rm UV}$ can range from $\sim$1 at "average" locations to $\gtrsim 10^5$ near hot stars, whereas n can range from $\sim$10 cm^{-3} in diffuse gas to $\gtrsim 10^6$ cm^{-3} in dense molecular clouds. On global scales in star-forming galaxy disks, $I_{\rm UV}$ and n may be correlated (see Section 2.2.9). But on small scales, enhanced radiation fields will not necessarily be offset by higher gas densities, and $I_{\rm UV}/n$ may span a wide range from "large" to "small."

For $\alpha G/2 \ll 1$ the absorption of the LW radiation is dominated by the combination of H_2-line absorption and H_2-dust absorption, and H I-dust is negligible.[9] For $\alpha G/2 \gg 1$ H I-dust absorption dominates the attenuation of the radiation field. We refer to $\alpha G/2 \ll 1$ as the "weak-field limit" and to $\alpha G/2 \gg 1$ as the "strong-field limit."

We now consider the behavior of $N_{1,\rm tot}$ in these two limits.

It follows from Equations (40) and (39) that for $\alpha G/2 \ll 1$,

$$N_{1,\rm tot} = \frac{1}{\sigma_g}\frac{\alpha G}{2} = \frac{1}{2}\frac{1}{\sigma_g}\frac{D_0}{Rn}G = \frac{1}{2}\frac{\bar{F}_\nu W_{g,\rm tot}}{Rn} = \frac{1}{2}\bar{f}_{\rm diss}\frac{wF_0}{Rn}. \quad (52)$$

So for weak fields, the total H I column density is equal to the ratio of the effective LW dissociation flux to the H_2 formation rate (which is the removal rate of for the H I). The atomic column is proportional to the surface dissociation rate D_0 (or to the field strength $I_{\rm UV}$) and inversely proportional to the cloud gas density n.

In the weak-field limit, the H I-dust opacity associated with the total atomic column $\tau_{1,\rm tot} \equiv \sigma_g N_{1,\rm tot} \ll 1$. We again see that H I-dust plays no role in attenuating the LW radiation field in this limit. For weak fields, the total H I column depends on σ_g only via $W_{g,\rm tot}$, through the possible competition between H_2-line absorption and H_2-dust absorption. For small σ_g where H_2-dust is negligible, dust absorption plays no role whatsoever, and $N_{1,\rm tot}$ is completely independent of σ_g. In the small-σ_g limit, $G \propto \sigma_g$, and the dust absorption cross section cancels out completely. For $R \propto Z'$, we then have $N_{1,\rm tot} \propto 1/Z'$, and the metallicity dependence enters entirely via the H_2 formation rate coefficient. For large σ_g, H_2-dust absorption is non-negligible, and $W_{g,\rm tot} \propto \sigma_g^{-1/2}$ (and $G \propto \sigma_g^{1/2}$), thus $N_{1,\rm tot}$ scales as $\sigma_g^{-1/2}$. Then with $\sigma_g \propto Z'$ and $R \propto Z'$, we have $N_{1,\rm tot} \propto Z'^{-3/2}$.

Expression (52) can be written as the simple "Strömgren relation"[10]

$$RnN_{1,\rm tot} = \frac{1}{2}\bar{F}_\nu W_{g,\rm tot}. \quad (53)$$

The effective dissociation flux on the right-hand side is the rate per unit area at which dissociating photons (those absorbed in H_2-lines but not by H_2-dust) penetrate the cloud surface. By definition these photons are fully absorbed by the H_2 when H I-dust is negligible, so this is also the photodissociation rate per unit surface area. In steady state this must equal the total H_2 formation rate per unit area, which is the left-hand side.

For the strong-field limit $\alpha G/2 \gg 1$, it follows from Equation (40) that

$$N_{1,\rm tot} = \frac{1}{\sigma_g}\ln\left[\frac{\alpha G}{2}\right] = \frac{1}{\sigma_g}\ln\left[\frac{1}{2}\frac{D_0 G}{Rn}\right] = \frac{1}{\sigma_g}\ln\left[\frac{1}{2}\frac{\sigma_g \bar{F}_\nu W_{g,\rm tot}}{Rn}\right] = \frac{1}{\sigma_g}\ln\left[\frac{1}{2}\bar{f}_{\rm diss}\frac{\sigma_g w F_0}{Rn}\right]. \quad (54)$$

For strong fields, $\tau_{1,\rm tot} = \sigma_g N_{1,\rm tot} \gtrsim 1$, and the H I-dust opacity associated with the total atomic column contributes significantly to the attenuation of the incident LW flux. This leads to a saturation and logarithmic dependence of the atomic column on the cloud parameters. For example, increasing the atomic column by increasing the LW-band flux also leads to more effective absorption of the LW photons by the larger H I-dust column. A decreasing fraction of the LW photons is then absorbed by the H_2, and the growth of the atomic column is limited. Similarly, increasing the H_2 formation rate reduces the atomic column, but the H I-dust opacity is then also reduced, which increases the LW fraction available for photodissociation, thereby moderating the reduction of the H I column.

If we neglect the logarithmic factor, then up to a factor of order unity, we have

$$N_{1,\rm tot} \approx 1/\sigma_g \quad (55)$$

for intense fields. Indeed, if the attenuation is dominated by H I-dust, the atomic column must approach a value such that $\tau_{1,\rm tot} \equiv \sigma_g N_{1,\rm tot} \gtrsim 1$. Then, if $\sigma_g \propto Z'$ the H I column $N_{1,\rm tot} \propto 1/Z'$ (neglecting the logarithmic factor). In the strong-field limit, the metallicity dependence enters via the grain absorption cross section.

Finally, Equation (54) for the strong-field limit may also be expressed as the Strömgren relation[11]

$$RnN_{1,\rm tot} = \frac{1}{2}\bar{F}_\nu W_{g,\rm tot}\, u. \quad (56)$$

Here

$$u \equiv \tau_{1,\rm tot}\, e^{-\tau_{1,\rm tot}} \quad (57)$$

is a reduction factor that accounts for H I-dust attenuation of the effective dissociation flux. The right-hand side of Equation (56), including the factor u, is the H_2 photodissociation rate per unit surface area, and this equals the total H_2 formation rate per unit area, which is the left-hand side.

[9] This limit is often referred to in the literature as the "self-shielding" limit. However, this is potentially confusing if self-shielding is properly understood to be associated with just H_2-line absorption. As we have been emphasizing, H_2-dust also absorbs and cannot be ignored for small αG, unless the metallicity is very low. So the weak-field limit may be referred to as the "H_2-line plus H_2-dust" shielding limit.

[10] This is analogous to the Strömgren expression, $\alpha_B n_e N_{\rm H^+} = F_{\rm Lyc}$, for the column density, $N_{\rm H^+}$, of ionized hydrogen in a slab that fully absorbs a flux, $F_{\rm Lyc}$, of Lyman continuum photons. Here n_e is the electron density, and α_B is the electron–proton recombination coefficient.

[11] To see this, note that $e^{-\tau_{1,\rm tot}} = 1/\alpha G$ when $\alpha G \gg 1$.

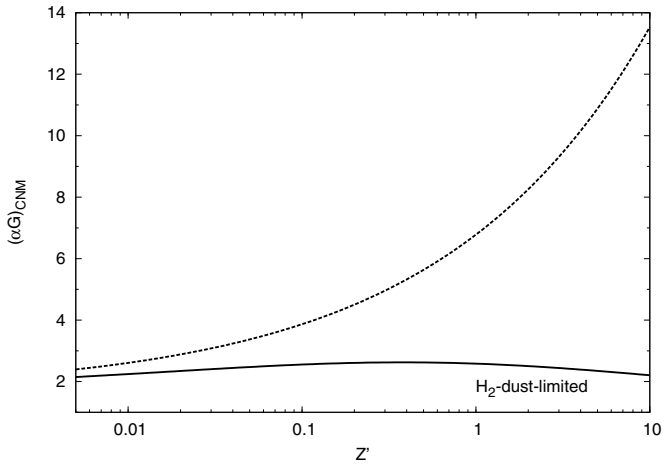

Figure 1. Metallicity dependence of $(\alpha G)_{\rm CNM}$ for two-phase equilibrium as given by Equation (59), with and without (solid and dashed curves) H_2-dust reduction of the effective dissociation bandwidth.

2.2.9. $(\alpha G)_{\rm CNM}$ *for Two-phase Equilibria*

Galaxy disks may be self-regulated such that the thermal pressures in the H I gas enable a cold/warm (CNM/WNM) two-phased mixture, with cold neutral HI (CNM) accumulating in the UV illuminated PDRs of the star-forming molecular clouds (Ostriker et al. 2010; Faucher-Giguère et al. 2013; Kim et al. 2013). As invoked by KMT/MK10, the ratio $I_{\rm UV}/n$ may then be restricted to a narrow range. This then gives rise to a characteristic αG for self-regulated disks, as follows.

For a given heating rate, two-phased equilibrium occurs for a narrow range of thermal pressures and associated CNM and WNM densities, $n_{\rm CNM}$ and $n_{\rm WNM}$, as controlled by the combined action of Lyα and C II fine-structure emission line cooling, with a metallicity dependence via the abundance of the gas-phase carbon ions (Field et al. 1969; Wolfire et al. 2003). Given the FUV heating rates and the metallicity-dependent emission line cooling rates, the characteristic CNM density for two-phase equilibrium will be close to the minimum gas density for which CNM is possible. Wolfire et al. (2003) developed the analytic formula

$$n_{\rm CNM} = \frac{31\phi_{\rm CNM}}{1+3.1Z'^{0.365}} I_{\rm UV}\ {\rm cm}^{-3}, \tag{58}$$

for the characteristic CNM density, assuming that FUV grain photoelectric emission is the dominant heating mechanism for the gas. In this expression, $I_{\rm UV}$ is again the FUV intensity (normalized to the Draine field), Z' is the metallicity, and $\phi_{\rm CNM}$ is a factor of order unity. Following KMT/MK10 we set $\phi_{\rm CNM} = 3$. This gives $n_{\rm CNM} = 23\ {\rm cm}^{-3}$ for $I_{\rm UV} = 1$, at $Z' = 1$.

Most importantly, $n_{\rm CNM}$ is proportional to $I_{\rm UV}$. If the gas density n in the FUV illuminated gas is set equal to $n_{\rm CNM}$, the ratio $I_{\rm UV}/n$ then depends on the metallicity only, as given by Equation (58). With Equation (51) we then have

$$(\alpha G)_{\rm CNM} = 6.78\left(\frac{1+3.1Z'^{0.365}}{4.1}\right)\frac{\phi_g}{1+(2.64\phi_g Z')^{1/2}} \tag{59}$$

for self-regulated systems. In Figure 1 the solid curve is $(\alpha G)_{\rm CNM}$ versus Z' as given by Equation (59) (assuming $\phi_g = 1$). The dashed curve excludes the $(2.64\phi_g Z')^{1/2}$ term that accounts for H_2-dust reduction of the effective dissociation bandwidth (not considered by KMT/MK10 as discussed in Section 4). Remarkably, the enhanced $n_{\rm CNM}$ associated with reduced cooling efficiency at low metallicity (Equation (58) is offset by the increased dissociation bandwidth at low Z'. Thus, so long as grain photoelectric heating dominates, we have

$$\frac{(\alpha G)_{\rm CNM}}{2} \approx 1 \tag{60}$$

for self-regulated systems, independent of Z'. The expected H I columns are then midway between the weak- and strong-field limits.

2.3. Isotropic Fields

We now consider clouds illuminated by isotropic radiation fields.

Let I_ν be the specific LW photon intensity of an isotropic field, and let $\mu \equiv \cos\theta$, where θ is the angle of an incident ray relative to the cloud normal. Again, we are assuming plane-parallel clouds. In the absence of dust, the photodissociation rate at a molecular column N_2 normal to the cloud surface may be written as

$$\begin{aligned} D(N_2) &= \frac{D_0}{2}\int_0^1 f_{\rm shield}(N_2/\mu)\,d\mu \\ &= 2\pi\bar{I}_\nu\int_0^1 \frac{dW_d(N_2/\mu)}{dN_2}\,\mu\,d\mu, \end{aligned} \tag{61}$$

where $f_{\rm shield}(N_2)$ is the unidirectional self-shielding function defined by Equation (16), and $W_d(N_2)$ is the *same* effective "multi-line" curve of growth for the (dust-free) dissociating bandwidth that appears in Equation (11) for beamed fields. In Equation (61), the contribution to the angular-integrated dissociation rate is reduced by the self-shielding factor $f_{\rm shield}(N_2/\mu)$ along each ray. Here $\bar{I}_\nu \equiv \bar{F}_\nu/4\pi$ is the free-space specific intensity averaged over the dissociating transitions, as given by Equation (12).

With the inclusion of dust absorption along each ray, the H I/H_2 formation–destruction equation at a molecular column N_2 is

$$Rn\,dN_1 = 2\pi\bar{I}_\nu\int_0^1 \frac{dW_d(N_2/\mu)}{dN_2}\,e^{-2\sigma_g N_2/\mu}\,e^{-\sigma_g N_1/\mu}\,\mu\,d\mu\,dN_2. \tag{62}$$

Like Equation (24) for beamed fields, this is a differential equation for $N_1(N_2)$. However, because of the angular integration, the exponential term $\exp(-\sigma_g N_1/\mu)$ for the H I-dust attenuation along a ray cannot be moved to the left-hand side as was done in Equation (24). To enable a separation of variables nevertheless, we replace the variable μ with some constant average $\langle\mu\rangle$ in the H I-dust term, and we *then* move this term to the left-hand side. For H_2-dust attenuation on the right-hand side, we keep μ as a variable in the exponential term.

Making this approximation and integrating over the atomic and molecular columns gives

$$Rn\int_0^{N_{1,\rm tot}} e^{\sigma_g N_1'/\langle\mu\rangle}\,dN_1' = 2\pi\bar{I}_\nu\,W_{g,\rm tot}\int_0^1 \mu d\mu = \frac{1}{4}\bar{F}_\nu\,W_{g,\rm tot}, \tag{63}$$

where

$$W_{g,\rm tot} \equiv \int_0^\infty \mu\frac{dW_d(N_2/\mu)}{dN_2}\,e^{-2\sigma_g N_2/\mu}\,d\left(\frac{N_2}{\mu}\right). \tag{64}$$

For $W_{g,\rm tot}$ as defined by Equation (64), the integration variable is N_2/μ, and the integration is from 0 to ∞. Thus, the $W_{g,\rm tot}$

that appears here is the *same* effective total H_2-dust-limited dissociation bandwidth that we defined for beamed radiation in Equation (27) (and represented analytically by Equation (28)). The effective bandwidths are *identical* for isotropic and beamed fields because the relative fractions of LW photons absorbed by H_2-lines versus H_2-dust along a ray do not depend on the ray's orientation. The product $\bar{F}_\nu W_{g,\rm tot}/4$ is then the effective dissociating flux for the isotropic field.

It follows from Equation (63) that the total H I column is given by

$$N_{1,\rm tot} = \frac{\langle\mu\rangle}{\sigma_g}\ln\left[\frac{1}{4}\frac{\sigma_g}{\langle\mu\rangle}\frac{\bar{F}_\nu W_{g,\rm tot}}{Rn} + 1\right] = \frac{\langle\mu\rangle}{\sigma_g}\ln\left[\frac{1}{4}\frac{\sigma_g}{\langle\mu\rangle}\bar{f}_{\rm diss}\frac{wF_0}{Rn} + 1\right] \quad (65)$$

or

$$N_{1,\rm tot} = \frac{\langle\mu\rangle}{\sigma_g}\ln\left[\frac{1}{\langle\mu\rangle}\frac{\alpha G}{4} + 1\right], \quad (66)$$

where again $\alpha \equiv D_0/Rn$, and $G \equiv \sigma_g W_{g,\rm tot}/\sigma_d^{\rm tot}$. The total H I-dust optical depth in the normal direction is then

$$\tau_{1,\rm tot} = \langle\mu\rangle\ln\left[\frac{1}{\langle\mu\rangle}\frac{\alpha G}{4} + 1\right]. \quad (67)$$

Equations (65), (66), and (67) for isotropic fields are very similar to Equations (39), (40), and (43) for beamed fields. The values of α are *equal* for corresponding beamed and isotropic fields (i.e., fields with the same $I_{\rm UV}$). Furthermore, G is independent of the field geometry. A geometrical factor of $1/4$ appears for slabs irradiated by isotropic fields (as opposed to $1/2$ for beamed fields).

The average angle $\langle\mu\rangle$ appears in Equations (65), (66), and (67) because the radiation fraction absorbed by H I-dust *does* depend on the field geometry and is larger for isotropic fields for which the relative H I-dust attenuation is increased along inclined rays. In Section 3.1.5 we calculate $\langle\mu\rangle$ by fitting these analytic expressions to the results of our numerical computations for the atomic columns for isotropic fields. We find that universally and to an excellent approximation $\langle\mu\rangle = 0.8$, independent of αG or Z', i.e., independent of the cloud parameters n, R, D_0, or σ_g.

We again consider the weak- and strong-field limits.

For weak fields ($\alpha G/4 \ll 1$),

$$N_{1,\rm tot} = \frac{1}{\sigma_g}\frac{\alpha G}{4} = \frac{1}{\sigma_g}\frac{1}{4}\frac{D_0}{Rn}G = \frac{1}{4}\frac{\bar{F}_\nu W_{g,\rm tot}}{Rn} = \frac{1}{4}\bar{f}_{\rm diss}\frac{wF_0}{Rn}, \quad (68)$$

and the H I-dust opacity $\sim\sigma_g N_{1,\rm tot}/\langle\mu\rangle$ is negligible and plays no role in attenuating the LW flux. The total atomic column depends on σ_g only via the dissociation bandwidth $W_{g,\rm tot}$, i.e., via the competition between H_2-line absorption and H_2-dust absorption. As for beamed radiation, Equation (68) is a simple Strömgren relation, and $N_{1,\rm tot}$ is equal to the ratio of the effective dissociation flux (or dissociation rate per unit surface area) to the H_2 formation rate. In the weak-field limit, and for a given αG and σ_g, i.e., for a given D_0 (or F_0 or $I_{\rm UV}$), n, R, and σ_g (or Z'), the atomic column for isotropic radiation is equal to half that produced by a corresponding beamed field. This is simply due to the factor-of-two difference in the LW photon fluxes for corresponding isotropic versus beamed fields for a given field strength $I_{\rm UV}$.

In the strong-field limit, $\alpha G/4 \gg 1$,

$$N_{1,\rm tot} = \frac{\langle\mu\rangle}{\sigma_g}\ln\left[\frac{\alpha G}{4}\right] = \frac{\langle\mu\rangle}{\sigma_g}\ln\left[\frac{1}{4}\frac{D_0 G}{Rn}\right] = \frac{\langle\mu\rangle}{\sigma_g}\ln\left[\frac{1}{4}\frac{\sigma_g}{\langle\mu\rangle}\frac{\bar{F}_\nu W_{g,\rm tot}(\sigma_g)}{Rn}\right]. \quad (69)$$

For strong fields, $\sigma_g N_{1,\rm tot} \gtrsim 1$ and the H I-dust opacity is significant and dominates the attenuation of the radiation. As for beamed fields, the total atomic column saturates, and $N_{1,\rm tot}$ is insensitive to the cloud parameters except for σ_g. Up to the logarithmic factor of order unity, we then have

$$N_{1,\rm tot} \approx \frac{\langle\mu\rangle}{\sigma_g}. \quad (70)$$

Because $\langle\mu\rangle = 0.8$, the saturation columns are only slightly smaller for isotropic versus beamed fields for large αG, and they are not very different.

3. NUMERICAL MODEL COMPUTATIONS

With our analytic results (Section 2) in mind, we now present detailed numerical calculations for the H I-to-H_2 transition profiles and the associated buildup of the atomic hydrogen columns for planar clouds illuminated by either beamed or isotropic FUV LW-band radiation fields. For this purpose we use the *Meudon PDR code*[12] (Le Petit et al. 2006) for the computation of the UV radiative transfer and depth-dependent photodissociation rates and for the steady state atomic and molecular hydrogen gas densities. The code implements the "extended spherical harmonics" method (Flannery et al. 1980; Goicoechea & Le Bourlot 2007) for an exact numerical solution of the coupled H_2-line and dust scattering and absorption radiative transfer. An adaptive frequency grid is employed with sufficient resolution ($\Delta\nu/\nu \sim 10^{-5}$) to capture the contributions of the narrow H_2-line Doppler cores and broad wings to the total ultraviolet opacities. The competition between dust absorption and scattering and H_2-line absorptions, and the important effects of H_2-line overlap, are included in the calculation of the local radiation field intensities and H_2 photodissociation rates.

A principal feature of the *Meudon PDR code* is that the radiative transfer can be calculated for either beamed or isotropic fields. We assume the Draine spectrum (Equation (2)), and we calculate models for beamed and isotropic configurations. As defined in Section 2.2, for corresponding beamed and isotropic fields the radiation energy densities at the cloud surfaces are identical (Section 2.1). We compare our numerical results with the analytic formulae discussed above.

One of our main goals is the accurate computation of the effective H_2-dust-limited dissociation bandwidth $W_{g,\rm tot}(\sigma_g)$ (Equation (27)) summed over all of the LW-band absorption lines, for a wide range of FUV dust absorption cross sections σ_g (as set by the metallicity Z'). We also calculate H I-to-H_2 transition profiles and the resulting atomic hydrogen columns from the weak- to strong-field limits (small to large αG), for both beamed and isotropic fields and for a wide range of metallicities.

For computational efficiency in our large parameter space and for direct comparisons with our analytic formulae, we have made several simplifying assumptions and modifications to the standard *Meudon PDR code*. First, instead of considering a full

[12] Publically available at http://pdr.obspm.fr.

range of grain sizes and wavelength-dependent absorption and scattering properties, we assume a single representative σ_g for each metallicity (as given by Equation (20)), independent of photon frequency within the narrow LW band. We assume pure forward scattering by the grains and neglect the (small) effects of back-scattering discussed by Goicoechea & Le Bourlot (2007). Thus, our σ_g enters as a simple effective absorption cross section. We have verified by spot checks within our parameter space that our assumption of a constant σ_g alters the results for the computed H I columns by no more than 10% for any metallicity compared with computations incorporating a standard grain-size distribution.

Second, we decouple the H I/H_2 formation–destruction equation from the complex gas and grain networks that govern the heavy element chemistry. We assume that the H_2 is formed on grain surfaces only with a rate coefficient R as given by Equation (21) and is destroyed only by (depth-dependent) LW photodissociation. We exclude gas-phase formation, e.g., via the sequence $H + e \rightarrow H^- + \nu$, $H^- + H \rightarrow H_2 + e$,[13] or destruction by cosmic-ray or X-ray secondary ionization (and we set the ionization rate ζ equal to zero). Thus, at depths where the LW radiation field is fully absorbed, the atomic density vanishes, and the entire H I column is maintained by photodissociation.

Third, we consider isothermal clouds rather than solving a heating–cooling equation for the gas temperature T. Our standard is $T = 100$ K, for which the H_2 formation rate coefficient $R = 3 \times 10^{-17}$ cm^3 s^{-1} for $Z' = 1$. And fourth, we assume that the total hydrogen nucleon density, $n = n_1 + 2n_2$, is a constant independent of cloud depth, so that the local H_2 formation rate Rn (s^{-1}) is also constant for any given model.

Fifth, we ignore absorption by neutral atomic carbon (C I) in the H_2 photodissociation layers. The carbon (continuum) photoionization band 1100–912 Å coincides almost exactly with the LW band for H_2 photodissociation, and C I, H_2, and dust compete for the same photons. The carbon photoionization cross section is 1.6×10^{-17} cm^{-2} (van Dishoeck et al. 2006), so that the C I opacity $\tau_{\rm CI} = 1.6 \times 10^{-17} AZ' N x_{\rm CI} \approx 1.6 \times 10^{-21} Z' N x_{\rm CI}$, where N is the hydrogen gas column, $A \approx 10^{-4}$ is the gas-phase carbon abundance for solar ($Z' = 1$) metallicity, and $x_{\rm CI}$ is the fraction of carbon present in atomic form. For $x_{\rm CI} \approx 1$, $\tau_{\rm CI}$ is competitive with the dust opacity $\tau_g = \sigma_g N \approx 1.9 \times 10^{-21} N$. However, the carbon is primarily C^+ and $x_{\rm CI}$ is generally very small in the dust-limited or H_2-line-limited absorption layers in which the H I columns are built up, as follows. In the absence of dust or H_2 absorption, and assuming that C I absorbs the entire LW flux in maintaining an outer and optically thick C^+ zone, then $F_0 \simeq \alpha n_{\rm C^+}^2 \ell = \alpha (AZ')^2 nN$, where $F_0 = 2 \times 10^7 I_{\rm UV}$ is the ionizing photon flux (Equation (3)), $\alpha \approx 2 \times 10^{-11}$ cm^3 s^{-1} is the electron–carbon recombination rate coefficient (Wolfire et al. 2008), $n_{C^+} = AZ'n$ is the volume density of C^+ ions, ℓ is the length scale of the optically thick C^+ Strömgren layer, and N is the *hydrogen* gas column associated with the C^+ layer. We are assuming that the carbon ions are neutralized by recombination with free electrons and that $n_e \approx n_{C^+}$. However, if the dust opacity associated with this gas column is large, i.e., if $\sigma_g N \gtrsim 1$, then the C^+ layer is limited by dust and C I absorption may be ignored. The condition $\sigma_g N \gtrsim 1$ may be expressed as $\sigma_g F_0/[(AZ')^2 \alpha n] \gtrsim 1$, or $I_{\rm UV}/n \gtrsim 5 \times 10^{-6} Z'$ cm^3, or $\alpha G \gtrsim 10^{-3} Z'$. Thus, unless αG is unusually small, C I absorption is negligible. Using our PDR code, and turning on the effects of additional C^+ neutralization processes such as dust-assisted recombination and chemical removal processes, we find that even for $Z' = 1$ the C I absorption is less than a 10% effect for $\alpha G = 0.01$ and is negligible for larger αG.

Sixth, we ignore H I Lyman-series line absorption of the LW-band photons. These atomic lines (beginning with Lyβ at 1026 Å) do appear within the molecular LW absorption band (e.g., Draine & Bertoldi 1996), and the *Meudon PDR code* includes them. However, very large atomic columns are required for the atomic line equivalent widths to contribute significantly to the absorption. We find that an H I column of $\sim 10^{24}$ cm^{-2} is required for the summed equivalent widths of the Ly-series lines to equal half the LW bandwidth (most of this absorption is due to just Lyβ). Such large H I columns are produced only for very small values of σ_g and Z', even in the strong-field large αG limit. For example, for $\alpha G \sim 100$ it follows from Equation (40) that $N_{1,\rm tot} \gtrsim 10^{24}$ cm^{-2} requires $\sigma_g \lesssim 3.9 \times 10^{-24}$ cm^2, or $Z' \lesssim 2 \times 10^{-3}$. Thus, for the relevant range of metallicities, the atomic line absorptions can be ignored, and we exclude them in the radiative transfer.

With the above assumptions, the basic inputs to the code are the intensity, $I_{\rm UV}$, and spectral shape of the radiation field (we assume the Draine representation, Equation (2)), in either a beamed or isotropic configuration, the total gas density n, the associated H_2 formation rate Rn (temperature and metallicity dependent), and the dust grain absorption cross section σ_g (metallicity dependent). The dimensionless parameter αG is formed from these cloud variables as described in Sections 2.2.5 and 2.2.6.

For any set of parameters the critical numerical computation is for the depth-dependent line-plus-continuum absorptions and the attenuation of the H_2 photodissociation rate. For the H_2, our code includes all 302 ro-vibrational vj levels in the $X^1\Sigma_g^+$ ground electronic state and the entire matrix of Lyman and Werner transitions to discrete $v'j'$ levels in the excited $B^1\Sigma_u$ and $C^1\Pi_u$ states. We exclude transitions with energies greater than the hydrogen ionization energy of 13.59 eV. (As is standard, we assume that any ionizing photons are always absorbed in adjacent H II regions outside of the PDRs.) Our code includes transitions out of excited v levels of the X state. However, for almost all conditions of interest and throughout most of the H I-to-H_2 transition zones, the dominating line absorptions are from the lowest few rotational levels ($j = 0$ to 5) levels of the $v = 0$ level.[14] Thus, the relevant UV transitions lie between 1108 and 912 Å, and this is the wavelength range of our "standard LW band."

The fractional populations, x_{vj}, of the vj levels in the X state are computed assuming population and depopulation by the upward and downward X–B and X–C transitions, quadrupole radiative (cascade) transitions between the X-state vj levels, and excitations and deexcitations in collisions with He, H^+, H, and other H_2 molecules. We use the Abgrall et al. (1993a) and Abgrall et al. (1993b) LW-band oscillator strengths and transition wave-numbers and the Abgrall et al. (2000) probabilities

[13] With our assumption that the grain surface H_2 formation rate coefficient R is linearly proportional to the metallicity, the gas-phase formation routes become important for $Z' \lesssim 5 \times 10^{-3}$, depending on the temperature and fractional ionization, x_e, of the gas. For an estimate of the effective rate coefficient, R_-, for H_2 formation via the negative-ion H^- intermediary, see, e.g., Equation (A7) of MK10, $R_- = 8 \times 10^{-19} x_{e,-3} T_3^{0.88}$ cm^3 s^{-1}.

[14] Photodissociation out of excited vibrational levels becomes significant when $I_{\rm UV} \gtrsim 10^5$ and the UV excitation rates become comparable to the quadrupole vibrational decay rates (Shull 1978). However, even for such intense fields, the excitation rates become small as the lines rapidly become optically thick, and for most of the H I layer absorption out of excited vibrational states is negligible (S88).

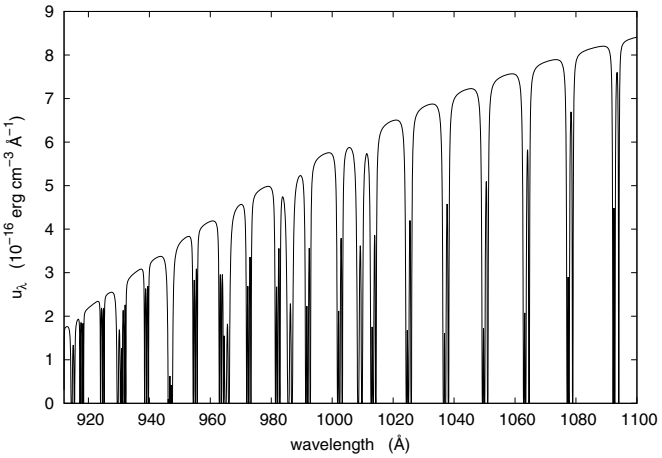

Figure 2. Absorbed far-UV spectrum showing partially overlapping Lyman–Werner band absorption lines, for beamed radiation into a cloud, at a total hydrogen gas column density of 3.74×10^{20} cm^{-2}, for a free-space radiation intensity $I_{\rm UV} = 35.5$, gas density $n = 10^3$ cm^{-3}, and metallicity $Z' = 1$ ($\alpha G/2 = 1$).

for spontaneous radiative dissociations from the individual ro-vibrational levels in the excited B and C states. For the radiative quadrupole transitions, we use the Einstein-A values computed by Wolniewicz et al. (1998). For the collisional processes we use the ro-vibrational state-to-state rate coefficients reported in Le Bourlot et al. (1999) and Wrathmall et al. (2007) in their study of H_2 excitation in astrophysical media.

As an example of our radiative transfer computations, we show in Figure 2 the energy density (erg cm^{-3} Å^{-1}) at a cloud column depth of $N = 3.74 \times 10^{20}$ cm^{-2}, or $\tau_g = 0.7$ ($A_V = 0.2$), for $\sigma_g = 1.9 \times 10^{-21}$ cm^2 ($Z' = 1$) for a model computation with $I_{\rm UV} = 35.5$ (isotropic) and $n = 1000$ cm^{-3}, or $\alpha G/2 = 1$. At this depth the cores of the individual absorption line are very optically thick, but the continuum between the lines has not yet been significantly attenuated by overlapping line wings. Around 80 strong lines are visible in Figure 2, consistent with our analytic estimate $\sigma_d^{\rm tot}/\sigma_d \simeq 80$ for the number of lines involved in the photodissociation process, as discussed in Section 2.2.1.

3.1. Results

We now present our numerical code results for (1) the unattenuated free-space H_2 photodissociation rate; (2) the curves of growth for the H_2-dust-limited dissociation bandwidth $W_g(N_2)$; (3) the total dissociation bandwidth $W_{g,\rm tot}(\sigma_g)$; (4) the self-shielding function $f_{\rm shield}(N_2)$; and (5) the mean self-shielding factor $G(Z')$. We then present H I-to-H_2 transition profiles and total integrated H I columns for beamed and isotropic fields and for a range of αG and metallicities Z'.

3.1.1. Free-space H_2 Photodissociation Rate

The optically thin (full 4π) free-space (optically thin) H_2 photodissociation rate, D_0, is a fundamental parameter for ISM and galaxy evolution studies, and we have recalculated it here for the Draine FUV spectrum (Equation (2)). In Table 1, and for $I_{\rm UV} = 1$, we list the free-space UV excitation rates, P_{vj} (s^{-1}) out of the 14 lowest-lying H_2 (v, j) ro-vibrational levels. Each rate is summed over all upward LW transitions. We also list the mean dissociation probabilities $\langle f_{\rm diss}\rangle_{vj}$, averaged over all of the transitions, and the resulting dissociation rates, D_{vj} (s^{-1}) out of each (v, j) level. Our numbers are consistent with Draine & Bertoldi (1996) (see their Table 2), who used our basic input molecular data sets.

Table 1
The H_2 Excitation Rates, P_{vj}, Mean Dissociation Fractions, $\langle f_{\rm diss}\rangle_{vj}$, and Dissociation Rates, D_{vj}; for the Free-space (Optically Thin) Draine Radiation Field, Out of the Lowest 14 Ro-vibrational H_2 (v, j) Levels in Order of Energy, E_i (in cm^{-1}), Relative to the Ground (0,0) Level

(v, j)	E_i (cm^{-1})	P_{vj} (s^{-1})	$\langle f_{\rm diss}\rangle_{vj}$	D_{vj} (s^{-1})
(0,0)	0.000	4.71(−10)	0.117	5.51(−11)
(0,1)	118.505	4.75(−10)	0.119	5.65(−11)
(0,2)	354.363	4.83(−10)	0.123	5.94(−11)
(0,3)	705.567	4.95(−10)	0.130	6.44(−11)
(0,4)	1168.825	5.11(−10)	0.145	7.41(−11)
(0,5)	1740.277	5.30(−10)	0.141	7.47(−11)
(0,6)	2414.852	5.57(−10)	0.160	8.91(−11)
(0,7)	3187.691	5.86(−10)	0.160	9.38(−11)
(0,8)	4051.884	6.19(−10)	0.175	1.08(−10)
(1,0)	4161.259	7.14(−10)	0.051	3.64(−11)
(1,1)	4273.913	7.21(−10)	0.055	3.97(−11)
(1,2)	4497.992	7.31(−10)	0.057	4.17(−11)
(1,3)	4831.595	7.43(−10)	0.057	4.24(−11)
(0,9)	5002.162	6.58(−10)	0.197	1.30(−10)

The *total* dissociation rate is weighted by the population fractions x_{vj} but is insensitive to the gas temperature or density when the excitation is mainly out of the lowest few j levels. For T between 10 to 10^3 K, and for n ranging from 10 to 10^6 cm^{-3}, we find that to within at most a 2% variation, $D_0 = 5.8 \times 10^{-11}$ s^{-1} for $I_{\rm UV} = 1$. The dissociation rate is essentially proportional to the field intensity. For very intense fields, the rate is increased by enhanced excitation of the rotational states and photodissociation out of these states by photons longward of 1108 Å, outside our nominal LW band. For $T = 100$ K, and $n = 100$ cm^{-3}, we find that for $I_{\rm UV}$ from 1 to 10^3, $D_0 = 5.8 \times 10^{-11}\phi_{\rm ex} I_{\rm UV}$ s^{-1}, where the "rotational excitation factor" $\phi_{\rm ex}$ increases from 1 to 1.5 for this range of field intensities. We have also computed the mean flux density in the free-space radiation field, as defined by Equation (12). For the Draine spectrum, we find that $\bar{F}_\nu = 2.46 \times 10^{-8}\phi_{\rm ex} I_{\rm UV}$ photons cm^{-2} s^{-1} Hz^{-1} for the same range of T, n, and $I_{\rm UV}$. For the analysis we present in Section 2, we assume $\phi_{\rm ex} = 1$.

3.1.2. $W_g(N_2)$ and $W_{g,\rm tot}(\sigma_g)$

As discussed in Section 2.2.4, the "H_2-dust-limited dissociation bandwidth" $W_g(N_2)$ (Equation (26)) is a fundamental quantity for the H I-to-H_2 transitions and the buildup of the H I column densities.

In Figure 3 we plot our curve-of-growth computations for $W_g(N_2)$ integrated over all of the LW-band absorption lines, for σ_g ranging from 1.9×10^{-20} to 1.9×10^{-23} cm^2, corresponding to metallicities Z' from 0.01 to 10. We set the Doppler-b parameters for all of the lines equal to a typical ISM cloud value of 2 km s^{-1}. Our results are insensitive to the precise choice for b because the dominant absorption lines are very highly damped. We extract the $W_g(N_2)$ curves from our numerical radiative transfer computations for the radiation flux absorbed in the lines, self-consistently accounting for the flux reduction due to the presence of H_2-dust. For any σ_g, the curve of growth $W_g(N_2)$ depends primarily on the internal molecular oscillator strengths, line profile cross sections, and dissociation probabilities for the excited states. We have verified by explicit computations that $W_g(N_2)$ is indeed very insensitive to external

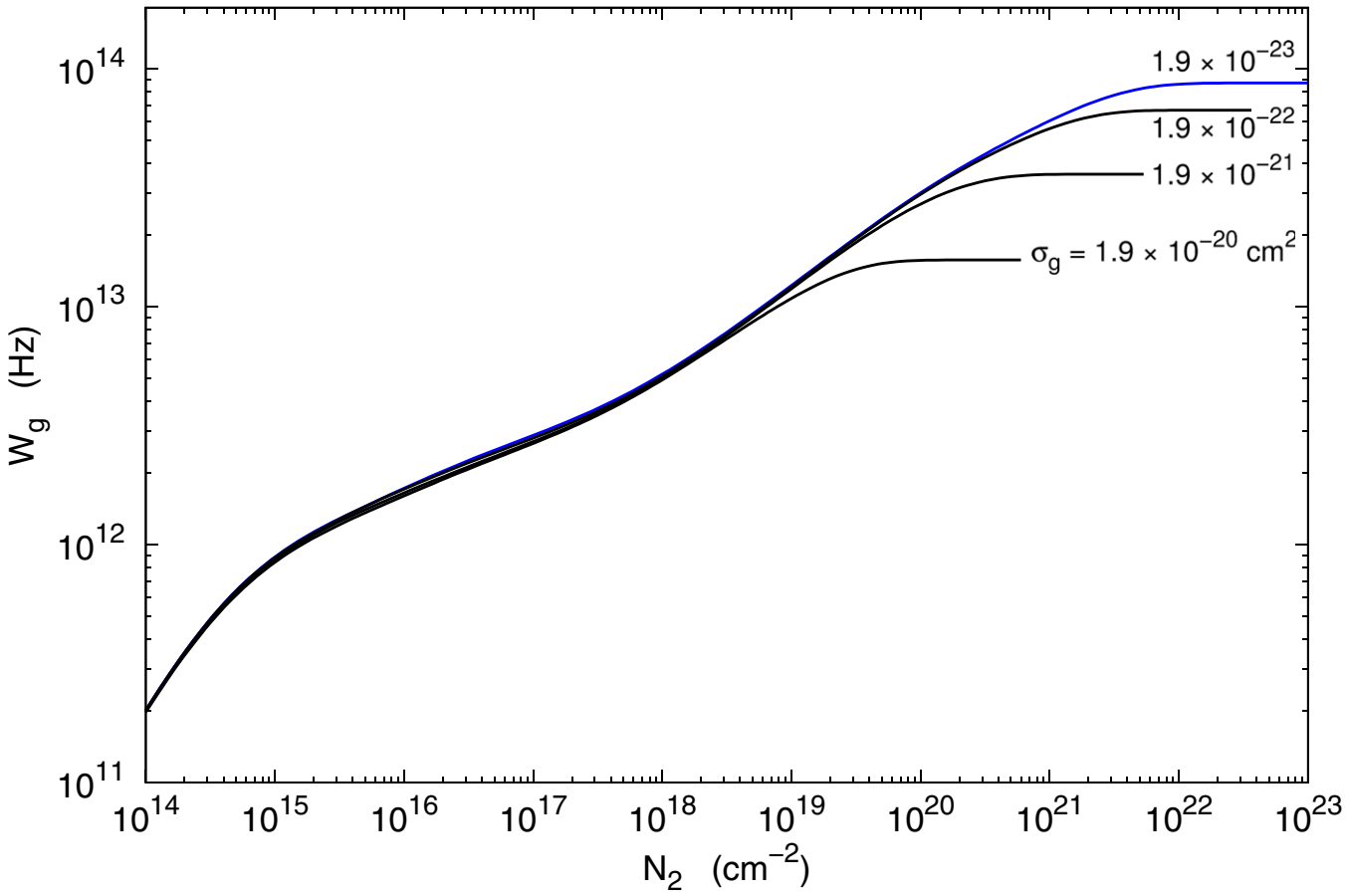

Figure 3. Curves of growth, $W_g(N_2)$, for the dust-limited dissociation bandwidth. The far-UV dust absorption cross sections σ_g range from 1.9×10^{-20} to 1.9×10^{-23} cm^{-2}. For $\sigma_g = 1.9 \times 10^{-23}$ cm^{-2} (blue curve), the H_2-lines fully overlap, and $W_g(N_2) = W_d(N_2)$ (see text).
(A color version of this figure is available in the online journal.)

cloud parameters such as the field intensity I_{UV} and/or gas density n, or temperature T. The curves of growth are also insensitive to the rotational-level distributions and ortho-to-para H_2 ratio. The specific curves displayed in Figure 3 were extracted from model runs with $I_{UV} = 4$, $n = 10^5$ cm^{-3}, and $T = 100$ K, and for a constant ortho-to-para ratio set equal to 3 (with H^+–H_2 proton exchange reactions turned off).

For $N_2 \lesssim 10^{14}$ cm^{-2}, all of the lines are optically thin, and W_g increases linearly with N_2. Between 10^{15} and 10^{17} cm^{-2}, the growth is logarithmic as the Doppler cores become optically thick. At larger columns, W_g increases more rapidly again as absorptions start occurring out of the line wings. For N_2 between 10^{18} and 10^{20} cm^{-2}, we find that W_g grows as $N_2^{3/8}$, a bit more slowly than for a single damped line (for which it would be $N_2^{1/2}$).

The W_g saturates at sufficiently large H_2 columns. When H_2-dust is negligible, the entire LW band is absorbed in fully overlapping lines, and W_g reaches a maximal value of 9×10^{13} Hz, for $N_2 \gtrsim 10^{22}$ cm^{-2}. In Figure 3 the absorption is essentially dust-free for $\sigma_g = 1.9 \times 10^{-23}$ cm^2, since the lines overlap before the H_2-dust opacity becomes significant, and for the (blue) curve $W_g(N_2) = W_d(N_2)$ (see Sections 2.2.1 and 2.2.4). For larger σ_g, and for $N_2 \gtrsim 1/(2\sigma_g)$, the asymptotic W_g is limited by H_2-dust opacity.

Figure 4 shows our results for the "total dust-limited bandwidth" $W_{g,tot}(\sigma_g)$ (Equation (27)) for σ_g from 10^{-24} to 10^{-20} cm^2. The points are our numerical results, and the solid curve is our analytic representation

$$W_{g,tot}(\sigma_g) \simeq \frac{9.9 \times 10^{13}}{1 + (\sigma_g / 7.2 \times 10^{-22}\ \mathrm{cm}^2)^{1/2}}\ \mathrm{Hz}, \qquad (71)$$

as already introduced in Section 2. This expression is accurate to within 4% compared with the numerical results. The transition from the line overlap to H_2-dust-limited regimes (small to large σ_g) occurs at $\sigma_g \sim 7.2 \times 10^{-22}$ cm^2. Line overlap is just starting to become important for solar ($Z' \sim 1$) metallicities. For a fully molecular slab, most of the LW-band radiation is absorbed by H_2-dust for $Z' \gtrsim 0.5$. For $Z' \lesssim 0.5$, most of the radiation is absorbed in H_2-lines. Our results show that the regimes of small and large σ_g are both relevant for the realistic range of metallicities in galaxies.

To a good approximation $W_{g,tot} \propto \sigma_g^{-1/2}$ for large σ_g as indicated by our numerical results and Equation (28). This is the expected scaling for a *single* (effective) damped absorption line in competition with H_2-dust (see Section 2.2.4). We adopt $W_{g,tot} \propto \sigma_g^{-1/2}$ for large σ_g for our analytic scaling relations in Section 2, although $W_g(N_2)$ grows somewhat more slowly with N_2 than for a single line.

3.1.3. Self-shielding Function and G(Z′)

By definition, the H_2 "self-shielding function" $f_{shield}(N_2) \equiv (1/\sigma_d^{tot}) dW_d/dN_2$, where $W_d(N_2)$ is the dissociation bandwidth for vanishing σ_g (see Equation (16)).

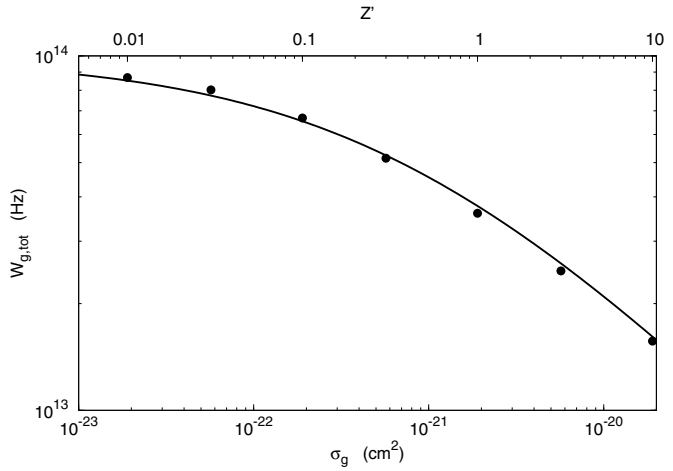

Figure 4. Total dust-limited dissociation bandwidth $W_{g,\rm tot}(\sigma_g)$. The points are the results of our radiative transfer computations. The solid curve is our fitting formula Equation (28).

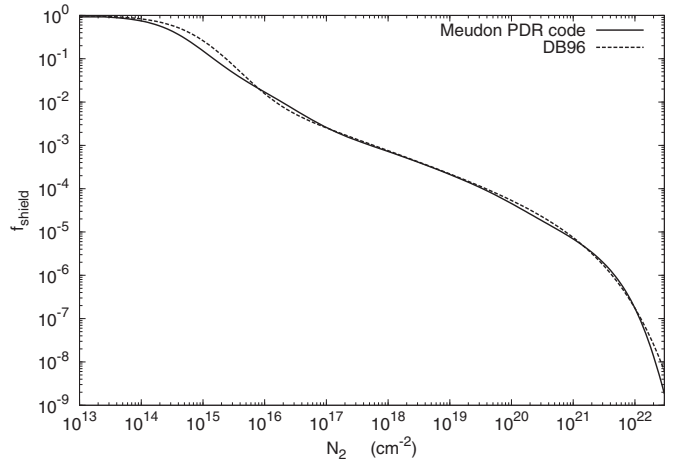

Figure 5. Our computed H_2 self-shielding function (solid curve) and the Draine & Bertoldi (1996) fitting formula (dashed curve) as given by Equation (72) for a Doppler parameter $b = 2$ km s^{-1}.

In Figure 5 we plot (solid curve) our numerically computed derivative $f_{\rm shield}(N_2)$. We also plot (dashed) the Draine & Bertoldi (1996) fit (their Equation (37)) for the shielding function, given by

$$f_{\rm shield}(N_2) = \frac{0.965}{(1+x/b_5)^2} + \frac{0.035}{(1+x)^{0.5}} \times \exp[-8.5\times10^{-4}(1+x)^{0.5}], \quad (72)$$

where $x = N_2/5\times10^{14}{\rm cm}^{-2}$ and $b_5 = b/10^5$ cm s^{-1} (we assume $b_5 = 2$). It is evident that our computed shielding function is in excellent agreement with this formula.

At low N_2, the lines are optically thin and $f_{\rm shield} = 1$. As the line cores become optically thick for $N_2 \gtrsim 10^{14}$ cm^{-2}, the molecules "self-shield" and $f_{\rm shield}$ decreases. By 10^{18} cm^{-2}, $f_{\rm shield} = 5\times10^{-4}$. Between 10^{18} and 10^{20} cm^{-2}, the shielding function declines as $N_2^{-5/8}$, as expected given the (integral) behavior of $W_d(N_2)$ in this range. Finally, at larger columns $f_{\rm shield}$ drops sharply as the lines fully overlap. As found by Draine & Bertoldi (1996), the reduction due to line overlap sets in at a column of 3×10^{20} cm^{-2}. We again see that attenuation due to line overlap becomes important for $Z' \lesssim 1$. For such metallicities, H_2-dust opacity becomes significant only

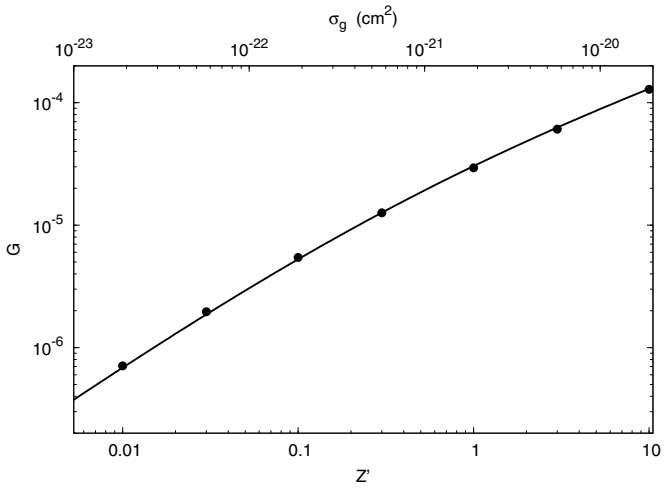

Figure 6. Average self-shielding factor G as a function of metallicity Z' or dust absorption cross section σ_g. The points are our numerical results, and the curve is our analytic expression Equation (46).

at columns $1/(2\sigma_g) \gtrsim 3\times10^{20}$ cm^{-2}, at which point the lines have already overlapped and the LW photons fully absorbed.

In Figure 6 we plot the "average self-shielding factor," $G \equiv (\sigma_g/\sigma_d^{\rm tot})W_{g,\rm tot}(\sigma_g)$ (Equation (41) or Equation (45)), as a function of the metallicity, assuming $\sigma_g = 1.9\times10^{-21}Z'$ cm^{-2} ($\phi_g = 1$). The points are our numerical results, and the curve is our analytic fitting formula Equation (46). As expected, for low metallicity (full overlap) $G \propto Z'$, but for high metallicity $G \propto Z'^{1/2}$ because of the H_2-dust cutoff. For $Z' = 10$, 1, 0.1, and 0.01, we find that G equals 1.3×10^{-4}, 2.8×10^{-5}, 5.4×10^{-6}, and 7.1×10^{-7}. For these metallicities, the average self-shielded dissociation rates are $D_0G/2 = 3.8\times10^{-15}$, 8.1×10^{-16}, 1.6×10^{-16}, and 2.1×10^{-17} s^{-1}. As discussed in Section 2.2.6 the average is over an H_2-dust optical depth $\tau_2 \sim 1$. For low metallicities, $D_0G/2$ becomes very small because the LW radiation is fully absorbed in lines at very low H_2-dust optical depths.

3.1.4. H I-to-H_2 Transition Profiles

We now present illustrative computations for the H I-to-H_2 transition profiles for a range of αG spanning the weak- to strong-field limits, and for metallicities Z' from high to low, for beamed and isotropic fields.

As discussed in Section 2.2.5, the profile shapes, i.e., the density ratios n_1/n and $2n_2/n$ as functions of the dust optical depth $\tau_g \equiv \sigma_g N$ (where $N \equiv N_1 + 2N_2$), depend on just the single dimensionless parameter $\alpha G \equiv D_0G/Rn$. This includes the locations of the H I-to-H_2 transition points expressed in terms of τ_g. We define the transition point as the cloud depth where $n_1/n = 2n_2/n = 0.5$. For both beamed and isotropic fields we compute five transition profiles for $\alpha G/2 = 0.01$, 0.1, 1, 10, and 10^2, for $Z' = 1$ and $\sigma_g = 1.9\times10^{-21}$ cm^{-2} ($\phi_g = 1$). These sequences illustrate the change in profile shapes, from "gradual" to "sharp," from the weak-field (H I-dust negligible) to strong-field limits (H I-dust dominant). In these computations $G = 2.8\times10^{-5}$ as appropriate for $Z' = 1$, and we set $D_0 = 2\times10^{-9}$ s^{-1} ($I_{\rm UV} \approx 35$) and $R = 3\times10^{-17}$ cm^3 s^{-1} ($T = 100$ K). To alter α and αG, we vary n from 10 to 10^5 cm^{-3}.

For each $\alpha G/2$ we plot the atomic and molecular fractions, n_1/n and $2n_2/n$, as functions of the total (atomic plus molecular) column density, N. For fully atomic gas $n_1/n = 1$, and for fully molecular gas $2n_2/n = 1$. For each model we also plot the

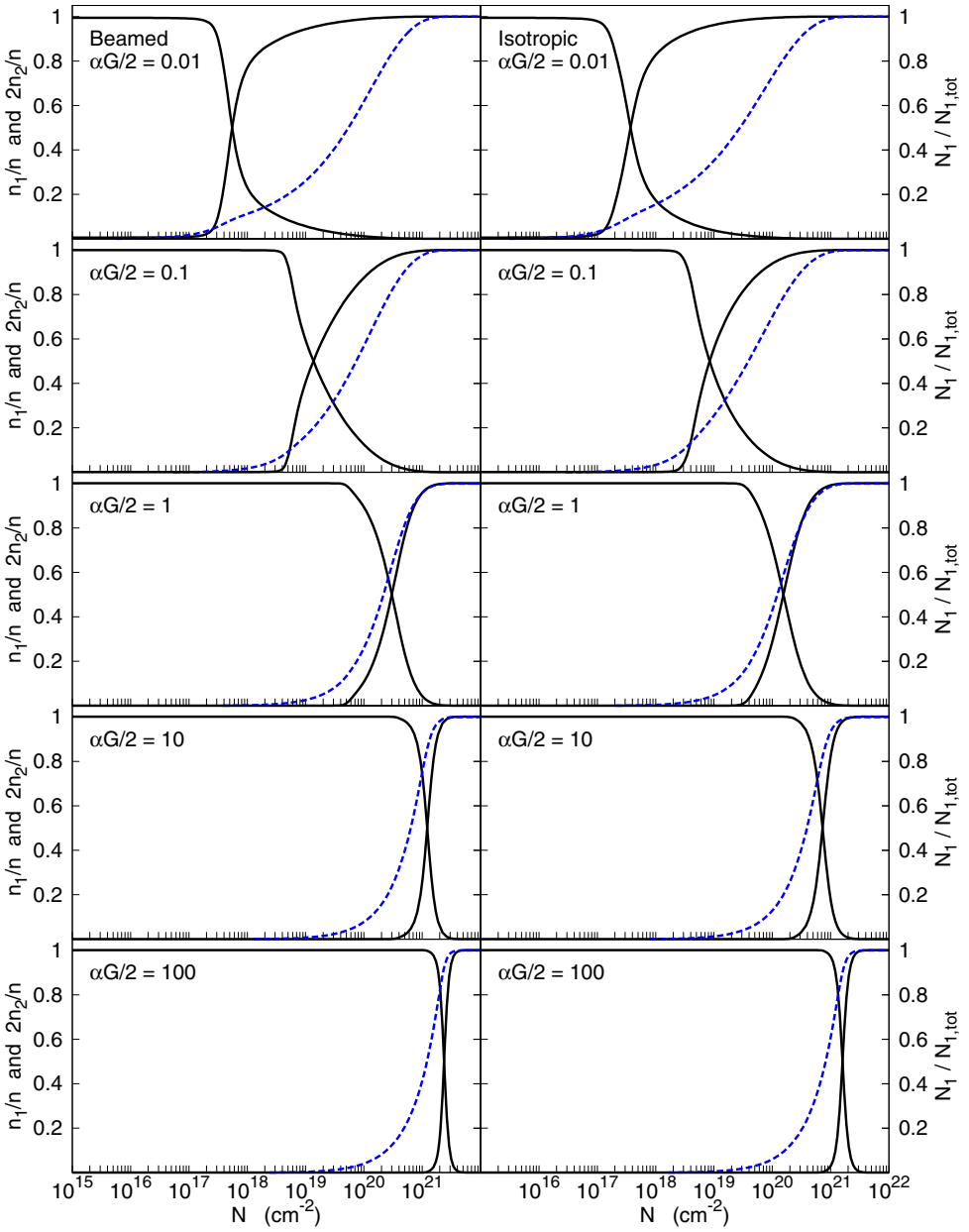

Figure 7. H I/H_2 transitions for beamed (left panels) and isotropic (right panels) radiation fields, for $\alpha G/2$ ranging from 0.01 (top panels) to 100 (bottom panels). The solid curves show the atomic and molecular gas fractions, n_1/n and $2n_2/n$, as functions of the total gas column density N into the cloud. The (blue) dashed curves are the normalized atomic columns, $\tilde{N}_1 \equiv N_1/N_{1,\rm tot}$, as functions of cloud depth.

(A color version of this figure is available in the online journal.)

normalized atomic column, $\tilde{N}_1 \equiv N_1/N_{1,\rm tot}$, also as a function of N. Thus, $\tilde{N}_1 \rightarrow 1$ at sufficiently large cloud depths where the LW radiation is fully absorbed. The curves for $\tilde{N}_1$ show how and where the atomic column is built up relative to the atomic-to-molecular transition points.

Figure 7, left panels, display the H I-to-H_2 transition profiles for the five beamed-field models with varying αG.

Several important features can be seen in these plots. First, the atomic-to-molecular transition points move deeper into the cloud with increasing αG. For $\alpha G/2 = 0.01$, 0.1, 1, 10, and 10^2, the total gas columns $N_{1\rightarrow 2}$ at the transition points equal 5.6×10^{17}, 1.4×10^{19}, 3.0×10^{20}, 1.2×10^{21}, and 2.4×10^{21} cm^{-2}. For the assumed $\sigma_g = 1.9\times10^{-21}$ cm^{-2}, these columns correspond to total dust optical depths $\tau_g = 1.05\times10^{-3}$, 2.6×10^{-2}, 0.58, 2.3, and 4.5. The H I-dust optical depths at the transition points are 9.0×10^{-4}, 2.0×10^{-2}, 0.45, 2.1, and 4.2. In the weak-field limit, the transition depths increase rapidly with αG. In the strong-field limit, the UV penetration is moderated by H I-dust absorption, and the transition depths increase slowly.

Second, the profile shapes vary with αG. In the weak-field limit, the atomic-to-molecular conversion is controlled by H_2-line self-shielding, but significant H I exists beyond the transition point up to the H_2-dust cutoff. In the weak-field limit, most of the H I column is built up past the transition point where the gas is *predominantly molecular*. In the strong-field limit, the transition point is controlled by (exponential) H I-dust absorption, and most of the H I is built up in an outer full atomic layer. Thus, in the weak-field limit the transitions are *gradual*, and in the strong-field limit the transitions are *sharp*. For example, at the H I-to-H_2 transition points, the normalized atomic column

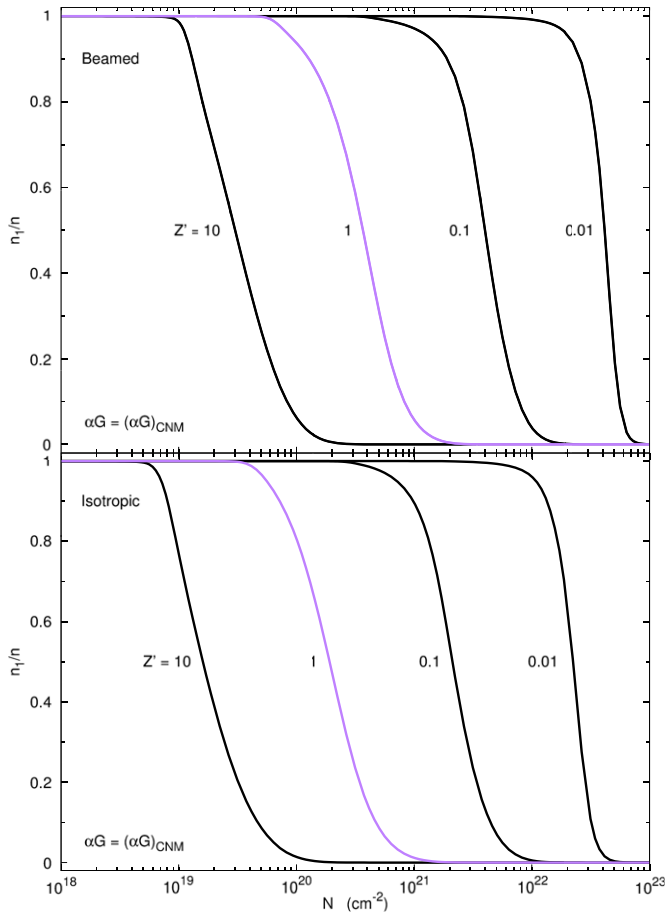

Figure 8. H I gas fractions, n_1/n, for beamed (upper panel) and isotropic (lower panel) radiation, for $\alpha G = (\alpha G)_{\rm CNM}$ for metallicities Z' from 0.01 to 10 times solar.

(A color version of this figure is available in the online journal.)

$\tilde{N}_1 = 0.08$, 0.19, 0.63, 0.85, and 0.92, from small to large αG. For $\alpha G/2 = 0.01$, 92% of the total atomic column is built up past the transition point inside the molecular zone. For $\alpha G/2 = 100$, only 8% of the atomic column is produced past the transition point.

Figure 7, right panels, show the transition profiles for *isotropic* fields for $\alpha G/2$ ranging from 0.01 to 100, for $Z' = 1$ and $\sigma_g = 1.9 \times 10^{-21}$ cm^2. As for the beamed-field models, the shapes of the profiles vary from gradual to sharp from the weak- to strong-field limits. The transition gas columns are $N_{1\rightarrow 2} = 3.7 \times 10^{17}$, 8.4×10^{18}, 1.6×10^{20}, 7.0×10^{20}, and 1.6×10^{21} cm^{-2}, or $\tau_g = 5.8 \times 10^{-4}$, 1.6×10^{-2}, 0.30, 1.4, and 3.0. The normalized atomic columns at the transition points are $\tilde{N}_1 = 0.10$, 0.23, 0.59, 0.82, and 0.90. The H I-dust opacities are 5.8×10^{-4}, 1.3×10^{-2}, 0.24, 1.2, and 2.8.

For fixed αG but varying Z' and σ_g, we expect the profile shapes to be invariant as functions of the dust optical depth τ_g, and we expect the UV penetration scale lengths and transition gas columns, $N_{1\rightarrow 2}$, to vary simply as $1/Z'$ or $1/\sigma_g$. This behavior is illustrated in the upper panel of Figure 8 showing four transition profiles for $Z' = 10$, 1, 0.1, and 0.01 (again for beamed fields). For clarity we only plot the atomic n_1/n curves. For these models we set $\alpha G/2 = (\alpha G)_{\rm CNM}(Z')/2 = 1.11$, 1.30, 1.28, and 1.12, as given by Equation (59) for self-regulated multiphased gas. Because αG is about the same for these models, the profile shapes are indeed very similar, and the transition columns grow inversely with Z'. For these four models, $N_{1\rightarrow 2} = 3.0 \times 10^{19}$, 3.7×10^{20}, 4.0×10^{21}, and 4.2×10^{22} cm^{-2}, corresponding to dust opacities $\tau_g = 0.57$, 0.70, 0.76, and 0.78. The H I-dust opacities at the transition points are 0.46, 0.56, 0.63, and 0.70. This behavior is in excellent agreement with the analytic theory presented in Section 2. For two-phased equilibrium, $\alpha G/2 \sim 1$ for all metallicities and is intermediate between the weak- and strong-field limits for which H I-dust opacity is just becoming significant.

Figure 8, lower panel, shows the n_1/n curves for $Z' = 10$, 1, 0.1, and 1 for the isotropic-field models, with $\alpha G/2 = (\alpha G)_{\rm CNM}(Z')/2$ as for the beamed-field models. Again, because αG is about the same for all four models, the profile shapes are very similar. The transition point columns are $N_{1\rightarrow 2} = 1.6 \times 10^{19}$, 1.9×10^{20}, 2.1×10^{20}, and 2.2×10^{22} cm^{-2}, or $\tau_g = 0.31$, 0.36, 0.40, and 0.42. The H I-dust optical depths at the transition points are 0.25, 0.29, 0.33, and 0.37.

The transition columns and optical depths for all of the isotropic-field models are smaller than for the beamed-field models because of the factor-of-two reductions in the incident fluxes for corresponding isotropic fields with the same αG.

3.1.5. Total H I Columns

A key goal is the computation of the total atomic column densities, $N_{1,\rm tot}$, for beamed and isotropic fields for a comparison with our analytic formulae.

In Figure 9, upper panel, we display $N_{1,\rm tot}$ for beamed fields, as a function of $\alpha G/2$ spanning the range from 0.01 to 100, for $Z' = 10$, 1, 0.1, and 0.01.

For our numerical models, we again set $D_0 = 2 \times 10^{-9}$ s^{-1} and $R = 3 \times 10^{-17} Z'$ cm^3 s^{-1} and vary the gas density n (to select $\alpha \equiv D_0/Rn$), and we set $\sigma_g = 1.9 \times 10^{-21} Z'$ cm^2. For the given input parameters D_0, R, n, and σ_g, we compute the total integrated atomic column density and also calculate $W_{g,\rm tot}$ and the associated average self-shielding factor $G = (\sigma_g/\sigma_d^{\rm tot}) W_{g,\rm tot}$. For each model we compute $N_{1,\rm tot}$ for the corresponding αG and σ_g. The points in Figure 9 are our model results for selected αG and Z'. Again, for the four metallicities, $G = 1.3 \times 10^{-4}$, 2.8×10^{-5}, 5.4×10^{-6}, and 7.1×10^{-7}. The curves in Figure 9 are as given by our fundamental analytic formula for beamed fields

$$N_{1,\rm tot} = \frac{1}{\sigma_g} \ln\left[\frac{\alpha G}{2} + 1\right], \qquad (73)$$

where $1/\sigma_g = 5.3 \times 10^{20}/Z'$ cm^{-2} as for the numerical models.

Our analytic and numerical results are in excellent agreement from the weak- to strong-field regimes. For weak fields (high gas densities), $N_{1,\rm tot} = (1/\sigma_g)\alpha G/2 = (1/2)\bar{F}_\nu W_{g,\rm tot}/Rn$ (Equation (52)). In this regime the total atomic column is proportional to the field intensity (dissociation flux) and varies inversely with the gas density. For strong fields (low densities), the dependence is logarithmic and $N_{1,\rm tot} = (1/\sigma_g)\ln(\alpha G)$ (Equation (54)). In this regime the atomic column is weakly dependent on $I_{\rm UV}/n$, and it is limited to values close to $1/\sigma_g$ because of the dominating H I-dust absorption. For example, for $Z' = 1$ and $\alpha G/2 = 0.01$, 0.1, 1, 10, and 100, our model computations give $N_{1,\rm tot} = 5.6 \times 10^{18}$, 5.3×10^{19}, 3.8×10^{20}, 1.2×10^{21}, and 2.4×10^{21} cm^{-2}, as also given by our analytic formula.

Expressed as a function of αG, $N_{1,\rm tot} \propto 1/Z'$. However, we recall that for large σ_g ($Z' \gtrsim 1$), αG is itself metallicity dependent and $\alpha G \propto Z'^{1/2}$ (see Equation (51)). Thus, for high metallicities in the weak-field limit, $N_{1,\rm tot} \propto Z'^{-3/2}$.

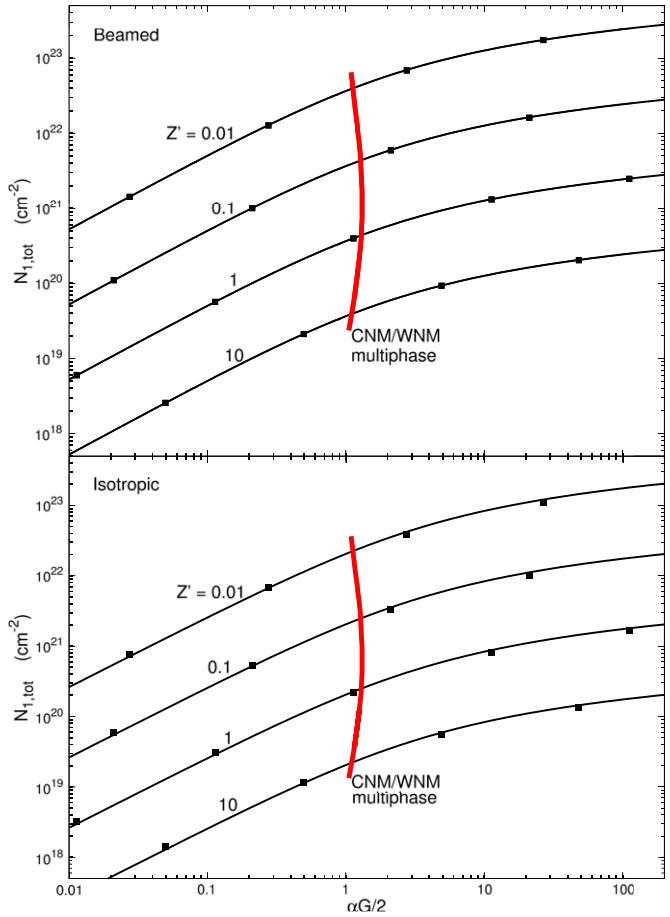

Figure 9. Total H I column as a function of $\alpha G/2$ for beamed (upper panel) and isotropic (lower panel) radiation, for metallicities Z' from 0.01 to 10 times solar. The square points are the numerical results, and the solid (black) curves are as given by our analytic formulae (Equations (40) and (65)). The red curves show $(\alpha G)_{\rm CNM}$ as functions of Z' for self-regulated two-phased equilibrium.
(A color version of this figure is available in the online journal.)

In this regime the column decreases by one power of Z' because of enhanced H_2 formation efficiency and decreases by an additional factor of $Z^{1/2}$ because of the reduction of the effective dissociation flux by the H_2-dust. For low metallicities in the weak-field limit, the dissociation flux is maximal, and $N_{1,\rm tot} \propto Z'^{-1}$. In the strong-field limit, the atomic column is only weakly (logarithmically) dependent on αG, and the metallicity dependence is mainly via the H I-dust opacity, and $N_{1,\rm tot} \propto Z'^{-1}$ for all metallicities. These metallicity scalings, discussed in Section 2.2.8, are validated by our numerical model results for the atomic column.

In Figure 9 we also plot a (red) curve for $(\alpha G)_{\rm CNM}(Z')$ as given by Equation (59) for self-regulated multiphased H I. As is again illustrated in Figure 9, $(\alpha G)_{\rm CNM}(Z')/2 \sim 1$. Given the assumptions underlying Equation (59), the H I columns for self-regulated multiphased gas are intermediate between the linear (weak-field) and logarithmic (strong-field) regimes for all metallicities.

Our computational results show that our analytic expression for $N_{1,\rm tot}$ is valid for *all* transition profile shapes, whether gradual (weak fields) or sharp (strong fields), regardless of where the atomic column is built up (whether in the molecular zone or in the outer fully atomic layer). Indeed, in our analytic derivation we did not make any assumptions on the profile shape. Our expression is universal and valid for all regimes (weak and strong fields, high and low metallicities) and for all transition profile shapes (gradual or sharp). We emphasize this point again in our alternate derivation via the KMT/MK10 "transfer-dissociation equation" (Section 4.1.1).

In Figure 9, lower panel, we plot the total atomic columns for our isotropic-field models. For these models we select D_0 and R, and vary n to set α, and we compute the total H I column. As discussed in Section 3.2, the total dust-limited dissociation bandwidth, $W_{\rm tot}$, and the average self-shielding factor, G, are identical for beamed and isotropic fields. In Figure 12 we plot $N_{1,\rm tot}$ as a function of αG, where for each Z' we use the $G(Z')$ computed using beamed fields. Again, αG ranges from 0.01 to 100, and we present results for Z' from 10 to 0.01. The $(\alpha G)_{\rm CNM}(Z')$ curve is also displayed. In Figure 9, the points are our numerical results, and the curves are as given by our fundamental analytic formula for isotropic fields (Section 2.3),

$$N_{1,\rm tot} = \frac{\langle\mu\rangle}{\sigma_g} \ln\left[\frac{1}{\langle\mu\rangle}\frac{\alpha G}{4} + 1\right], \quad (74)$$

where again $1/\sigma_g = 5.3 \times 10^{20}/Z'$ cm^{-2}. To obtain the match between the numerical results and analytic formula shown in Figure 9, we have fit for the average angle factor $\langle\mu\rangle$. We find that

$$\langle\mu\rangle = 0.8 \quad (75)$$

provides an excellent fit for all αG and for all $\sigma_g \propto Z'$.

For isotropic fields in the weak-field limit, $N_{1,\rm tot} = (1/\sigma_g)\alpha G/4 = (1/4)\bar{F}_\nu W_{g,\rm tot}/Rn$ (Equation (68)). As discussed in Section 2.3, this is half the column for the corresponding beamed field because of the factor-of-two difference in the incident dissociation fluxes. For weak fields, $N_{1,\rm tot}$ is independent of $\langle\mu\rangle$. In the strong-field limit, $N_{1,\rm tot} = (\langle\mu\rangle/\sigma_g)\ln(\alpha G/4\langle\mu\rangle)$ (Equation (69)), and the column is reduced by the factor $\langle\mu\rangle = 0.8$ compared with beamed-field models (neglecting the small difference in the logarithms). For example, for $Z' = 1$ and $\alpha G/2 = 0.01$ 0.1, 1, 10, and 100, our model results for the total atomic column are 3.1×10^{18}, 2.9×10^{19}, 2.1×10^{20}, 7.7×10^{20}, and 1.6×10^{21} cm^{-2}, smaller in the expected way compared with beamed-field models. The linear and logarithmic behaviors for small and large $\alpha G \propto I_{\rm UV}/n$ and the scaling with Z' are identical for isotropic and beamed fields.

Our expression for the total column for isotropic fields is also valid for all profile shapes, from gradual to sharp.

4. COMPARISON WITH KMT/MK10

In a series of papers, Krumholz et al. (2008, 2009) and McKee & Krumholz (2010; hereafter KMT/MK10) considered the interstellar atomic-to-molecular transition in the context of galaxy-wide conditions for star formation. For this purpose, KMT/MK10 developed analytic models for the H I-to-H_2 transitions in *spherical* clouds irradiated by isotropic radiation fields. They also considered planar models. KMT/MK10 were particularly interested in exploring the role of metallicity in setting star-formation thresholds, and in MK10 they applied their spherical models to compute metallicity-dependent H_2 mass fractions in star-forming clouds as functions of the gas mass surface densities in galaxy disks. The integral H_2 mass fraction, $f_{\rm H_2}$, may be a critical parameter in galaxy-wide Kennicutt–Schmidt (KS) relations, especially if conversion to H_2 is required for star

formation.[15] For spheres, $f_{H_2} \equiv M_{H_2}/M_{gas}$, where M_{H_2} and M_{gas} are the molecular and total gas masses within the volumes. For slabs $f_{H_2} \equiv \Sigma_{H_2}/\Sigma_{gas}$, where Σ_{H_2} and Σ_{gas} are the molecular and total gas mass surface densities in the normal directions.

The assumption of spherical versus plane-parallel geometry complicates the analysis and computation of the H I-to-H_2 transition because for spheres oblique rays cross through the clouds even when optically thick H_2 cores are present. Optically thick slabs are simpler because all rays are absorbed. To proceed, KMT/MK10 made the simplifying assumption that the H I-to-H_2 transitions are always sharp, such that any atomic layer has a well-defined length scale. For the spheres, fully atomic and dusty H I shells are then assumed to surround fully molecular H_2 cores. Rays that cross through the H I shells are either unattenuated or are absorbed by dust, or by H_2-lines under the assumption that the molecular fractions in the shells are small. Rays that impinge on the H_2 cores are fully attenuated. MK10 employ a "variable Eddington factor" formalism to close the angular moments of the radiative transfer equation for the radiation fields in the H I shells. For a given total cloud mass and radiation field intensity, a complicated iterative procedure then yields the spherical and nested H I/H_2 structures, and associated H_2 mass fractions.

KMT/MK10 implicitly assumed that the H_2-lines are always in the fully overlapping regime, independent of Z' and σ_g, and they did not consider the possible reduction of the effective dissociation bandwidth by H_2-dust. KMT/MK10 did not make the distinction between H I-dust and H_2-dust that we have been emphasizing.

According to KMT/MK10, the spherical H I/H_2 "shell–core" structures depend on two dimensionless parameters, "χ" and "τ_r." In their definition, "χ/f_1 is the ratio of the number of LW photons absorbed by dust to the number absorbed by H_2," where f_1 is the fraction of gas in atomic form. As we clarify below, χ is actually identical to our αG in the low-Z', small-σ_g, ($w = 1$) limit where H_2-dust absorption is negligible. The second parameter, $\tau_r \equiv n\sigma_g r$, is the "dust optical depth associated with the cloud radius r," where n is the hydrogen nucleon density at the cloud surface. For a slab (of finite width) the corresponding second parameter is the total dust optical depth $\tau_z \equiv \sigma_g n z$ through the slab, where z is the linear extent. The parameters τ_r and τ_z will enter into our discussion of the H_2 mass fractions for spheres and slabs (Section 4.2).

We wish to compare our analytic theory for the H I column densities for planar clouds with the KMT/MK10 formulae for spheres. This will enable us to also compare results for the H_2 mass fractions. We will show that any differences between corresponding (i.e., properly normalized) slabs and spheres are very small and that it is therefore advantageous to use our much simpler and fully analytic plane-parallel formalism.

We start (in Section 4.1) by clarifying the relationship between the KMT/MK10 χ and our αG. To do this we reanalyze the "transfer-dissociation equation" presented by Krumholz et al. (2008). This also enables a comparison of our formulae for the H I columns with KMT/MK10's similar, though not identical, expressions for the atomic columns for planar geometry. In Section 4.2.1 we develop a simple expression for f_{H_2} for optically thick slabs for two-sided irradiation using our analytic expressions for the total H I-dust optical depths for one-sided irradiation of semi-infinite clouds, for isotropic or beamed fields. In Section 4.2.2 we re-express the MK10 formulae for uniform density (isochoric) spheres and (isobaric) "atomic–molecular complexes" for (1) the critical H I-dust optical depths required for the formation of H_2 cores and (2) the H_2 mass fractions as functions of the total cloud optical depths (or gas masses). This will enable a clear comparison with our expressions for slabs.

We find that for corresponding spheres and slabs embedded in isotropic fields, the predicted H I columns are very similar. The differences are no greater than 20% for αG ranging from 0.01 to 100. For two-phased H I equilibria for which $\alpha G/2 \sim 1$, the differences between spheres and slabs are negligible, and the H I columns for spheres and slabs are essentially identical. In fact, we show that switching from a beamed to an isotropic field for a slab is much more significant than switching from a slab to a sphere for a fixed isotropic field. We then show that for proper normalization of the three configurations—uniform sphere, complex, or slab—the predicted H_2 mass fractions as functions of total cloud masses or columns are also very similar.

4.1. χ and αG

To clarify the relationship between the KMT/MK10 χ and our αG, it is useful to consider the "transfer-dissociation equation" developed by Krumholz et al. (2008), here for beamed radiation into a slab. This discussion will also provide an alternate derivation of our fundamental formula (Equation (40)) for the total H I column density.

4.1.1. Transfer-dissociation Equation

Let $F_\nu(z)$ be the flux density (photons cm^{-2} s^{-1} Hz^{-1}) at frequency ν of beamed LW radiation at linear depth z into a slab. The radiation flux (cm^{-2} s^{-1}) between frequencies ν_1 and ν_2 is then

$$F(z) \equiv \int_{\nu_1}^{\nu_2} F_\nu(z)\, d\nu. \tag{76}$$

At the cloud surface $F(0) = F_0/2$, where F_0 is the flux integral (our Equation (3)) for the free-space radiation field.

The transfer equation for $F(z)$ is

$$\frac{dF}{dz} = -n\sigma_g F - n_2 \int_{\nu_1}^{\nu_2} \sigma_\nu F_\nu\, d\nu. \tag{77}$$

Here $n \equiv n_1 + 2n_2$ is the total (atomic plus molecular) hydrogen gas volume density, and σ_ν is the ("complicated") cross section for the multiline H_2 absorption process.[16] The first term on the right-hand side of Equation (77) is the dust absorption rate of the local radiative flux. The second term is the H_2-line absorption rate.

The steady state H_2 formation–destruction equation is

$$Rnn_1 = \bar{f}_{diss} n_2 \int_{\nu_1}^{\nu_2} \sigma_\nu F_\nu(z)\, d\nu, \tag{78}$$

where in this expression, $\bar{f}_{diss}$ (as defined in Section 2) is the mean fraction of all H_2-line absorptions that lead to photodissociation. Following Krumholz et al. (2008) and our discussion in Section 2, we assume that $\bar{f}_{diss}$ is independent of cloud depth.

[15] For example, in the expression $\dot{\Sigma}_{SFR} = \epsilon f_{H_2} \Sigma_{gas}/\tau_{dyn}$, the molecular fraction f_{H_2} enters as a threshold, and the star-formation rate is quenched as f_{H_2} becomes small. In this form of the KS relation, $\dot{\Sigma}_{SFR}$ is the star-formation rate per unit mass surface density, Σ_{gas} is the total gas mass surface density, τ_{dyn} is the dynamical time, and ϵ is the star-formation efficiency per dynamical time.

[16] The product $\bar{f}_{diss} \int \sigma_\nu\, d\nu$ is the total dissociation cross section σ_d^{tot} (Equation (13)), Section 2.2.1).

The "complicated" integral in Equation (77) may be eliminated to give the transfer-dissociation equation (Krumholz et al. 2008)

$$\frac{dF}{dz} = -n\sigma_g F - \frac{Rnn_1}{\bar{f}_{\rm diss}}. \quad (79)$$

In dimensionless form

$$\frac{d\mathcal{F}}{d\tau} = -\mathcal{F} - \frac{2}{\chi} f_1, \quad (80)$$

where $\mathcal{F} \equiv F/F(0)$ is the normalized depth-dependent flux, $\tau \equiv n\sigma_g z$ is the dust optical depth, and $f_1(\tau) \equiv n_1/n$ is the depth-dependent fraction of gas in atomic form.

In Equation (80)

$$\chi \equiv \frac{\bar{f}_{\rm diss}\sigma_g F_0}{Rn}. \quad (81)$$

This is the KMT/MK10 χ, here introduced for one-sided irradiation of a slab by a beamed field with incident LW flux $F(0) \equiv F_0/2$.[17] Compared with our Equation (48) it is already clear that $\chi = \alpha G$ for $w = 1$.

Because the product $\sigma_g n F_0$ is the dust absorption rate per unit volume of the surface LW radiation flux, and because $Rn^2 f_1/\bar{f}_{\rm diss}$ is the H_2-line absorption rate per unit volume, KMT/MK10 interpret χ/f_1 as the ratio of the number of LW photons absorbed by dust to the number absorbed by H_2-lines at the optically thin cloud surface (with one factor of n canceling when doing the division). In this interpretation, the dust absorption being referred to in the numerator is *independent of whether the gas is atomic or molecular*.

However, as we now show, if the dust absorption term in the transfer-dissociation equation is redefined to refer to H I-dust absorption only, we will recover our fundamental formula for the H I column density, including a method for "renormalizing" the dissociation flux to account for H_2-dust absorption. We demonstrate this by analyzing the transfer-dissociation equation in the following three steps.

4.1.2. Step 1: Transition Assumed Sharp

First, we assume—as done by KMT/MK10—that the atomic-to-molecular transition is *always* sharp. We impose this assumption even though we know that it is good only if our $\alpha G \gg 1$, i.e., only if F_0/n and χ are sufficiently large. Nevertheless, in seeking a solution for Equation (80), we assume that for any χ the atomic fraction $f_1 = 1$ everywhere $\mathcal{F}$ is non-zero, up to the (unknown) transition point where $\mathcal{F}$ vanishes. At that point the gas switches suddenly from H I to H_2.

Setting $f_1 = 1$, the solution to Equation (80) is

$$\mathcal{F}(\tau) = \frac{\chi + 2}{\chi} e^{-\tau} - \frac{2}{\chi}. \quad (82)$$

It is evident that the flux vanishes for $\tau = \tau_{1,\rm tot}$, where

$$\tau_{1,\rm tot} \equiv \ln\left[\frac{\chi}{2} + 1\right], \quad (83)$$

and this is then the solution for the transition point (Krumholz et al. 2008). The total atomic column density up to the transition point is

$$N_{1,\rm tot} = \frac{1}{\sigma_g} \ln\left[\frac{\chi}{2} + 1\right], \quad (84)$$

because by assumption there is no H_2 in the photodissociated layer and τ_1 is the optical depth due to H I-dust only.

We immediately recognize Equations (83) and (84). They are identical to our expressions (40) and (43) for the total H I-dust optical depth and H I column density, except that here the argument is χ, as given by Equation (81), rather than our αG as defined by the similar but not quite identical Equation (48). Indeed, it is apparent that $\alpha G = w\chi$, where w is the normalized effective dissociation bandwidth as defined by Equation (31). (This identity is clarified in *Step 3*.)

For $\chi \gg 1$, the attenuation of the LW flux is dominated by dust absorption, and $\mathcal{F}(\tau) \approx e^{-\tau}$. An exponentially attenuating flux is precisely what produces a sharp transition profile. Therefore, for $\chi \gg 1$ the assumption that the transition is sharp is consistent. Furthermore, the exponential attenuation is due specifically to H I-dust absorption. Sharp profiles occur when H I-dust dominates the attenuation.

For $\chi \ll 1$, dust absorption is negligible compared with H_2-lines, $\tau \ll 1$ throughout the atomic layer, and $\mathcal{F}(\tau) = 1 - 2\tau/\chi$ to first-order in τ. For small χ, Equation (83) gives $\tau_{1,\rm tot} = \chi/2$, so that

$$N_{1,\rm tot} = \frac{1}{\sigma_g}\frac{\chi}{2} \quad (85)$$

in this limit. However, when H_2-lines dominate the attenuation the transition is not sharp, and the assumption that $f_1 = 1$ is inconsistent.

Nevertheless, as we now show in *Step 2*, the above expressions for $\mathcal{F}(\tau)$, τ_1, and $N_1^{\rm tot}$ for large and small χ are valid for *any* varying f_1, *whether or not* the H I/H_2 transition is sharp, provided that H_2-dust is always negligible compared with H I-dust or H_2-lines, so that τ in Equation (80) can be redefined as the optical depth associated with H I-dust absorption only.[18]

4.1.3. Step 2: H_2-dust Negligible, and τ Redefined

With the neglect of H_2-dust absorption, Equation (79) is

$$\frac{dF}{dz} = -n_1\sigma_g F - \frac{Rnn_1}{\bar{f}_{\rm diss}}, \quad (86)$$

where now n has been replaced by n_1 in the first term on the right-hand side, or

$$\frac{d\mathcal{F}}{d\tau} = -\mathcal{F} - \frac{2}{\chi}, \quad (87)$$

where χ is again given by Equation (81) but where now

$$\tau \equiv \sigma_g \int_0^z n_1\, dz \quad (88)$$

is defined in advance as the optical depth associated with H I-dust only.

[17] When Krumholz et al. (2008) defined their χ via the transfer-dissociation equation, they wrote the surface flux $F(0)$ in the numerator, rather than the full 4π free-space F_0. However, when discussing spherical models, KMT/MK10 *redefine* their χ and replace $F(0)$ with F_0 in the numerator. In this paper we use the free-space F_0 throughout, including here in our discussion of the transfer-dissociation equation. With this adjustment a factor of two appears in the second term on the right-hand side of Equation (80), which is not there in Krumholz et al. (2008).

[18] Indeed, we know that our Equations (40) and (43) are valid for all αG, *whether or not* the H I-to-H_2 transition is sharp. This suggests that although we assumed $f_1 = 1$ to derive Equations (83) and (84), they are valid even when χ is small and the transition is not sharp.

In Equations (86) and (87), a factor $f_1 \equiv n_1/n$ does not appear. The solutions are still given by Equations (84) and (85) for large and small χ but now with *no* assumptions on the shapes of the transition profiles.

For large χ the transition is sharp because the radiation flux is attenuated exponentially by the H I-dust, as shown in *Step 1*. However, for low χ, for which $\tau_{1,\rm tot}$ is small, the transition need not be sharp. In this limit we again have,

$$N_{1,\rm tot} = \frac{1}{\sigma_g}\frac{\chi}{2} = \frac{\bar{f}_{\rm diss}F_0/2}{Rn}. \quad (89)$$

But this is just a Strömgren relation (as also noted by MK10). Therefore, it must hold *independent* of the shape of the H I/H_2 profile, provided only that the entire incident dissociation flux, $\bar{f}_{\rm diss}F_0/2$, is fully absorbed by H_2-lines, which it indeed will be for small $\tau_{1,\rm tot}$. Again, $RnN_{1,\rm tot}$ is the integrated H_2 formation rate per unit area, and in steady state this equals the fully absorbed dissociation flux $\bar{f}_{\rm diss}F_0/2$ impinging on the surface, independent of profile shape. In fact, we know that for low χ (i.e., for small F_0/n and αG) the transition profile is gradual, with most of the H I column built up in the molecular zone, as we have shown and discussed in Section 3.

Although Krumholz et al. (2008) derived their expression (83) for the dust optical depth assuming a sharp transition, it is actually valid for all χ, large and small, for sharp *and* gradual atomic hydrogen profiles, provided that H_2-dust absorption is negligible compared with H I-dust and H_2-lines.

4.1.4. Step 3: H_2-dust and Renormalization of the Dissociation Flux

We now include H_2-dust. In Equations (79) and (80), the original dust absorption term, $n\sigma_g F$, is not necessarily negligible—even when $\chi \ll 1$—if the atomic fraction f_1 is sufficiently small. This is the regime where H_2-dust absorption may be significant, even if H I-dust is negligible.

Because of H_2-dust absorption of radiation "between the lines," not all of the photons in the LW band are absorbed by the H_2, even for a fully molecular slab. The effective dissociation flux is then smaller than $\bar{f}_{\rm diss}F_0/2$. The Strömgren relation then implies that for $\chi \ll 1$ the total H I-dust optical depth $\tau_{1,\rm tot}$ must be *smaller* than $\chi/2$, rather than equal to $\chi/2$ as given by Equation (89).

If τ is redefined to refer to H I-dust only as in *Step 2*, the effect of H_2-dust absorption can be included in the transfer-dissociation equation by a simple "renormalization" of the effective dissociation flux. We replace $F_0/2$ with a suitably reduced $wF_0/2$ equal to the flux of LW photons absorbed in H_2-lines in a dusty molecular slab, *excluding in advance* photons that are inevitably absorbed by H_2-dust. The renormalization factor can be computed in advance for any given σ_g, and we immediately recognize w as the (normalized) effective dissociation bandwidth that we defined and computed in Sections 2 and 3.

The transfer-dissociation equation for the renormalized LW flux is

$$\frac{d(wF)}{dz} = -n_1\sigma_g wF - \frac{Rnn_1}{\bar{f}_{\rm diss}}, \quad (90)$$

where again the dust term on the right-hand side refers to H I-dust absorption only. Photons absorbed by H_2-dust anywhere in the slab are excluded from consideration "in advance."

In dimensionless form

$$\frac{d\mathcal{F}}{d\tau} = -\mathcal{F} - \frac{2}{\chi'}, \quad (91)$$

where $\mathcal{F} \equiv F/F(0)$, $d\tau \equiv n_1\sigma_g z$, and

$$\chi' \equiv w\chi = \frac{\bar{f}_{\rm diss}\sigma_g wF_0}{Rn}. \quad (92)$$

We see that χ' is just our αG (Equation (48)). Thus,

$$\alpha G = w\chi \quad (93)$$

as already indicated in *Step 1*.

Most importantly, in Equations (90) and (91) a factor "f_1" does not appear at all. The solution is

$$\mathcal{F}(\tau) = \frac{\chi'+2}{\chi'}e^{-\tau} - \frac{2}{\chi'}, \quad (94)$$

where τ is the H I-dust optical depth, and there are *no* assumptions on the shape of the H I-to-H_2 transition profile. The flux vanishes for $\tau = \tau_1$, where

$$\tau_{1,\rm tot} = \ln\left[\frac{\chi'}{2}+1\right] = \ln\left[\frac{\alpha G}{2}+1\right], \quad (95)$$

and the expression for the total atomic column is then

$$N_{1,\rm tot} = \frac{1}{\sigma_g}\ln\left[\frac{\alpha G}{2}+1\right]. \quad (96)$$

We have thus recovered our original expressions (39) and (40) for the total atomic column and H I-dust opacity for beamed radiation into a slab. It is again clear that these expressions are general. They are valid for large or small αG (strong or weak fields) for the regimes of significant H I-dust and/or H_2-dust absorption and are independent of the profile shapes (gradual or sharp). We also have in Equation (94) a closed-form expression for the depth-dependent LW-band flux as a function of the H I-dust optical depth.

We again see that αG is the fundamental dimensionless parameter. Physically, αG is the ratio of the H I-dust to H_2-line absorption rates of the effective dissociation flux, excluding any LW photons that are absorbed by H_2-dust. The relationship between χ and our αG is now clear. Specifically, $w\chi \equiv \alpha G$, where crucially our factor w accounts for H_2-dust absorption and the resulting reduction of the effective dissociation flux. In the low-Z', small-σ_g limit, H_2-dust is negligible, $w = 1$, and $\chi = \alpha G$. For high Z' and large σ_g, $w < 1$ (decreasing as $\sigma_g^{-1/2}$ or as $Z'^{-1/2}$), and then $\alpha G < \chi$. KMT/MK10 did not make the distinction between H I-dust and H_2-dust and ignored the effects of H_2-dust entirely in their definition of χ. As we have discussed in Sections 2 and 3, H_2-dust can reduce the effective dissociation bandwidth by a factor ~4 for the (realistic) range of metallicities in galaxies.

In Figure 10 we again schematically summarize the four regimes that are incorporated by our formula for the total H I column density. In each quadrant, large or small αG for large or small Z', we indicate the shape of the H I-to-H_2 transition (sharp or gradual), the dominant source of opacity (H I-dust, H_2-lines, or H_2-lines plus H_2-dust), and the expression for the H I-dust opacity in terms of the parameters σ_g, F_0, Rn, and w.

4.2. Critical H I-dust Opacities and H_2 Mass Fractions: Slabs versus Spheres

4.2.1. Slabs

Given our expressions (Equation (40) or Equation (65)) for the total H I-dust optical depths in semi-infinite slabs, we can write

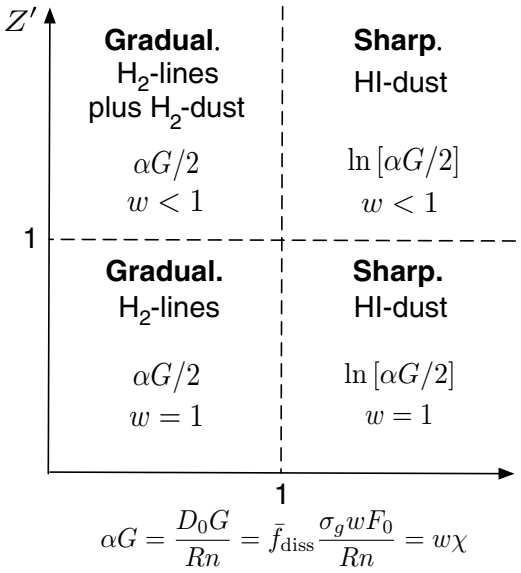

Figure 10. Dominant sources of far-UV absorption (H I-dust, H_2-lines, and H_2-dust), H I-to-H_2 transition profile shapes (gradual or sharp), and total H I-dust opacities (large or small), in the $\alpha G = D_0 G/(Rn) = \bar{f}_{\rm diss}\sigma_g w F_0/(Rn) \equiv w\chi$ vs. Z' plane.

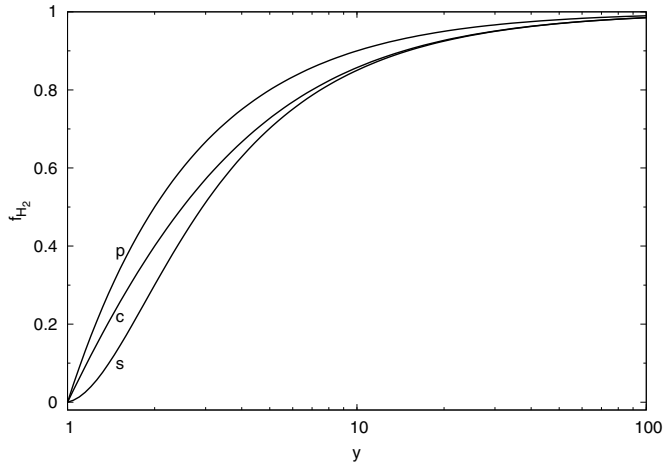

Figure 11. H_2 mass fractions as given by Equations (97), (100), and (102), for plane-parallel slabs ("p"), uniform-density spheres ("s"), and complexes ("c"), as functions of the normalized H I-dust optical depth y.

down a simple formula for the integrated H_2 mass fraction, f_{H_2}, for planar geometry for a comparison with the KMT/MK10 results for spheres. Our main focus is a comparison of slabs and spheres irradiated by isotropic fields, but we also consider beamed radiation for slabs.

For an isotropic field with a given $I_{\rm UV}$, a uniformly illuminated sphere corresponds to *two-sided* irradiation of a slab of finite width, with properly normalized total optical depths for the sphere and slab. For a slab with total dust thickness $\tau_z \equiv \sigma_g n z = \sigma_g N$ (where N is the total gas column density in the normal direction), the H_2 mass fraction is simply

$$f_{H_2}^{\rm p} = 1 - \frac{1}{y}, \qquad (97)$$

where $y \equiv \tau_z/\tau_1$, and τ_1 is the H I-dust depth summed over both sides of the slab (the superscript "p" indicates plane-parallel slab). By definition, $y \geqslant 1$. We plot $f_{H_2}^{\rm p}$ versus y in Figure 11.

For *optically thick* slabs in which the radiation incident on both sides is fully absorbed, and for illumination by isotropic fields, $\tau_1 = \tau_1^{\rm p}$, where

$$\tau_1^{\rm p} = 2\langle\mu\rangle \ln\left[\frac{1}{\langle\mu\rangle}\frac{\alpha G}{4} + 1\right] = 1.6 \ln\left[\frac{\alpha G}{3.2} + 1\right]. \qquad (98)$$

This is twice the optical depth given by our Equation (66) for one-sided illumination of a semi-infinite slab. (We have set $\langle\mu\rangle = 0.8$, as found in Section 3.) For beamed radiation $\tau_1 = \tau_1^{\rm p,b}$, where

$$\tau_1^{\rm p,b} = 2 \ln\left[\frac{\alpha G}{2} + 1\right], \qquad (99)$$

given our Equation (39) for one-sided illumination (the superscript "b" is for beamed radiation). We plot $\tau_1^{\rm p}$ and $\tau_1^{\rm p,b}$ versus αG in Figure 12.

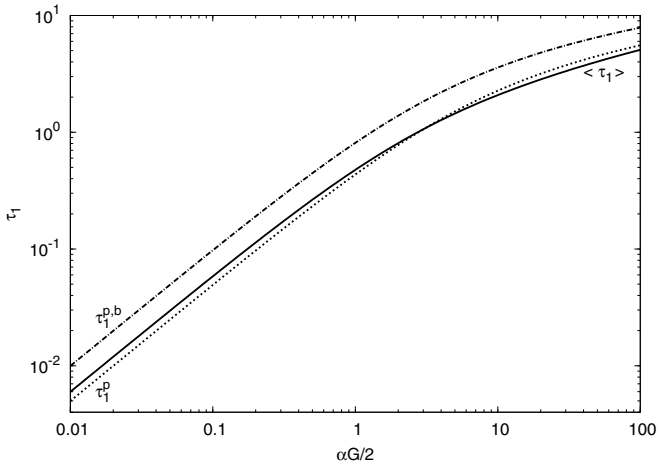

Figure 12. Critical (total) H I-dust optical depths; $\tau_1^{\rm p,b}$ for beamed fields into a slab (dot-dashed), $\tau_1^{\rm p}$ for isotropic fields into a slab (dotted), and $\langle\tau_1\rangle$ for critical spheres in isotropic fields (dotted), as functions of $\alpha G/2$, as given by Equations (99), (98), and (101).

For two-sided illumination of optically thick slabs, Equation (97) for f_{H_2} together with Equation (98) or Equation (99) for the total H I-dust optical depths may be used to compute the integral H_2 mass fractions whether the H I-to-H_2 transitions are gradual or sharp. For $\alpha G \gg 1$, an optically thick slab consists of a simple H I-H_2-H I sandwich structure, with two fully atomic layers outside an inner H_2 zone, with sharp transitions between the atomic and molecular layers. For sharp transitions a "critical" optically thick slab occurs for $y = 1$ for which an H_2 layer just appears at the midplane, and $\tau_1^{\rm p}$ or $\tau_1^{\rm p,b}$ are then the critical H I-dust optical depths. The planar sandwich for sharp transitions corresponds to the spherical core–shell structures considered by KMT/MK10, as illustrated in Figure 13.

4.2.2. Spheres

MK10 carried out their iterative radiative transfer procedure to compute spherical H I shell and H_2 core structures for two types of systems. First, they considered "uniform density" spheres for which the density of hydrogen nuclei, $n = n_1 + 2n_2$, is constant through the spheres as in our slabs. Second, they considered "atomic–molecular complexes" in which the H_2 gas density, n_2, is 10 times the atomic density, n_1, for approximate pressure equilibrium between the shells and the cores. MK10 then presented fitting formulae (their Equations (82) and (93)) for f_{H_2} in uniform density spheres and complexes, as functions of their cloud parameters χ and τ_r.

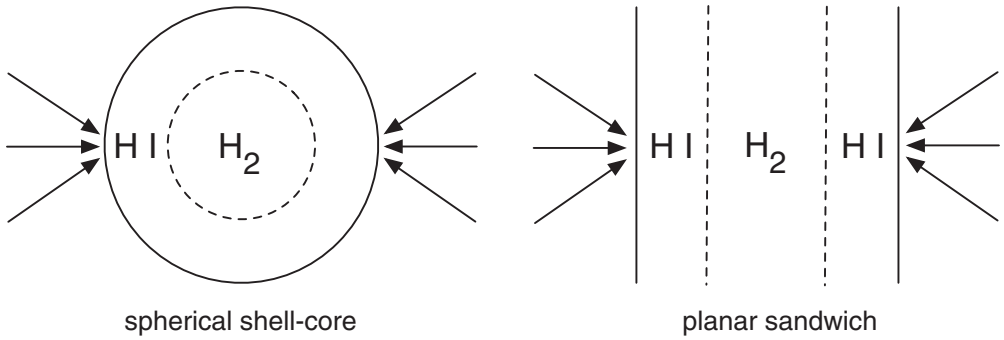

Figure 13. Corresponding shell–core structures for spheres and sandwich structure for slabs, for sharp H I-to-H_2 transitions and illumination by isotropic radiation.

We can re-express the MK10 formulae for f_{H_2} as simple functions of y, similar to our Equation (97) for slabs. For spheres $y \equiv \langle\tau\rangle/\langle\tau_1\rangle$, where $\langle\tau\rangle \equiv \sigma_g\langle N\rangle$ is the area-averaged total dust column density of the sphere and where $\langle N\rangle \equiv M_{\rm gas}/m\pi r^2$ is the average gas column density, r is the cloud radius, and m is the mean particle mass per hydrogen nucleon. For a uniform density sphere, the total optical depth $\langle\tau\rangle = \langle\tau_r\rangle \equiv (4/3)\sigma_g n r$. For a complex, $\langle\tau\rangle \geqslant (4/3)\sigma_g n_1 r \equiv \langle\tau_r\rangle$, where n_1 is the gas density in the atomic shell. The parameter y is defined such that the total optical depth $\langle\tau\rangle$ is normalized relative to the critical (area-averaged) dust depth $\langle\tau_1\rangle$ required for the appearance of an H_2 core at $r = 0$. The critical depths $\langle\tau_1\rangle$ are auxiliary quantities also computed by MK10 for the uniform density spheres and complexes, assuming irradiation by isotropic radiation fields. The $\langle\tau_1\rangle$ for spheres correspond to our $\tau_1^{\rm p}$ for two-sided illumination of slabs by isotropic fields. In our terminology, these are the (total) *H I-dust* optical depths in spheres and slabs. For sharp transitions these are critical optical depths.

The MK10 fitting formula (their Equation (82)) for the H_2 mass fraction in uniform density spheres may be rewritten as[19]

$$f_{H_2}^{\rm s} \simeq 1 - \frac{1.5}{y + 0.5y^{-1.8}} \qquad (100)$$

(where the superscript "s" is for spheres). Their critical H I-dust optical depth is

$$\langle\tau_1\rangle = 1.1 \times \ln[1 + 0.6\alpha G + 0.01(\alpha G)^2]. \qquad (101)$$

Again, in Equation (100) $y \equiv \langle\tau\rangle/\langle\tau_1\rangle$. In Figures 11 and 12 we plot $f_{H_2}^{\rm s}$ versus y and $\langle\tau_1\rangle$ versus αG for comparisons with our expressions for slabs.

For complexes, the MK10 fit formula for the H_2 mass fraction (their Equation (93)) may be rewritten as[20]

$$f_{H_2}^{\rm c} \simeq 1 - \frac{1.5}{y + 0.5}. \qquad (102)$$

[19] This follows from MK10 Equation (82) for $x_{H_2}^3 \equiv f_{H_2}$, where x_{H_2} is the scaled radius of the H_2 core in a uniform density cloud. For a critical cloud $x_{H_2} = 0$, and this occurs when their $\xi_d = 1.944$, where $\xi_d \equiv 2.22\ln[1 + 0.6\chi + 0.01\chi^2]/\langle\tau_r\rangle$. This gives our expression (101) for the critical depth $\langle\tau_1\rangle$, where we have replaced χ with our αG. Our expression (100) is then MK10 Equation (82), where $y = 2/\xi_d$.

[20] For MK10 Equation (93) for the complexes their $f_{H_2}(s)$ just vanishes for the critical value $s = 2$, where $s \equiv 2.22\ln[1 + 0.6\chi + 0.01\chi^2]/\langle\tau_c\rangle$, and $\langle\tau_c\rangle$ is the total area-averaged dust optical depth of the complex (MK10, Equation (91)). This again gives our expression (101) for the critical depth $\langle\tau_1^{\rm c}\rangle$. Our expression (102) is then MK10 Equation (93), where their $s \equiv 2/y$.

(The superscript "c" is for complexes.) Fully atomic complexes and uniform density spheres are identical, so the critical H I-dust depth $\langle\tau_1\rangle$ for complexes is also given by Equation (101). Because of the compression of the molecular gas, the functional form for f_{H_2} is altered compared with uniform density spheres, and the $y^{-1.8}$ factor in the denominator of Equation (100) is replaced by unity in Equation (102). We also plot $f_{H_2}^{\rm c}$ for the complexes in Figure 11.

Figure 12 shows the similarity in the critical H I-dust optical depths for slabs and spheres. For isotropic fields, and for αG ranging from 0.01 to 10^2, the differences are no greater than 20%. Furthermore, Figure 12 shows that switching from isotropic to corresponding beamed radiation for a slab is in fact much more significant than switching from a slab to a sphere for an isotropic field. For isotropic fields, the H I-dust optical depths for slabs and complexes are equal for $\alpha G \approx 1.5$, so for two-phased H I equilibrium ($[\alpha G]_{\rm CNM}/2 \sim 1$) the differences between the H I-dust optical depths for spheres and slabs are negligible. Thus, for $\alpha G \sim 1$ any differences between spheres and slabs arise only because of any remaining differences in the functional forms for f_{H_2}.

Figure 11 shows the similarity and small differences in f_{H_2} for slabs, uniform-density spheres, and complexes, as given by Equations (97), (100), and (102). For slabs, our formula (97) for f_{H_2} is unaltered if the molecular gas is assumed to be denser than the atomic gas, and there is no distinction between uniform-density and isobaric conditions. The differences are all small. For example, for a spherical complex compared with a slab, the percentage difference in $f_{H_2}(y)$ is at most 40% at $y = 3$.

4.2.3. H_2 Mass Fractions and Star-formation Thresholds in Self-regulated Gas

If H_2 is a requirement for star formation, we may define the cloud gas column at which $f_{H_2} = 0.5$ as the "star-formation threshold." This is a plausible definition for sharp H I-to-H_2 transitions for which a "sterile" atomic layer is well defined. As given by Equations (97), (100), and (102), $f_{H_2} = 0.5$ for $y = 2$, 2.93, and 2.5, for slabs, uniform density spheres, and complexes. We define $\Sigma_{\rm gas,*}$ as the threshold gas mass surface density for which $f_{H_2} = 0.5$.

For estimates of *metallicity-dependent* H_2 mass fractions and star-formation thresholds in Kennicutt–Schmidt relations for galaxy disks, we adopt the KMT/MK10 "self-regulation" ansatz that the H I in star-forming clouds is typically driven to the CNM densities/pressures required for two-phase equilibria as set by the stellar FUV radiation fields. Thus, for any Z' we assume that $\alpha G = (\alpha G)_{\rm CNM}(Z')$ (Equation (59)). Because $(\alpha G)_{\rm CNM} \sim 1$ to 2 for all Z', the H I-to-H_2 transitions are sharp to a good approximation (as argued by KMT/MK10). For our

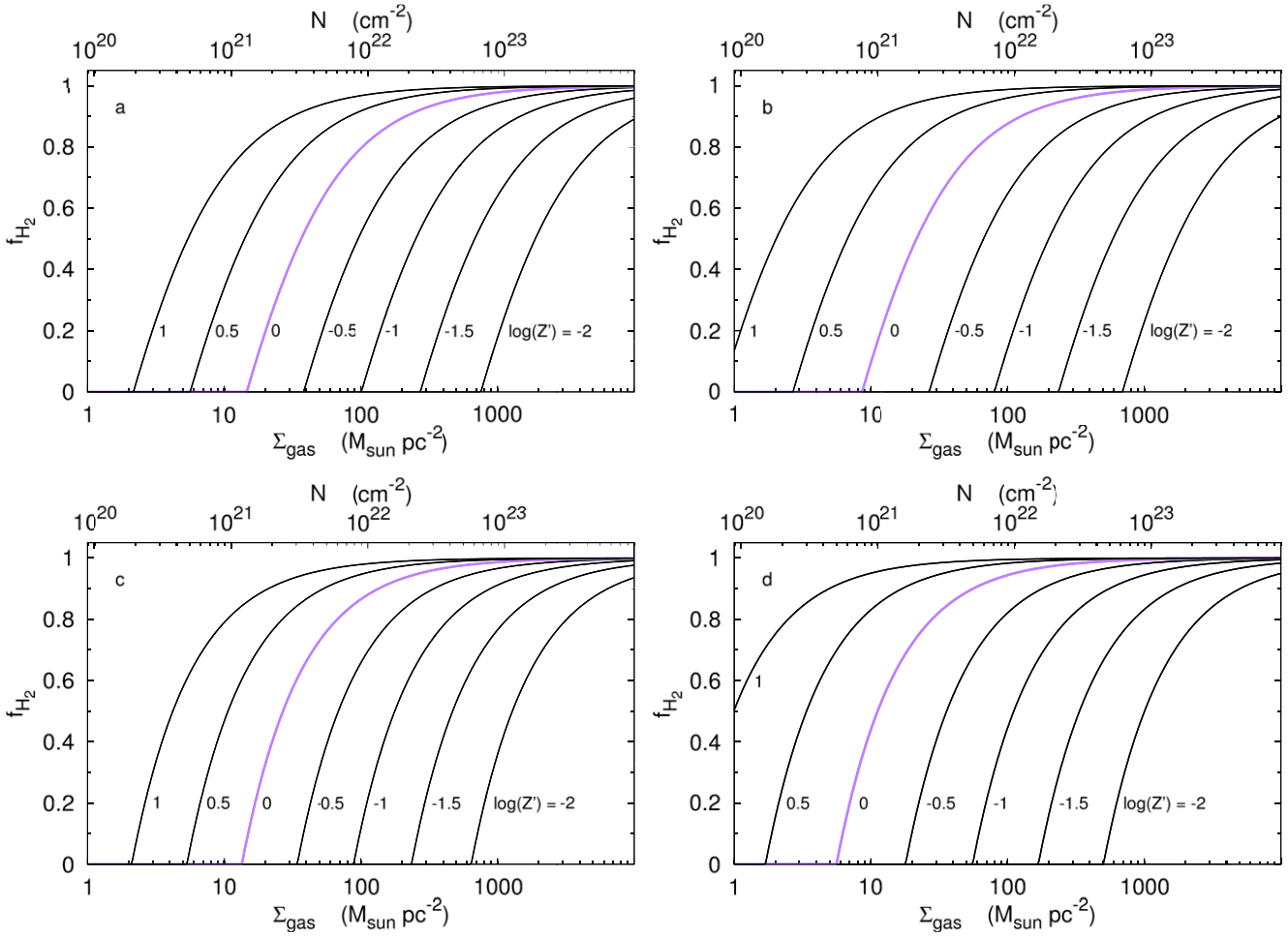

Figure 14. H_2 mass fractions as functions of total gas mass surface density for metallicities Z' from 0.01 to 10 times solar. (a) Spherical complex, with $\sigma_g = 1.0 \times 10^{-21} Z'$ cm^2 and excluding H_2-dust absorption in setting $(\alpha G)_{\rm CNM}$, as assumed by MK10. (b) Spherical complex with $\sigma_g = 1.0 \times 10^{-21} Z'$ cm^2 but including H_2-dust. (c) Plane-parallel slab, with the MK10 relation $\sigma_g = 1.0 \times 10^{-21} Z'$ cm^2 and excluding H_2-dust. (d) Slab with $\sigma_g = 1.9 \times 10^{-21} Z'$ cm^2 and including H_2-dust.

(A color version of this figure is available in the online journal.)

slabs we therefore assume H I-H_2-H I sandwich structures, for which critical optically thick slabs occur at $y = 1$ (as discussed in Section 4.2.1).

We present four sets of computations to compare results for spheres versus slabs.

First, in Figure 14, panel (a), we use Equations (102) and (101) to reproduce the MK10 results for $f^{\rm c}_{\rm H_2}(\Sigma_{\rm gas})$ for spherical atomic–molecular complexes (Figure 5 in MK10). Here $\Sigma_{\rm gas} \equiv (m/\sigma_g)\langle\tau\rangle$ is the area-averaged gas mass surface density, where m is the mean particle mass per hydrogen nucleus and $\langle\tau\rangle$ is the area-averaged dust opacity. Thus, in Equation (102) $y = \Sigma_{\rm gas}/\Sigma_1$, where $\Sigma_1 \equiv (m/\sigma_g)\langle\tau_1\rangle$, and where $\langle\tau_1\rangle$ is given by Equation (101) for each $(\alpha G)_{\rm CNM}(Z')$. We set $m = 2.34 \times 10^{-24}$ g as appropriate for a cosmic hydrogen–helium mixture. KMT/MK10 assume that the dust cross section scales with metallicity as $\sigma_g = 1.0 \times 10^{-21} Z'$ cm^2, so we set our $\phi_g = 1/1.9$ (see Equation (20)). MK10 also implicitly assume that H_2-dust absorption is negligible for all Z', so we exclude our H_2-dust term, $(2.64\phi_g Z')^{1/2}$, in the denominator of Equation (59). The resulting curves for $f_{\rm H_2}$ as functions of $\Sigma_{\rm gas}$ ($M_\odot$ pc^{-2}) are displayed in Figure 14 for Z' ranging from 0.01 to 10. They are a precise reproduction of the MK10 results (their Figure 5). For example, with the above assumptions, $Z' = 1$ gives $(\alpha G)_{\rm CNM} = 3.6$ so that $\langle\tau_1\rangle = 1.3$, and a molecular core appears ($y = 1$) for $\Sigma_{\rm gas} = 14.6\, M_\odot$ pc^{-2}. The $f^{\rm c}_{\rm H_2} = 0.5$ star-formation threshold ($y = 2.5$) is then $\Sigma_{\rm gas,*} = 36.5\, M_\odot$ pc^{-2}. For smaller (larger) Z', the curves shift to the right (left) exactly as in Figure 5 of MK10.

Second, in Figure 14, panel (b), we show results for spherical complexes, again with $\phi_g = 1/1.9$ but now *with* the H_2-dust term included in the estimate for $(\alpha G)_{\rm CNM}(Z')$. As expected, for very low Z' the $f_{\rm H_2}$ curves and the corresponding star-formation thresholds are unaltered, since this is the complete line overlap regime for which H_2-dust is negligible. However, for $Z' \gtrsim 0.3$ the curves start to shift to the left and the thresholds are reduced to smaller gas mass surface densities. These shifts are due to the reductions of the effective dissociation fluxes by the non-negligible H_2-dust opacities. For example, when H_2-dust is included for $Z' = 1$ we have $(\alpha G)_{\rm CNM} = 1.6$ (for $\phi_g = 1/1.9$) so that $\langle\tau_1\rangle = 0.77$, and the H_2 core appears at $\Sigma_{\rm gas} \simeq 8.6\, M_\odot$ pc^{-2} and $\Sigma_{\rm gas,*} = 21.5\, M_\odot$ pc^{-2}. The inclusion of H_2-dust in the estimate for $(\alpha G)_{\rm CNM}$ modifies the MK10 results for solar and super-solar metallicities.

Third, in Figure 14, panel (c), we again adopt the MK10 assumptions, $\phi_g = 1/1.9$ and negligible H_2-dust for any Z' but for slabs instead of spheres, and we use Equation (97) to compute

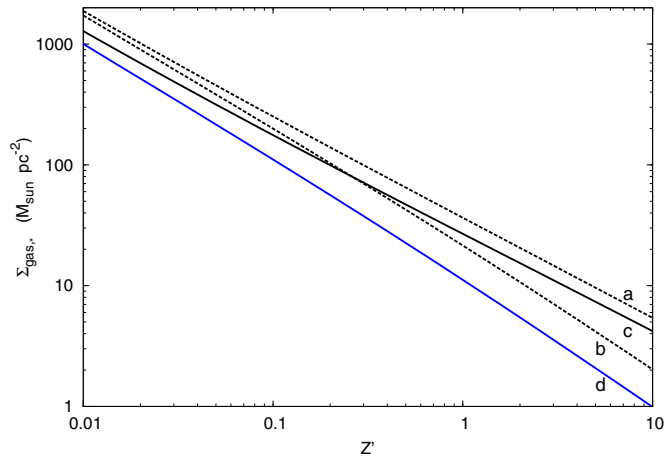

Figure 15. Star-formation threshold gas mass surface density $\Sigma_{\rm gas,*}$ at which the H_2 mass fraction $f_{H_2} = 0.5$ for the four models, (a), (b), (c), and (d), in Figure 14 (see text).

(A color version of this figure is available in the online journal.)

$f^{\rm p}_{H_2}(\Sigma_{\rm gas})$. Here $\Sigma_{\rm gas} = (m/\sigma_g)\tau_z$, where τ_z is the total dust depth of the slab, so that $y = \Sigma_{\rm gas}/\Sigma_1$ where $\Sigma_1 = (m/\sigma_g)\tau_1^{\rm p}$, and the critical H I-dust optical depth $\tau_1^{\rm p}$ is given by Equation (98) for each $(\alpha G)_{\rm CNM}(Z')$. We have already seen that the functional forms for the mass fractions are very similar for complexes and slabs (with at most a 40% difference at $y = 3$) and that the critical H I-dust columns are essentially equal for $\alpha G \sim 1$ (as for self-regulated gas). It is therefore not surprising that the curves for slabs are almost identical to the MK10 results in Figure 14. For $Z' = 1$, we again have $(\alpha G)_{\rm CNM} = 3.6$ so that $\tau_1^{\rm p} = 1.2$ and H_2 appears for $\Sigma_{\rm gas} \simeq 13.4\,M_\odot\ {\rm pc}^{-2}$ and the star-formation threshold ($y = 2$) is at $\Sigma_{\rm gas,*} = 26.8\,M_\odot\ {\rm pc}^{-2}$. For metallicities $Z' \gtrsim 0.3$, the neglect of H_2-dust in setting $(\alpha G)_{\rm CNM}$ is more significant than switching from spherical to plane-parallel cloud geometry.

In Figure 14, panel (d), we again present results for slabs but now with our preferred and somewhat larger $\sigma_g = 1.9 \times 10^{-21} Z'\ {\rm cm}^2$ ($\phi_g = 1$) and with the inclusion of H_2-dust absorption in setting $(\alpha G)_{\rm CNM}(Z')$. The $f^{\rm p}_{H_2}$ curves and thresholds are shifted to lower gas mass surface densities compared to Figure 14. For $Z' = 1$, we now have $(\alpha G)_{\rm CNM} = 2.6$, given that $\tau_1^{\rm p} = 0.95$, so that H_2 appears at $\Sigma_{\rm gas} = 5.6 M_\odot\ {\rm pc}^{-2}$ and the star-formation threshold surface gas mass density is $\Sigma_{\rm gas,*} = 11\,M_\odot\ {\rm pc}^{-2}$.

Finally, in Figure 15 we plot $\Sigma_{\rm gas,*}(Z')$ for the above four model sets. At any Z' the star-formation thresholds vary by factors of 2–3 for the four model assumptions, for Z' between 0.01 and ~2. Again, we are assuming that $\alpha G = (\alpha G)_{\rm CNM}(Z')$ for which the critical H I-dust optical depths are all of order unity. The threshold gas mass surface densities therefore scale as $\sim 2m/\sigma_g$, and we have

$$\Sigma_{\rm gas,*}(Z') \approx \frac{12}{\phi_g Z'}\ \ M_\odot\ {\rm pc}^{-2}. \qquad (103)$$

For $Z' \sim 1$, the star-formation thresholds are of order $10\,M_\odot\ {\rm pc}^{-2}$.

The predicted H I columns and star-formation thresholds appear consistent with observations, at least for ~solar metallicity systems. For example, in a recent GALFA-H I study of the H I-to-H_2 transition on sub-parsec scales in the Perseus giant molecular cloud, Lee et al. (2012) find an almost constant H I surface density of $\Sigma_{\rm H\,I} \sim 6$–$8\,M_\odot\ {\rm pc}^{-2}$ in each of the mapped sub-regions. For $Z' = 1$, this is consistent with the H I columns expected for αG of order unity, including conditions appropriate for two-phased equilibrium. Thus, Perseus is in the H I-dust-limited and strong-field regime. On larger scales, Leroy et al. (2008) find a mean total gas column of $14\,M_\odot\ {\rm pc}^{-2}$ at the H I-to-H_2 transition radii (see their Table 5) in their analysis of the H I and CO distributions in the THINGS and HERACLES galaxy surveys. The observed threshold column density of $14\,M_\odot\ {\rm pc}^{-2}$ is in harmony with our 1D predictions or the spherical KMT/MK10 models (see Figure 15). However, in this interpretation there must be typically one primary UV absorbing cloud (GMC) per line of sight in the galaxy surveys, with negligible additional diffuse H I, since our predicted thresholds are for single cold clouds.

5. RECAP AND SUMMARY

In this paper we have presented analytic theory and numerical computations for the atomic-to-molecular (H I-to-H_2) transitions, and the buildup of atomic hydrogen (H I) gas columns, in the PDRs of optically thick interstellar clouds illuminated by photodissociating FUV LW radiation fields. We have focused on simple idealized uniform density (1D) planar slabs that fully absorb the incident radiation. This enables a Strömgren type analysis (Sternberg 1988, "S88") for the total steady state column density of H I that is maintained by the incident photodissociating flux. The behavior is more complicated than for classical (dust-free) photoionized H II regions, (1) because H_2 photodissociation is a (multi-)line absorption process and (2) because of the generally inevitable competition between H_2-line absorption, H_2-dust absorption, and H I-dust absorption of the LW photons.

As discussed in Section 1, the H I-to-H_2 transition in interstellar gas has been investigated by numerous authors over many years, with varying levels of analytic and numerical sophistication. In this paper we extend the analytic theory developed in S88 and consider 1D slabs irradiated by either beamed or isotropic fields. The beamed configuration is appropriate for clouds near a localized radiation source. Isotropic irradiation may be more appropriate for ambient or "global" conditions in galaxies. In our theoretical development we make the important distinction between H I-dust and H_2-dust absorption, which is not previously discussed in the literature. The three-way competition between H I-dust absorption, H_2-dust absorption, and H_2-line absorption determines the behavior and dependence of the atomic column density on the environmental parameters.

Our analytic formulae and results are developed in Section 2 and verified in Section 3 with detailed numerical radiative transfer computations, including for the H_2-dust-limited dissociation bandwidth. In Section 4 we compare our results to models that assume spherical symmetry.

To conclude this paper, we recap our basic results as follows. The fundamental dimensionless parameter in the problem is

$$\alpha G = \frac{D_0 G}{Rn} = \frac{\sigma_g \bar{F}_\nu W_{g,{\rm tot}}}{Rn} = \bar{f}_{\rm diss}\frac{\sigma_g w F_0}{Rn}$$

$$= 1.54\,\frac{I_{\rm UV}}{(n/100\,{\rm cm}^{-3})}\,\frac{\phi_g}{1+(2.64\phi_g Z')^{1/2}}.$$

(See also expressions (49) and (50).) Here $I_{\rm UV}$ is the free-space FUV intensity (relative to the Draine field), D_0 is the free-space (optically thin) H_2 photodissociation rate (s^{-1}), n is the total hydrogen gas volume density (cm^{-3}), R is the H_2 formation rate coefficient ($cm^3\ s^{-1}$), G (dimensionless) is the mean self-shielding

Table 2
Glossary of Symbols

Symbol	Definition	Units
$\mathcal{I}_\nu$	Far-UV specific photon intensity.	photons cm^{-2} s^{-1} Hz^{-1} sr^{-1}
$\mathcal{I}_\nu^{\rm ISM}$	Free-space far-UV specific intensity (Equation (2)).	photons cm^{-2} s^{-1} Hz^{-1} sr^{-1}
$I_{\rm UV}$	Intensity scaling factor relative to the unit free-space Draine field.	...
F_ν	Flux density, $F_\nu \equiv 4\pi\mathcal{I}_\nu$.	photons cm^{-2} s^{-1} Hz^{-1}
$\bar{F}_\nu$	Mean flux density in LW band (Equation (12)).	photons cm^{-2} s^{-1} Hz^{-1}
F_0	Free-space LW band photon flux integral (Equations (3) and (4)).	photons cm^{-2} s^{-1}
$F_\nu(z)$	Beamed photon flux density at linear depth z in a slab.	photons cm^{-2} s^{-1} Hz^{-1}
$F(z)$	Beamed photon flux at linear depth z in a slab (Equation (76)).	photons cm^{-2} s^{-1}
$\sigma_{\nu,d}$	H_2 photodissociation cross section at frequency ν (Equations (7) and (77)).	cm^2
σ_d	Individual H_2-line photodissociation cross section (Equation (9)).	cm^2 Hz
$\sigma_d^{\rm tot}$	H_2 photodissociation cross section summed over all lines (Equation (13)).	cm^2 Hz
D	Depth-dependent H_2 photodissociation rate.	s^{-1}
D_0	Free-space H_2 photodissociation rate (Equation (5) and (15)).	s^{-1}
$D(0)$	H_2 photodissociation rate at the surface of a optically thick slab (Equation (6)).	s^{-1}
P_{vj}	LW photon H_2 pumping rate out of ro-vibrational level vj (Table 1).	s^{-1}
$\langle f_{\rm diss}\rangle_{vj}$	Mean dissociation probability out of level vj (Table 1).	...
$\bar{f}_{\rm diss}$	Mean dissociation fraction per absorbed LW photon (Equation (18)).	...
σ_g	Far-UV grain absorption cross section per hydrogen nucleon (Equation (20)).	cm^2
ϕ_g	Order unity grain composition factor.	...
Z'	Metallicity relative to solar abundances.	...
R	Grain surface H_2 formation rate coefficient (Equation (21)).	cm^3 s^{-1}
T	Gas temperature.	K
n_1	Atomic hydrogen (H I) volume density.	cm^{-3}
n_2	Molecular hydrogen (H_2) volume density.	cm^{-3}
n	Total hydrogen gas volume density, $\equiv n_1 + 2n_2$.	cm^{-3}
N_1	H I column density.	cm^{-2}
N_2	H_2 column density.	cm^{-2}
N	Hydrogen gas column density, $N \equiv N_1 + 2N_2$.	cm^{-2}
$\tau_g \equiv \sigma_g N$	Dust opacity in normal direction.	...
$N_{1,\rm tot}$	Total H I column density on one side of an optically thick slab.	cm^{-2}
$\tau_{1,\rm tot} \equiv \sigma_g$	H I-dust opacity in normal direction.	...
$W_d(N_2)$	H_2-line overlap limited dissociation bandwidth.	Hz
$W_g(N_2)$	H_2-dust-limited dissociation bandwidth.	Hz
$W_{d,\rm tot}$	Total H_2-dust-limited dissociation bandwidth.	Hz
w	Normalized H_2-dust-limited dissociation bandwidth (Equation (29)).	...
$f_{\rm shield}(N_2)$	H_2 self-shielding function (Equations (16) and (72)).	...
$\langle\mu\rangle$	Mean ray-angle factor for H I-dust opacity (Equations (63) and (75)).	...
$\alpha \equiv D_0/(Rn)$	Free-space atomic-to-molecular density ratio (Equations (34) and (44)).	...
$G(\sigma_g)$	Mean self-shielding factor (Equations (41), (45)–(48)).	...
αG	Fundamental dimensionless parameter for the HI-to-H_2 transition (Equations (49)– (51)).	...
$n_{\rm CNM}$	CNM gas density for multiphased H I equilibrium (Equation (58)).	cm^{-3}
$(\alpha G)_{\rm CNM}$	αG for two-phase H I equilibrium (Equation (59)).	...
$\Sigma_{\rm H_2}$	H_2 mass surface density in plane-parallel slab.	$M_\odot$ pc^{-2}
$\Sigma_{\rm gas}$	Total gas mass surface density in plane-parallel slab.	$M_\odot$ pc^{-2}
$M_{\rm H_2}$	H_2 gas mass within sphere.	$M_\odot$
$M_{\rm gas}$	Total gas mass within sphere.	$M_\odot$
$\tau_z \equiv n\sigma_g z$	Total dust optical depth through slab of finite linear width z.	...
$\tau_r \equiv n\sigma_g r$	Dust optical depth along radius r of a sphere.	...
y	Total dust optical depth normalized to the H I-dust optical depth (Equation (97)).	...

Table 2
(Continued)

Symbol	Definition	Units
$\tau_1^{\rm p}$	H I-dust optical depth, finite slab, two-sided irradiation, isotropic (Equation (98)).	...
$\tau_1^{\rm p,b}$	H I-dust optical depth, finite slab, two-sided radiation, beamed (Equation (99)).	...
$\langle\tau_1\rangle$	Mean H I-dust optical depth, sphere, isotropic irradiation (Equation (101)).	...
$f_{\rm H_2}^{\rm p}$	H_2 mass fraction for slab (Equation (97)).	...
$f_{\rm H_2}^{\rm s}$	H_2 mass fraction for uniform density sphere (Equation (100)).	...
$f_{\rm H_2}^{\rm c}$	H_2 mass fraction for spherical atomic-molecular complex (Equation (102)).	...
$\Sigma_{\rm gas,*}$	Star-formation threshold gas surface density at which $f_{\rm H_2}=0.5$.	$M_\odot$ pc^{-2}

factor, σ_g is the FUV continuum dust absorption cross section (cm^2), $\bar{F}_\nu$ is the mean photon flux density (cm^{-2} s^{-1} Hz^{-1}) in the (912–1108 Å) LW band, F_0 is the total LW photon flux (cm^{-2} s^{-1}), $\bar{f}_{\rm diss}$ is the mean dissociation probability, Z' is the metallicity relative to solar, $W_{g,\rm tot}$ is the total H_2-dust-limited dissociation bandwidth (Hz), w (dimensionless) is the normalized bandwidth, and ϕ_g is a factor of order unity depending on the dust grain absorption properties. The final dependence of αG on Z' is via the metallicity-dependent dissociation bandwidth w (see Equation (29)).

For two-sided illumination of an optically thick slab by beamed radiation, our analytic expression for the total atomic (H I) column density is (see Equation (40))

$$N_{\rm H\,I} = 2\times\frac{1}{\sigma_g}\ln\left[\frac{\alpha G}{2}+1\right] = \frac{1.05\times10^{21}}{Z'\phi_g}\ln\left[\frac{\alpha G}{2}+1\right]\ {\rm cm}^{-2},$$

or as a gas mass surface density (including a factor of 1.4 for helium)

$$\Sigma_{\rm gas,H\,I} = \frac{11.9}{Z'\phi_g}\ln\left[\frac{\alpha G}{2}+1\right]\ M_\odot\ {\rm pc}^{-2}.$$

For two-sided irradiation by an isotropic field (see Equation (66)),

$$N_{\rm H\,I} = 2\times\frac{\langle\mu\rangle}{\sigma_g}\ln\left[\frac{1}{\langle\mu\rangle}\frac{\alpha G}{4}+1\right] = \frac{8.42\times10^{20}}{Z'\phi_g}\ln\left[\frac{\alpha G}{3.2}+1\right]\ {\rm cm}^{-2},$$

(where $\langle\mu\rangle=0.8$), or

$$\Sigma_{\rm gas,H\,I} = \frac{9.5}{Z'\phi_g}\ln\left[\frac{\alpha G}{3.2}+1\right]\ M_\odot\ {\rm pc}^{-2}.$$

These expressions are generally valid for all regimes, from the weak- to strong-field limits (small and large αG), for all H I-to-H_2 transition profile shapes (gradual or sharp), and for arbitrary metallicity Z' (small or large).

For an optically thick cloud with total gas mass surface density $\Sigma_{\rm gas}$, the integral molecular (H_2) gas fraction is

$$f_{\rm H_2}(\Sigma_{\rm gas}) = 1-\frac{\Sigma_{\rm H\,I}}{\Sigma_{\rm gas}}$$

with $\Sigma_{\rm H\,I}$ as given above for either beamed or isotropic fields. In Figure 14 (panel (a) versus (c)) we compare our results for 1D slabs with the H_2 mass fractions for spheres. The differences are very small.

Our formulae for the H I columns and H_2 mass fractions may be incorporated easily into hydrodynamics simulations for galaxy evolution.

For $\alpha G/2\lesssim 1$ the H I-to-H_2 transitions are gradual, and the atomic columns are built up in the predominantly molecular portions of the cloud. For $\alpha G/2\gtrsim 1$ the transitions are sharp, and the H I is built up in outer fully atomic layers. For sharp transitions, the H I-H_2-H I sandwich structure for slabs corresponds to H I shell and H_2 core structures for spheres. If star-formation requires the conversion to H_2, then a threshold surface density, $\Sigma_{\rm gas,*}$, may be defined at which the molecular fraction $f_{\rm H_2}=0.5$. For $\alpha G/2\gtrsim 1$ and sharp transitions we then have $\Sigma_{\rm gas,*}\equiv 2\Sigma_{\rm H\,I}$.

For self-regulated galaxy disks (ala KMT/MK10) in which the H I is driven to two-phased thermal equilibrium (and heated by FUV photoelectric emission from dust grains), the dimensionless parameter αG is restricted to a narrow range close to $(\alpha G)_{\rm CNM}$, where

$$\frac{(\alpha G)_{\rm CNM}}{2}\ \approx\ 1,$$

independent of the metallicity Z'. For such self-regulated systems, our theory then predicts a metallicity-dependent H I-to-H_2 star-formation threshold for individual clouds

$$\Sigma_{\rm gas,*}(Z')\ \approx\ \frac{12}{\phi_g Z'}\ M_\odot\ {\rm pc}^{-2}.$$

This appears consistent with Galactic and extragalactic observations, at least for solar metallicity systems.

We thank Chris McKee for many discussions and for detailed comments on our manuscript, including assistance with Equation (100). We thank Alex Dalgarno, Reinhard Genzel, Avi Loeb, David Neufeld, Tsevi Mazeh, Ewine van Dishoeck, and the referee for helpful comments and conversations about this work. A.S. is supported by the DFG via German-Israeli Project Cooperation grant STE1869/1-1/GE625/15-1 and by a PBC Israel Science Foundation I-CORE Program grant 1829/12. This work was supported in part by grant SYMPAYTICO (ANR-11-BS56-0023) from the French Agence Nationale de la Recherche and by the French CNRS national program PCMI. The early stages of our project was funded by the France-Israel High Council for Science and Technology.

APPENDIX

GLOSSARY OF SYMBOLS

Table 2 is a glossary of symbols we have used in this paper. In this listing we also refer to the equations in which the various symbols appear and/or are defined.

REFERENCES

Aaronson, M., Black, J. H., & McKee, C. F. 1974, ApJL, 191, L53
Abel, T., Anninos, P., Zhang, Y., & Norman, M. L. 1997, NewA, 2, 181
Abgrall, H., Le Bourlot, J., Pineau Des Forets, G., et al. 1992, A&A, 253, 525
Abgrall, H., Roueff, E., & Drira, I. 2000, A&AS, 141, 297
Abgrall, H., Roueff, E., Launay, F., Roncin, J. Y., & Subtil, J. L. 1993a, A&AS, 101, 323
Abgrall, H., Roueff, E., Launay, F., Roncin, J. Y., & Subtil, J. L. 1993b, A&AS, 101, 273
Ahn, K., Shapiro, P. R., Iliev, I. T., Mellema, G., & Pen, U.-L. 2009, ApJ, 695, 1430
Albornoz Vásquez, D., Rahmani, H., Noterdaeme, P., et al. 2014, A&A, 562, A88
Allen, R. J., Atherton, P. D., & Tilanus, R. P. J. 1986, Natur, 319, 296
Allen, R. J., Knapen, J. H., Bohlin, R., & Stecher, T. P. 1997, ApJ, 487, 171
Andersson, B.-G., Roger, R. S., & Wannier, P. G. 1992, A&A, 260, 355
Andersson, B.-G., & Wannier, P. G. 1993, ApJ, 402, 585
Barlow, M. J., & Silk, J. 1976, ApJ, 207, 131
Bigiel, F., Leroy, A., Walter, F., et al. 2008, AJ, 136, 2846
Bisbas, T. G., Bell, T. A., Viti, S., Yates, J., & Barlow, M. J. 2012, MNRAS, 427, 2100
Black, J. H., & Dalgarno, A. 1976, ApJ, 203, 132
Black, J. H., & Dalgarno, A. 1977, ApJS, 34, 405
Black, J. H., & van Dishoeck, E. F. 1987, ApJ, 322, 412
Blitz, L., & Rosolowsky, E. 2004, ApJL, 612, L29
Blitz, L., & Rosolowsky, E. 2006, ApJ, 650, 933
Bohlin, R. C., Savage, B. D., & Drake, J. F. 1978, ApJ, 224, 132
Bok, B. J., Lawrence, R. S., & Menon, T. K. 1955, PASP, 67, 108
Böker, T., Lisenfeld, U., & Schinnerer, E. 2003, A&A, 406, 87
Bolatto, A. D., Leroy, A. K., Jameson, K., et al. 2011, ApJ, 741, 12
Bromm, V., Yoshida, N., Hernquist, L., & McKee, C. F. 2009, Natur, 459, 49
Browning, M. K., Tumlinson, J., & Shull, J. M. 2003, ApJ, 582, 810
Burton, M. G., Hollenbach, D. J., & Tielens, A. G. G. M. 1990, ApJ, 365, 620
Burton, W. B., Liszt, H. S., & Baker, P. L. 1978, ApJL, 219, L67
Cardelli, J. A., Clayton, G. C., & Mathis, J. S. 1989, ApJ, 345, 245
Carruthers, G. R. 1970, ApJL, 161, L81
Cazaux, S., & Tielens, A. G. G. M. 2002, ApJL, 575, L29
Christensen, C., Quinn, T., Governato, F., et al. 2012, MNRAS, 425, 3058
Ciardi, B., Ferrara, A., & Abel, T. 2000, ApJ, 533, 594
Crighton, N. H. M., Bechtold, J., Carswell, R. F., et al. 2013, MNRAS, 433, 178
Cui, J., Bechtold, J., Ge, J., & Meyer, D. M. 2005, ApJ, 633, 649
Dalgarno, A. 2006, PNAS, 103, 12269
Davé, R., Katz, N., Oppenheimer, B. D., Kollmeier, J. A., & Weinberg, D. H. 2013, MNRAS, 434, 2645
de Jong, T. 1972, A&A, 20, 263
de Jong, T., Boland, W., & Dalgarno, A. 1980, A&A, 91, 68
Diaz-Miller, R. I., Franco, J., & Shore, S. N. 1998, ApJ, 501, 192
Dijkstra, M., Haiman, Z., Mesinger, A., & Wyithe, J. S. B. 2008, MNRAS, 391, 1961
Draine, B. T. 1978, ApJS, 36, 595
Draine, B. T. 2003, ARA&A, 41, 241
Draine, B. T. 2011, Physics of the Interstellar and Intergalactic Medium (Princeton, NJ: Princeton Univ. Press)
Draine, B. T., & Bertoldi, F. 1996, ApJ, 468, 269
Elmegreen, B. G. 1993, ApJ, 411, 170
Elmegreen, B. G., & Elmegreen, D. M. 1987, ApJ, 320, 182
Faucher-Giguère, C.-A., Quataert, E., & Hopkins, P. F. 2013, MNRAS, 433, 1970
Feldmann, R., Hernandez, J., & Gnedin, N. Y. 2012, ApJ, 761, 167
Federman, S. R., Glassgold, A. E., & Kwan, J. 1979, ApJ, 227, 466
Fialkov, A., Barkana, R., Tseliakhovich, D., & Hirata, C. M. 2012, MNRAS, 424, 1335
Field, G. B., Goldsmith, D. W., & Habing, H. J. 1969, ApJ, 155, 149
Field, G. B., Somerville, W. B., & Dressler, K. 1966, ARA&A, 4, 207
Fitzpatrick, E. L. 1999, PASP, 111, 63
Flannery, B. P., Roberge, W., & Rybicki, G. B. 1980, ApJ, 236, 598
Foltz, C. B., Chaffee, F. H., Jr., & Black, J. H. 1988, ApJ, 324, 267
France, K., Nell, N., Kane, R., et al. 2013, ApJL, 772, L9
Fu, J., Guo, Q., Kauffmann, G., & Krumholz, M. R. 2010, MNRAS, 409, 515
Fukui, Y., Okamoto, R., Yamamoto, H., et al. 2014, arXiv:1401.7398
Fumagalli, M., Krumholz, M. R., & Hunt, L. K. 2010, ApJ, 722, 919
Ge, J., & Bechtold, J. 1997, ApJL, 477, L73
Genzel, R., Tacconi, L. J., Combes, F., et al. 2012, ApJ, 746, 69
Genzel, R., Tacconi, L. J., Kurk, J., et al. 2013, ApJ, 773, 68
Gillmon, K., & Shull, J. M. 2006, ApJ, 636, 908
Gillmon, K., Shull, J. M., Tumlinson, J., & Danforth, C. 2006, ApJ, 636, 891
Gir, B.-Y., Blitz, L., & Magnani, L. 1994, ApJ, 434, 162
Glassgold, A. E., & Langer, W. D. 1974, ApJ, 193, 73
Glover, S. C. O., & Brand, P. W. J. L. 2003, MNRAS, 340, 210
Glover, S. C. O., Federrath, C., Mac Low, M.-M., & Klessen, R. S. 2010, MNRAS, 404, 2
Gnedin, N. Y., Tassis, K., & Kravtsov, A. V. 2009, ApJ, 697, 55
Goicoechea, J. R., & Le Bourlot, J. 2007, A&A, 467, 1
Goldshmidt, O., & Sternberg, A. 1995, ApJ, 439, 256
Goldsmith, P. F., & Li, D. 2005, ApJ, 622, 938
Goldsmith, P. F., Li, D., & Krčo, M. 2007, ApJ, 654, 273
Gomez, Y., Lebron, M., Rodriguez, L. F., et al. 1998, ApJ, 503, 297
Gould, R. J., & Harwit, M. 1963, ApJ, 137, 694
Gould, R. J., & Salpeter, E. E. 1963, ApJ, 138, 393
Habart, E., Boulanger, F., Verstraete, L., Walmsley, C. M., & Pineau des Forêts, G. 2004, A&A, 414, 531
Habart, E., Boulanger, F., Verstraete, L., et al. 2003, A&A, 397, 623
Habing, H. J. 1968, BAN, 19, 421
Haiman, Z., Rees, M. J., & Loeb, A. 1996, ApJ, 467, 522
Haiman, Z., Rees, M. J., & Loeb, A. 1997, ApJ, 476, 458
Heiles, C. 1969, ApJ, 156, 493
Heiner, J. S., Allen, R. J., & van der Kruit, P. C. 2009, ApJ, 700, 545
Heiner, J. S., Allen, R. J., & van der Kruit, P. C. 2011, MNRAS, 416, 2
Heyer, M. H., Corbelli, E., Schneider, S. E., & Young, J. S. 2004, ApJ, 602, 723
Hill, J. K., & Hollenbach, D. J. 1978, ApJ, 225, 390
Hirashita, H., & Ferrara, A. 2005, MNRAS, 356, 1529
Hollenbach, D., & Natta, A. 1995, ApJ, 455, 133
Hollenbach, D. J., Werner, M. W., & Salpeter, E. E. 1971, ApJ, 163, 165
Holzbauer, L. N., & Furlanetto, S. R. 2012, MNRAS, 419, 718
Jura, M. 1974, ApJ, 191, 375
Kaufman, M. J., Wolfire, M. G., Hollenbach, D. J., & Luhman, M. L. 1999, ApJ, 527, 795
Kim, J.-h., Krumholz, M. R., Wise, J. H., et al. 2013, ApJ, 775, 109
Knapen, J. H., Allen, R. J., Heaton, H. I., Kuno, N., & Nakai, N. 2006, A&A, 455, 897
Knapp, G. R. 1974, AJ, 79, 527
Krčo, M., & Goldsmith, P. F. 2010, ApJ, 724, 1402
Krumholz, M. R., McKee, C. F., & Tumlinson, J. 2008, ApJ, 689, 865
Krumholz, M. R., McKee, C. F., & Tumlinson, J. 2009, ApJ, 693, 216
Kuhlen, M., Madau, P., & Krumholz, M. R. 2013, ApJ, 776, 34
Lagos, C. D. P., Baugh, C. M., Lacey, C. G., et al. 2011, MNRAS, 418, 1649
Le Bourlot, J., Pineau des Forêts, G., & Flower, D. R. 1999, MNRAS, 305, 802
Ledoux, C., Petitjean, P., & Srianand, R. 2006, ApJL, 640, L25
Lee, D.-H., Pak, S., Dixon, W. V. D., & van Dishoeck, E. F. 2007, ApJ, 655, 940
Lee, H.-H., Herbst, E., Pineau des Forets, G., Roueff, E., & Le Bourlot, J. 1996, A&A, 311, 690
Lee, M.-Y., Stanimirović, S., Douglas, K. A., et al. 2012, ApJ, 748, 75
Lee, M.-Y., Stanimirović, S., Wolfire, M. G., et al. 2014, ApJ, 784, 80
Leitch-Devlin, M. A., & Williams, D. A. 1985, MNRAS, 213, 295
Le Petit, F., Nehmé, C., Le Bourlot, J., & Roueff, E. 2006, ApJS, 164, 506
Lepp, S., & Shull, J. M. 1984, ApJ, 280, 465
Leroy, A. K., Walter, F., Brinks, E., et al. 2008, AJ, 136, 2782
Levshakov, S. A., & Varshalovich, D. A. 1985, MNRAS, 212, 517
Li, D., & Goldsmith, P. F. 2003, ApJ, 585, 823
Liszt, H., & Lucas, R. 2002, A&A, 391, 693
Liszt, H. S. 2007, A&A, 461, 205
Liszt, H. S., & Burton, W. B. 1979, ApJ, 228, 105
London, R. 1978, ApJ, 225, 405
Mac Low, M.-M., & Glover, S. C. O. 2012, ApJ, 746, 135
Madden, S. C., Geis, N., Genzel, R., et al. 1993, ApJ, 407, 579
Matthews, H. E., Purton, C. R., Roger, R. S., Dewdney, P. E., & Mitchell, G. F. 2003, ApJ, 592, 176
McCutcheon, W. H., Shuter, W. L. H., & Booth, R. S. 1978, MNRAS, 185, 755
McKee, C. F., & Krumholz, M. R. 2010, ApJ, 709, 308
Mebold, U., Winnberg, A., Kalberla, P. M. W., & Goss, W. M. 1982, A&A, 115, 223
Mészáros, P. 1968, Ap&SS, 2, 510
Miyake, S., Stancil, P. C., Sadeghpour, H. R., et al. 2010, ApJL, 709, L168
Myers, P. C., Ho, P. T. P., Schneps, M. H., et al. 1978, ApJ, 220, 864
Neufeld, D. A., & Spaans, M. 1996, ApJ, 473, 894
Noterdaeme, P., Petitjean, P., Ledoux, C., et al. 2010, A&A, 523, A80
Offner, S. S. R., Bisbas, T. G., Viti, S., & Bell, T. A. 2013, ApJ, 770, 49

Ostriker, E. C., McKee, C. F., & Leroy, A. K. 2010, ApJ, 721, 975
Palla, F., Salpeter, E. E., & Stahler, S. W. 1983, ApJ, 271, 632
Pirronello, V., Liu, C., Shen, L., & Vidali, G. 1997, ApJL, 475, L69
Popping, G., Somerville, R. S., & Trager, S. C. 2014, MNRAS, in press (arXiv:1308.6764)
Rachford, B. L., Snow, T. P., Destree, J. D., et al. 2009, ApJS, 180, 125
Rachford, B. L., Snow, T. P., Tumlinson, J., et al. 2002, ApJ, 577, 221
Rand, R. J., Kulkarni, S. R., & Rice, W. 1992, ApJ, 390, 66
Rank, D. M., Townes, C. H., & Welch, W. J. 1971, Sci, 174, 1083
Reach, W. T., Koo, B.-C., & Heiles, C. 1994, ApJ, 429, 672
Read, P. L. 1981, MNRAS, 194, 863
Richter, P., Sembach, K. R., Wakker, B. P., & Savage, B. D. 2001, ApJL, 562, L181
Robertson, B. E., & Kravtsov, A. V. 2008, ApJ, 680, 1083
Roger, R. S., & Dewdney, P. E. 1992, ApJ, 385, 536
Roger, R. S., McCutcheon, W. H., Purton, C. R., & Dewdney, P. E. 2004, A&A, 425, 553
Roger, R. S., & Pedlar, A. 1981, A&A, 94, 238
Röhser, T., Kerp, J., Winkel, B., Boulanger, F., & Lagache, G. 2014, A&A, 564, 71
Safranek-Shrader, C., Agarwal, M., Federrath, C., et al. 2012, MNRAS, 426, 1159
Sancisi, R., Goss, W. M., Anderson, C., Johansson, L. E. B., & Winnberg, A. 1974, A&A, 35, 445
Savage, B. D., Bohlin, R. C., Drake, J. F., & Budich, W. 1977, ApJ, 216, 291
Schruba, A., Leroy, A. K., Walter, F., et al. 2011, AJ, 142, 37
Schuster, K. F., Kramer, C., Hitschfeld, M., Garcia-Burillo, S., & Mookerjea, B. 2007, A&A, 461, 143
Shaw, G., Ferland, G. J., Abel, N. P., Stancil, P. C., & van Hoof, P. A. M. 2005, ApJ, 624, 794
Shaya, E. J., & Federman, S. R. 1987, ApJ, 319, 76
Shull, J. M. 1978, ApJ, 219, 877
Smith, D. A., Allen, R. J., Bohlin, R. C., Nicholson, N., & Stecher, T. P. 2000, ApJ, 538, 608
Solomon, P. M., & Werner, M. W. 1971, ApJ, 165, 41
Spaans, M., & Neufeld, D. A. 1997, ApJ, 484, 785
Spaans, M., Tielens, A. G. G. M., van Dishoeck, E. F., & Bakes, E. L. O. 1994, ApJ, 437, 270
Spaans, M., & van Dishoeck, E. F. 1997, A&A, 323, 953
Spitzer, L., Drake, J. F., Jenkins, E. B., et al. 1973, ApJL, 181, L116
Spitzer, L., Jr. 1948, ApJ, 107, 6
Spitzer, L., Jr., & Tomasko, M. G. 1968, ApJ, 152, 971
Stecher, T. P., & Williams, D. A. 1967, ApJL, 149, L29
Stephens, T. L., & Dalgarno, A. 1972, JQSRT, 12, 569
Sternberg, A. 1988, ApJ, 332, 400
Sternberg, A., & Dalgarno, A. 1989, ApJ, 338, 197
Sternberg, A., & Neufeld, D. A. 1999, ApJ, 516, 371
Stoerzer, H., Stutzki, J., & Sternberg, A. 1996, A&A, 310, 592
Strömgren, B. 1939, ApJ, 89, 526
Tacconi, L. J., Genzel, R., Neri, R., et al. 2010, Natur, 463, 781
Tacconi, L. J., Neri, R., Genzel, R., et al. 2013, ApJ, 768, 74
Takahashi, J., Masuda, K., & Nagaoka, M. 1999, MNRAS, 306, 22
Thompson, R., Nagamine, K., Jaacks, J., & Choi, J.-H. 2014, ApJ, 780, 145
Tielens, A. G. G. M., & Hollenbach, D. 1985, ApJ, 291, 722
van der Werf, P. P., & Goss, W. M. 1989, A&A, 224, 209
van der Werf, P. P., Goss, W. M., & O'Dell, C. R. 2013, ApJ, 762, 101
van der Werf, P. P., Goss, W. M., & Vanden Bout, P. A. 1988, A&A, 201, 311
van Dishoeck, E. F., & Black, J. H. 1986, ApJS, 62, 109
van Dishoeck, E. F., & Black, J. H. 1988, ApJ, 334, 771
van Dishoeck, E. F., & Black, J. H. 1990, ApJ, 360, 313
van Dishoeck, E. F., Jonkheid, B., & van Hemert, M. C. 2006, FaDi, 133, 231
Viala, Y. P. 1986, A&AS, 64, 391
Viala, Y. P., Roueff, E., & Abgrall, H. 1988, A&A, 190, 215
Visbal, E., Haiman, Z., Terrazas, B., Bryan, G. L., & Barkana, R. 2014, arXiv:1402.0882
Wakker, B. P. 2006, ApJS, 163, 282
Wannier, P. G., Lichten, S. M., Andersson, B.-G., & Morris, M. 1991, ApJS, 75, 987
Wannier, P. G., Lichten, S. M., & Morris, M. 1983, ApJ, 268, 727
Webber, W. R. 1998, ApJ, 506, 329
Welty, D. E., Xue, R., & Wong, T. 2012, ApJ, 745, 173
Williams, J. P., & Maddalena, R. J. 1996, ApJ, 464, 247
Wilson, R. W., Jefferts, K. B., & Penzias, A. A. 1970, ApJL, 161, L43
Wise, J. H., & Abel, T. 2007, ApJ, 671, 1559
Wolcott-Green, J., Haiman, Z., & Bryan, G. L. 2011, MNRAS, 418, 838
Wolfire, M. G., Hollenbach, D., & McKee, C. F. 2010, ApJ, 716, 1191
Wolfire, M. G., McKee, C. F., Hollenbach, D., & Tielens, A. G. G. M. 2003, ApJ, 587, 278
Wolfire, M. G., Tielens, A. G. G. M., Hollenbach, D., & Kaufman, M. J. 2008, ApJ, 680, 384
Wolniewicz, L., Simbotin, I., & Dalgarno, A. 1998, ApJS, 115, 293
Wong, T., & Blitz, L. 2002, ApJ, 569, 157
Wrathmall, S. A., Gusdorf, A., & Flower, D. R. 2007, MNRAS, 382, 133
Yoshida, N., Abel, T., Hernquist, L., & Sugiyama, N. 2003, ApJ, 592, 645